Jagiellonian University
Faculty of Physics, Astronomy and Applied Computer Science

Phase transition signatures in nuclear multifragmentation: Fluctuations of the largest fragment size

Tomasz Pietrzak

PhD thesis written under the supervision of
prof. dr hab. Janusz Brzychczyk

Cracow, 2023

Wydział Fizyki, Astronomii i Informatyki Stosowanej
Uniwersytet Jagielloński

Oświadczenie

Ja niżej podpisany *Tomasz Pietrzak* doktorant Wydziału Fizyki, Astronomii i Informatyki Stosowanej Uniwersytetu Jagiellońskiego oświadczam, że przedłożona przeze mnie rozprawa doktorska pt. „Phase transition signatures in nuclear multifragmentation: Fluctuations of the largest fragment size“ jest oryginalna i przedstawia wyniki badań wykonanych przeze mnie osobiście, pod kierunkiem prof. dr hab. Janusza Brzychczyka. Pracę napisałem samodzielnie.

Oświadczam, że moja rozprawa doktorska została opracowana zgodnie z Ustawą o prawie autorskim i prawach pokrewnych z dnia 4 lutego 1994 r. (Dziennik Ustaw 1994 nr 24 poz. 83 wraz z późniejszymi zmianami).

Jestem świadom, że niezgodność niniejszego oświadczenia z prawdą ujawniona w dowolnym czasie, niezależnie od skutków prawnych wynikających z ww. ustawy, może spowodować unieważnienie stopnia nabytego na podstawie tej rozprawy.

Kraków, dnia ....
podpis doktoranta

Abstract

Nuclear multifragmentation and its relation to the liquid-gas phase transition in nuclear matter has been the subject of intensive theoretical and experimental research. A special attention was paid to the largest fragment size fluctuations to obtain a better insight into the phase behavior of fragmenting systems. In particular, percolation studies have shown that the cumulant ratios (skewness and kurtosis) of the largest fragment size distribution provide a new robust signature of phase transition (critical behavior) in finite systems.

This thesis examines properties of the largest fragment size (charge) distributions within the Canonical Thermodynamic Model and the Statistical Multifragmentation Model (SMM). It is shown that the cumulant features characteristic of percolation transition indicate also the breakup transition observed along with a specific heat maximum, interpreted as a manifestation of liquid-gas phase transition.

The cumulant analysis of the largest fragment charge distribution is applied to the ALADIN data on fragmentation of Au projectiles at relativistic energies. Extensive comparisons with predictions of a bond percolation model show a remarkably accuracy of this model in reproducing the distributions as well as the whole fragmentation pattern as represented by the measured charge correlations. In analogy to percolation, the pseudocritical and critical points are identified in the fragmentation data.

The analysis method is further applied to the ALADIN S254 experimental data to investigate the isotopic dependence of projectile fragmentation. The experiment was conducted with neutron-rich ^{124}Sn and radioactive neutron-poor ^{107}Sn and ^{124}La beams of 600 MeV/nucleon incident energy and natural Sn targets. The identified transition points, well reproduced by the SMM model, are found to be weakly dependent on the A/Z ratio of the fragmenting spectator source.

For all investigated reaction systems, the transition temperature determined from the measured isotopic ratios is around 5.5 MeV, nearly independent of the size and A/Z ratio of the system. This is in agreement with predictions of the statistical models, confirming that the fragmentation process is governed by the opening of the corresponding partition space.

The thesis corroborates that the skewness and kurtosis of the largest fragment size (charge) distribution are valuable observables in searching for a phase transition in multifragmentation. Their properties appear generic for fragmentation processes. The bond percolation model precisely reproducing the experimental data may serve as a very useful reference model for studying the distinction between first- and second-order phase transitions.

Streszczenie

Multifragmentacja jąder atomowych i jej związek z przejściem fazowym ciecz-gaz w materii jądrowej jest przedmiotem intensywnych badań teoretycznych i eksperymentalnych. Szczególne znaczenie mają badania fluktuacji rozmiaru największego fragmentu, pozwalające głębiej poznać własności fazowe badanych systemów. Jak sugeruje model perkolacji, stosunki kumulant (skośność i kurtoza) rozkładu rozmiaru największego fragmentu mogą stanowić nową wartościową sygnaturę przejścia fazowego (zjawiska krytycznego) w procesach fragmentacji.

W niniejszej pracy badane są własności tych kumulant w ramach Kanonicznego Modelu Termodynamicznego oraz Statystycznego Modelu Multifragmentacji (SMM). Stwierdzono, że sygnatura charakterystyczna dla przejścia fazowego perkolacji stosuje się także do przejścia fazowego typu ciecz-gaz sygnalizowanego przez maksimum ciepła właściwego.

Analiza kumulant rozkładu ładunku największego fragmentu jest zastosowana do danych ALADIN z pomiarów fragmentacji spektatorów pocisków Au przy energiach relatywistycznych. Szczegółowe porównania z przewidywaniami modelu perkolacji wiązań wykazują wyjątkowo dobrą dokładność tego modelu w odtwarzaniu wszelkich rozkładów ładunku fragmentów oraz ich korelacji. W analogii do perkolacji zidentyfikowany zostały punkt pseudokrytyczny oraz punkt zdarzeń krytycznych.

Analizę rozszerzono na dane z eksperymentu ALADIN S254, aby zbadać zależność procesu fragmentacji od izospinu systemu. Eksperyment został przeprowadzony z wiązkami neutronowo-nadmiarowych jąder ^{124}Sn i wiązkami radioaktywnymi neutronowo-deficytowych izotopów ^{107}Sn i ^{124}La o energii 600 MeV/nukleon. Zaobserwowane sygnatury przejścia fazowego, dobrze odtworzone przez model SMM, pokazują nikły wpływ izospinu źródła na przebieg procesu fragmentacji.

Dla wszystkich badanych reakcji, temperatury w punktach przejścia fazowego, wyznaczone ze zmierzonych stosunków izotopowych, wynoszą około 5.5 MeV, prawie niezależnie od wielkości i stosunku A/Z systemu. Wynik ten jest zgodny z przewidywaniami modeli statystycznych, co wskazuje, że o rozkładzie partycji układu decydują gęstości dostępnych stanów w końcowej fazie termalizacji.

Wyniki pracy potwierdzają, że skośność i kurtoza rozkładu rozmiaru (ładunku) największego fragmentu są wartościowymi obserwablami w poszukiwaniu przejścia fazowego w multifragmentacji. Ich właściwości mają charakter ogólny dla procesów fragmentacji. Model perkolacji, który precyzyjnie opisuje dane eksperymentalne, może być wykorzystywany jako model referencyjny w badaniach sygnatur stosowanych do identyfikacji przejść fazowych.

Contents

Chapter 1

Introduction

Nuclear multifragmentation – the disintegration of highly excited nuclei into clusters of various sizes – has been intensively investigated over the past decades. This was mainly motivated by the possibility of testing the phase diagram of nuclear matter, since the multifragmentation process was predicted to be associated with a first-order liquid-gas phase transition [1–3]. On the other hand, multifragmentation observed in high energy collisions exhibit properties characteristic of the percolation critical behavior [4–11]. Although the occurrence of a phase transition is often deduced, its order and universality class are not unequivocally identified. In nuclear systems the distinction between first-order and second-order (critical behavior) phase transitions is very difficult because of finite-size and Coulomb effects, which significantly change phase transition characteristics defined in the thermodynamic limit. In particular, simulations with lattice gas models have shown that in finite systems the signals characteristic of a second-order percolation transition can be observed inside the liquid-gas coexistence zone, i.e. the first-order liquid-gas phase transition becomes similar to a critical behavior [12–16]. Moreover, in analysis of the experimental data, events cannot be sorted according to the temperature as the control parameter. One has to use another quantity that is measurable in individual events. This may additionally blur the phase transition signals.

In nuclear multifragmentation studies, particular attention has been paid to the largest fragment size (mass or charge), which is expected to play the role of the order parameter, thus providing a better insight into phase behavior of investigated systems [12,13,17–23]. In particular, recent percolation studies have shown that statistical measures of the largest cluster size distribution, the skewness, K_3, and the kurtosis, K_4, provide a robust signal of the percolation transition [24].

The pseudocritical point in finite systems is indicated by the zero crossing of K_3 coinciding with a minimum of K_4. This signature is applicable even to very small systems and can be tested with various measurable event sorting variables. Therefore, it is well suited for applications to nuclear multifragmentation.

The primary objective of this thesis work is the study of phase transition in nuclear multifragmentation by examining properties of the largest fragment size distributions (event-to-event fluctuations) with the cumulant analysis suggested by the percolation results. This new method is applied to statistical multifragmentation models containing a liquid-gas phase transition and to ALADIN experimental data on spectator fragmentation at relativistic energies.

The thesis is organized as follows.

Chapter 2 shortly describes theoretical predictions on the phase diagram of nuclear matter and the relation of multifragmentation processes to the bulk liquid-gas phase transition.

Chapter 3 briefly overviews experimental investigations of nuclear multifragmentation in the context of phase transitions.

Chapter 4 is devoted to model studies, focusing on the cumulant properties of the largest fragment size distribution. After recalling the percolation results, the studies are extended to statistical models: the Canonical Thermodynamic Model (CTM) [25] and the Copenhagen Statistical Multifragmentation Model (SMM) [26].

Chapter 5 examines the fragment charge distributions and correlations measured in fragmentation of Au projectiles at relativistic energies in the ALADIN experiment [27]. Extensive quantitative comparisons with predictions of the bond percolation are performed. They concern not only the largest fragment charge distributions, but the whole fragmentation pattern is verified in detail. In addition, the model is used to evaluate effects of secondary decays on the cumulant properties, and to test the relevance of phase transition signals.

In Chapter 6 the cumulant analysis of the largest fragment charge distributions is applied to the ALADIN S254 experimental data to investigate the isotopic dependence of the break-up transition. The experiment was conducted with neutron-rich ^{124}Sn and radioactive neutron-poor ^{107}Sn and ^{124}La beams of 600 MeV/nucleon incident energy and natural Sn targets [28, 29]. The experimental results are compared to calculations performed with the Statistical Multifragmentation Model. In addition, the derived transition temperatures are confronted with predictions of the thermodynamic and Hartree–Fock models.

Summary and conclusions are presented in Chapter 7.

Author's contribution:

The thesis author developed software for calculations within the Canonical Thermodynamic Models, performed SMM simulations and the theoretical data analysis presented in Chapter 4.

Chapter 5 includes material from the published article [30]:
J. Brzychczyk, T. Pietrzak, A. Wieloch, W. Trautmann, *Distributions of the largest fragment size in multifragmentation: Traces of a phase transition*, Phys. Rev. C 98, 054606 (2018).
The author significantly contributed to this work by taking part in the experimental data analysis and percolation simulations. In particular, the author checked whether the investigated observables are independent of the projectile energy and the target nucleus for the applied event sorting, examined the Fisher and Zipf power laws, and performed model simulations for the bimodality tests.

The results presented in Chapter 6 have been published in the article [31]:
T. Pietrzak *et al.*, *The percolation phase transition and statistical multifragmentation in finite systems*, Phys. Lett. B 809, 135763 (2020).
The author performed the cumulant analysis of the experimental data and model calculations. Preliminary results of this work were presented at the International

Workshop on Multifragmentation and Related Topics (IWM2009) in Catania and published in the conference proceedings:
T. Pietrzak *et al.*, *Tracing a phase transition with fluctuations of the largest fragment size: Statistical multifragmentation models and the ALADIN S254 data* [32].

Chapter 2

Nuclear multifragmentation and the liquid-gas phase transition

Since the radial part of the nuclear force is similar to the van der Waals interaction, the nuclear matter is expected to present a liquid-gas phase transition [1]. This was corroborated in a variety of theoretical studies, which predict a liquid-gas phase coexistence region at low densities (below the normal nuclear density) with a critical density ρ_c around one-third of the normal nuclear density ρ_0 and a critical temperature $T_c \simeq 14 \div 18$ MeV for the symmetric nuclear matter [33–37]. The symmetric nuclear matter refers to an infinite uniform system of nucleons with equal neutron and proton densities, interacting only through the strong force (the Coulomb interaction is neglected). The predictions were based on microscopic approaches such as the temperature-dependent Hartree-Fock or relativistic mean-field models. As an example,

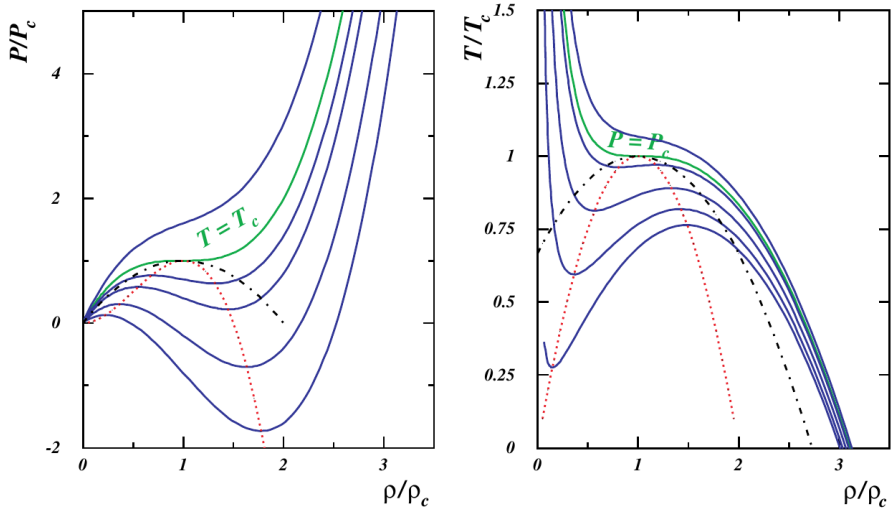

Figure 2.1: Equation of state relating the pressure (left) or the temperature (right) and the density (normalized to critical values) in symmetric nuclear matter. The solid lines represent isotherms (left) and isobars (right). The dash-dotted lines delimit the coexistence region and the dotted lines the isothermal spinodal region. Figure from [38].

Fig. 2.1 shows results of Hartree-Fock calculation with a Skyrme force for nucleon-nucleon interaction [38]. The dash-dotted line is the coexistence curve

determined from the Maxwell construction. The region below this line indicates conditions at which the liquid and gas phases can coexist in thermodynamic equilibrium. The dotted line is the upper boundary of the isothermal spinodal region corresponding to the negative isothermal compressibility (decreasing parts of isotherms in Fig. 2.1). In this region a homogeneous system is mechanically unstable with respect to density fluctuations and breaks into separate phases of gas and liquid. The spinodal and coexistence lines converge at the critical point, where the first-order phase transition becomes a second-order one. A metastable one-phase state may exist within the area between the spinodal and coexistence curves. The metastable state separates into two-phase stable liquid–gas mixture by nucleation of liquid droplets in supersaturated vapor (at low densities $\rho < \rho_c$) or by nucleation of vapor bubbles in superheated liquid (at higher densities $\rho > \rho_c$).

The phase diagram of asymmetric nuclear matter with different neutron-to-proton ratios was studied in detail within the framework of a relativistic mean-field model by Müller and Serot [33]. Figure 2.2 compares the coexistence and spinodal curves for

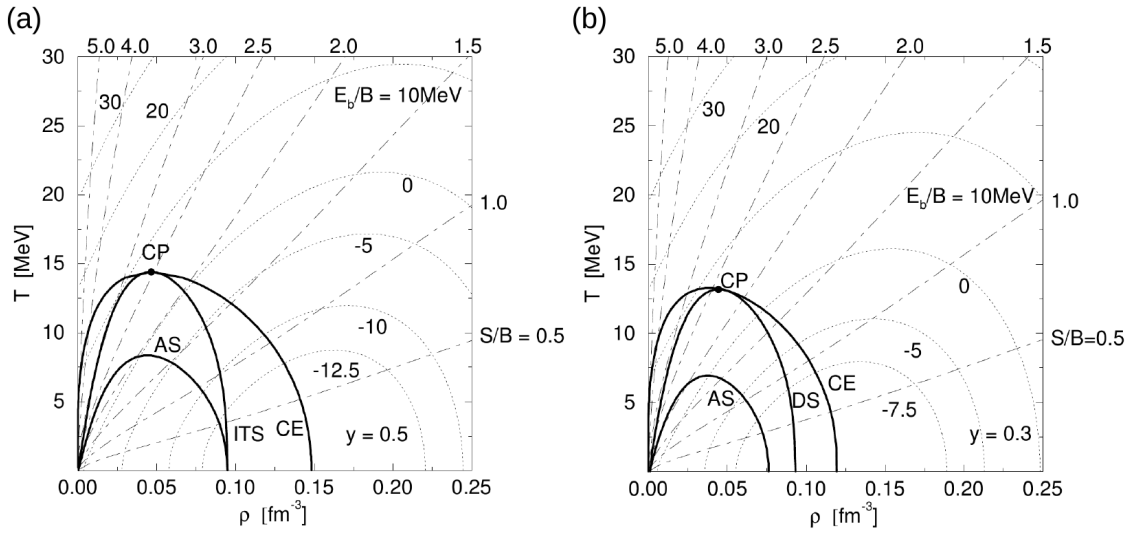

Figure 2.2: Phase diagram of symmetric nuclear matter (a) and of asymmetric matter with proton fraction $y = 0.3$ (b) in the temperature-density plane. The solid lines depict the coexistence curve (CE), the isothermal spinodal (ITS), the adiabatic spinodal (AS), and the diffusive spinodal (DS). The critical point is denoted by CP. The dotted lines are contours of equal energy per baryon, and adiabats are shown as dot-dashed lines. Figure from [33].

symmetric nuclear matter (left diagram) and asymmetric nuclear matter with a proton fraction of $y = 0.3$ (right diagram). In the case of isospin-asymmetric matter the coexistence region is reduced and its structure is more complex. It additionally contains the diffusive spinodal associated with the chemical instability, i.e., the instability with respect to fluctuations in the neutron/proton concentration. The phase separation in asymmetric nuclear matter can be therefore driven by a combination of mechanical and chemical instabilities. Due to the higher dimensionality of the binodal surface, the transition is suggested to be of second-order. The neutron/proton compositions of the coexisting liquid and gas phases are predicted to be different, the liquid is closer to

symmetry whereas the gas is enriched in the more abundant species. This effect, being a consequence of the increasing symmetry energy with density, is often referred to as isospin fractionation or distillation [39–41].

Collisions with heavy ions provide the possibility of investigating nuclear matter far away from normal conditions. In particular, the multifragmentation process allows to probe the nuclear phase diagram at moderate temperatures and low densities. In the most popular scenario of multifragmentation, a hot nuclear system created in a nuclear collision expands due to the internal thermal pressure and after reaching the liquid-gas coexistence zone disintegrates into fragments through spinodal decomposition or nucleation, as it is schematically illustrated in Fig. 2.3. Such a thermodynamic description assumes that the

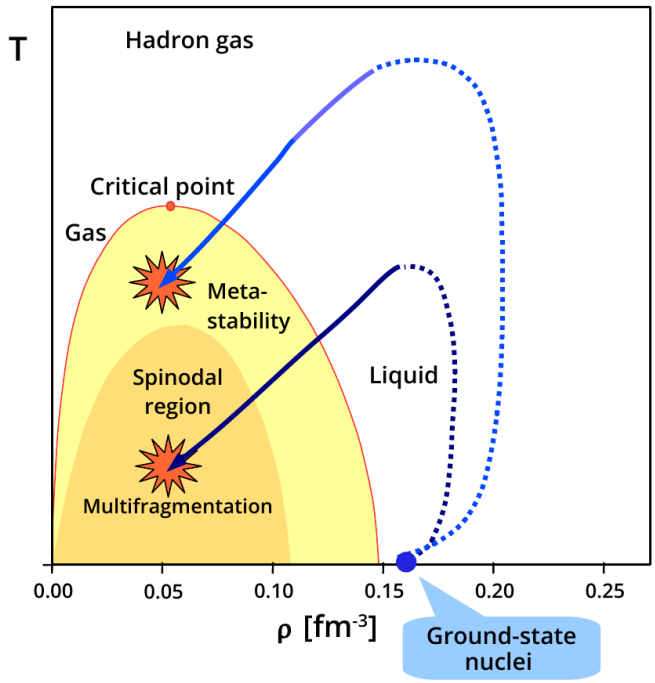

Figure 2.3: Sketch of collision trajectories in the temperature-density plane leading to the liquid-gas coexistence region where the system undergoes multifragmentation by spinodal decomposition or nucleation in the metastable regime.

excited system equilibrates faster than it expands and cools. The light fragments such as single nucleons and light charged particles are considered as gas while the intermediate mass fragments and heavy residues (if present) are treated as liquid droplets. Then the excited fragments undergo sequential decay into cold secondary fragments.

In finite nuclear systems, the phase transition is substantially modified due to the presence of surface and Coulomb effects. Surface effects can reduce the critical temperature by $2 \div 6$ MeV while the Coulomb force is responsible for a further reduction of $1 \div 3$ MeV [35, 42, 43]. The estimated temperatures depend on the method and the size of the studied system. For example, according to calculations with the fermionic molecular dynamics model performed for the ^{16}O nucleus, the critical temperature deduced from observing the disappearance of the liquid-gas coexistence is about 10 MeV [44]. A somewhat larger value, $T_c \simeq 12$ MeV, has been concluded from a study of a system of mass number $A = 36$ with the antisymmetrized molecular dynamics [45].

Levit and Bonche studied the stability of hot charged nuclei (or liquid drops) immersed in a vapor of free nucleons by employing a temperature-dependent Hartree-Fock model with Skyrme interactions [46]. They showed that below a certain limiting temperature, $T_{\rm lim}$, the nucleus can exist in equilibrium with the surrounding vapor, but above $T_{\rm lim}$ the nucleus is unstable and will break into pieces. This is the so called Coulomb instability in finite nuclei. The limiting temperature values calculated within this approach [47] are presented in Fig. 2.4. They vary considerably with the mass and isospin-asymmetry of the compound nucleus but are always much lower than the critical temperature of infinite

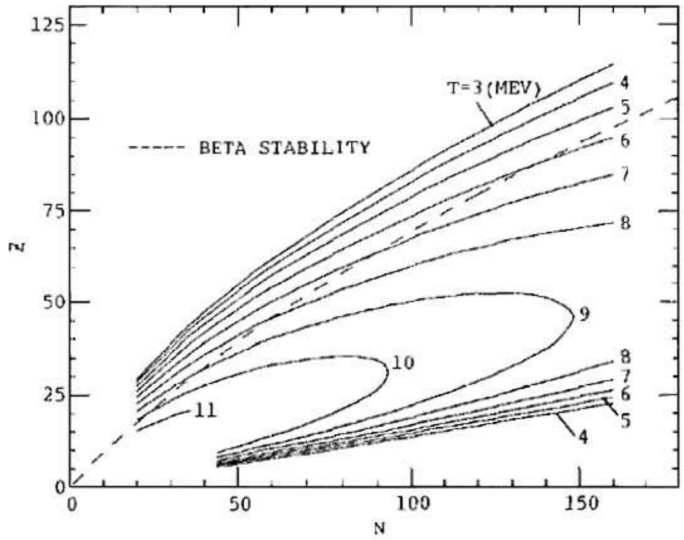

Figure 2.4: Limiting temperatures as a function of the number of protons Z and neutrons N as predicted by Besprosvany and Levit [47].

nuclear matter. The Coulomb instability of hot nuclei was also studied in later works with other models using different kinds of the effective nucleon-nucleon interaction [48–55]. It was found that the values of $T_{\rm lim}$ are very sensitive to the chosen nuclear interaction and to the assumed temperature dependence of the surface tension. In particular, Song and Su derived relations between the limiting temperature and the critical temperature of nuclear matter for several different Skyrme interactions [49]. The limiting temperature has been often interpreted as the maximum temperature that a nucleus can sustain before multifragmentation, and therefore as an upper limit for the maximal temperature observed experimentally. However, such an interpretation may be questionable, since the excited system evolves before multifragmentation without the presence of the outer vapor.

Chapter 3

Experimental investigations of multifragmentation

In the early 1980's, the Purdue University group observed that the inclusive mass yields of the fragments produced in p+Xe and p+Kr collisions at 50 to 350 GeV followed a power law $Y(A_{\mathrm{f}}) \propto {A_{\mathrm{f}}}^{-\tau}$ with the exponent τ of about 2.6 [56, 57]. This was interpreted as a possible evidence of a liquid-gas phase transition near the critical point according to the Fisher model which describes the droplet condensation in supersaturated vapor near the critical temperature [58]. Although such an interpretation might be questionable for systems created in nuclear reactions, it aroused great interest in the multifragmentation phenomenon.

Over the next years, a substantial progress in experimental investigations of multifragmentation was achieved owing to the development of heavy-ion acceleration and particle detection techniques. In particular, advanced multidetector arrays of high efficiency with large angular coverage and high granularity (4π detectors) allowed for almost complete reaction characterization on the event-by-event basis [59]. They permit to study not only the inclusive particle yields and spectra but also the energy and angular correlations between the fragments, and observables related to the fragment charge partitions. Moreover, they provide a possibility to reconstruct the fragmenting system and to estimate its excitation energy. The development of radioactive beams have offered the unique opportunity to explore isospin dependence of multifragment decays.

Multifragmentation processes have been observed in various kinds of nuclear reactions when the excitation energy deposited in the system is comparable to the nuclear binding energy. Figure 3.1 illustrates three major classes of these reactions.

One class is central or near-central nucleus-nucleus collisions at intermediate bombarding energies ($20 \div 100$ MeV/nucleon). Calculations with microscopic transport models, such as the Boltzmann-Uheling-Uhlenbeck (BUU) and Quantum Molecular Dynamics (QMD) approaches, indicate that significantly compressed and highly excited nuclear matter is produced in the early stage of the reaction in the region of overlap between projectile and target [60]. At this stage, some energetic nucleons and light particles are emitted mostly in the forward direction (pre-equilibrium emission). Then the excited, thermalized nuclear system expands due to unbalanced mechanical and thermal pressure, and disintegrates into nucleons and fragments. Finally, the hot primary fragments propagate independently in their mutual Coulomb field and undergo

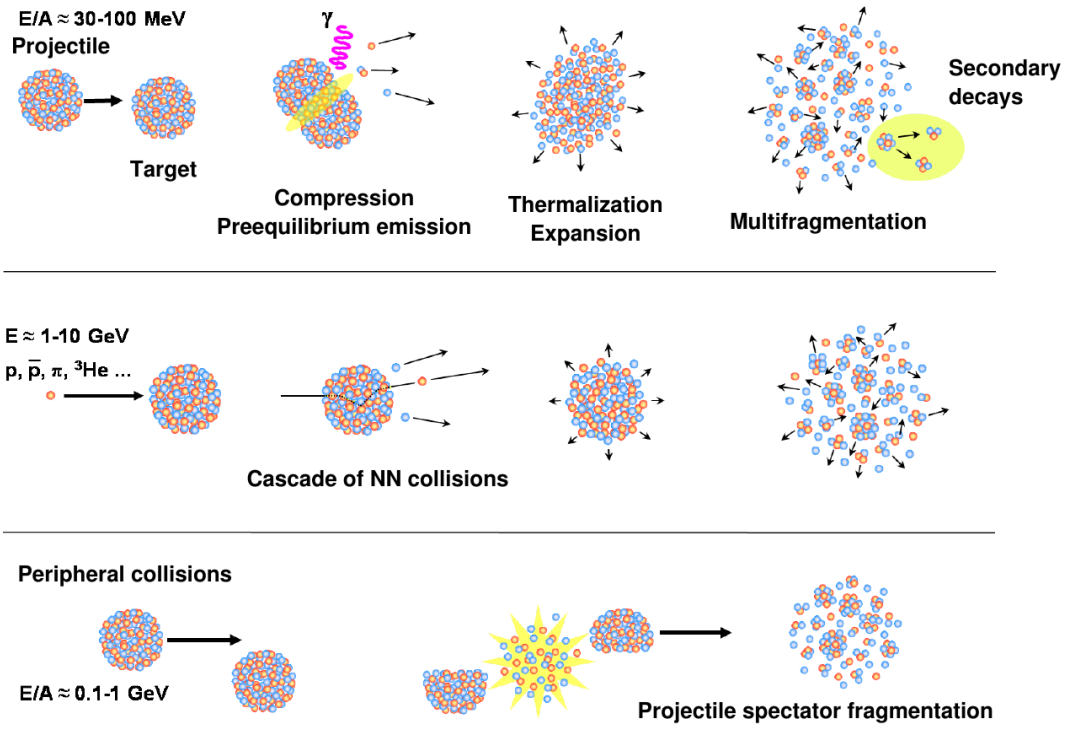

Figure 3.1: Three main types of nuclear reactions leading to multifragmentation.

secondary decays. Such reactions have been extensively investigated in several heavy-ion laboratories, especially at the Michigan State University with the MSU 4π and MINIBALL multidetectors [61–63] at the Texas A&M University with the NIMROD 4π neutron and charged-particle detection system [64], at the GANIL facility in Caen with the INDRA 4π multidetector [65] and at LNS Catania using the CHIMERA 4π multidetector [66].

Another class includes reactions induced by light particles (pions, protons, antiprotons, light ions) on heavy targets at projectile energies in the GeV range. The initial reaction dynamics can be viewed as a cascade of nucleon-nucleon and nucleon-pion collisions, during which several fast particles may be ejected from the nucleus. According to Intra-Nuclear Cascade (INC) and BUU dynamical calculations the cascade stops after about 30 fm/c. The excited heavy residue is expected to reach a state of quasi-equilibrium, and then undergoes statistical decay (via multifragmentation at sufficiently high excitation energies). Such reactions allow to investigate the thermal properties of the fragmenting system with minimal rotational and compressional effects. They were the most comprehensively studied in experiments performed at LNS Saclay and at the Brookhaven AGS with the Indiana Silicon Sphere (ISiS) 4π detector array [67]. Measurements indicate that mixtures of intermediate mass fragments (IMF's) with $3 \leqslant Z \leqslant 30$ and light particles ($Z < 3$) are emitted from hot nuclear systems expanded to sub-saturation density, on time scales consistent with a bulk disintegration (< 100 fm/c).

Multifragmentation processes have been also observed in decays of projectile-like fragments or projectile spectators in peripheral and semi-peripheral heavy-ion collisions at intermediate and relativistic energies. Such fragmenting systems are not significantly

influenced by the compression and angular momentum, similarly as in reactions induced by light particles. Projectile spectator fragmentation at relativistic energies has been investigated in a series of experiments carried out at GSI Darmstadt using the ALADIN forward-spectrometer [27]. A prominent feature of the data is that the fragment multiplicities and fragment charge correlations are independent of the projectile energy and the target nucleus when plotted as a function of Z_{bound} (the total charge of fragments with $Z \geqslant 2$) which is a measure of the spectator size being correlated with the impact parameter. This universality indicates that a high degree of equilibrium is reached prior to the fragmentation stage of the reaction.

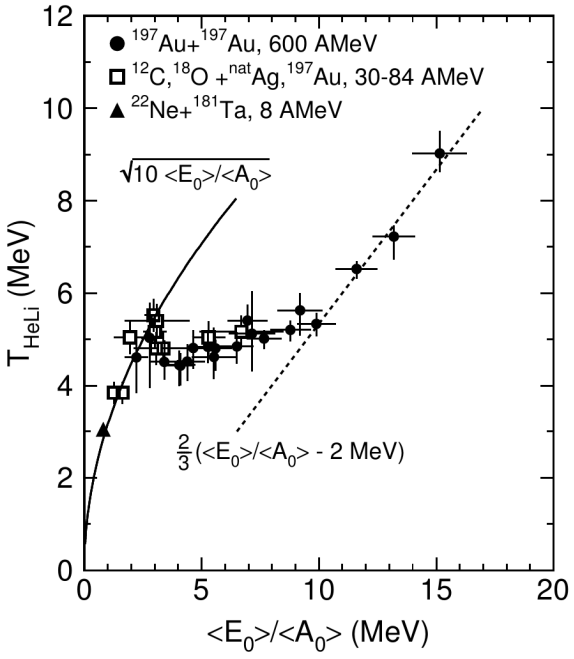

Figure 3.2: Caloric curve as the dependence of the isotope temperature T_{HeLi} on the total excitation energy per nucleon, determined by the ALADIN group from the decay of spectator nuclei [68].

Many studies have been devoted to determining the thermodynamic properties of hot nuclear systems, in particular the nuclear caloric curve, i.e., the dependence of the temperature T on the excitation energy E^*. The excitation energy is calculated event-by-event with the calorimetry method based on measurement of the total kinetic energy of particles emitted from the source [69]. The temperature can be estimated from the slope of the measured particle kinetic energy spectra, from the double ratios of isotopic yields, and/or from the population of excited states in light clusters by fitting a Boltzmann distribution [70]. The first experimental evaluation of the nuclear caloric curve was reported by the ALADIN collaboration in 1995 (see Fig. 3.2) [68]. It was derived from fragment distributions measured in Au + Au collisions at an incident energy of $E/A = 600$ MeV. The temperature values were deduced from the yield ratios of He and Li isotopes. As can be seen in Fig. 3.2 the caloric curve exhibits three distinct parts. In the evaporation regime at excitation energies below 2 MeV/nucleon, the rise of the temperature is consistent with the low-temperature approximation of a fermionic system indicated by the solid line. Within the range of excitation energies from 3 to 10

MeV/nucleon where multifragment breakup dominates, a nearly constant value for T_{HeLi} of about $4.5 \div 5$ MeV is observed. Beyond an excitation energy of 10 MeV/nucleon, the caloric curve rises approximately linearly with a slope close to that of a classical Boltzmann gas, indicating the vaporization regime. The plateau in the caloric curve was interpreted as a signature of a first-order liquid-gas phase transition. Such a behavior is predicted by statistical models of multifragmentation [26, 71] and also by molecular dynamics calculations (see e.g. [72]). A flattening or plateau-like structure in the caloric curve was observed in many measurements. As indicated in Ref. [73] the plateau temperatures can be interpreted as representing the limiting temperatures resulting from Coulomb instabilities of heated and expanded nuclei. Using a number of caloric curves obtained experimentally for different systems, Natowitz *et al.* derived the limiting temperature as a function of the system mass, which is shown in Fig. 3.3 [74]. The observed significant decrease with mass is consistent with presented model predictions. Based on these results, the authors estimated a critical temperature of $T_{\mathrm{c}} = 16.6 \pm 0.86$ MeV for symmetric infinite nuclear matter.

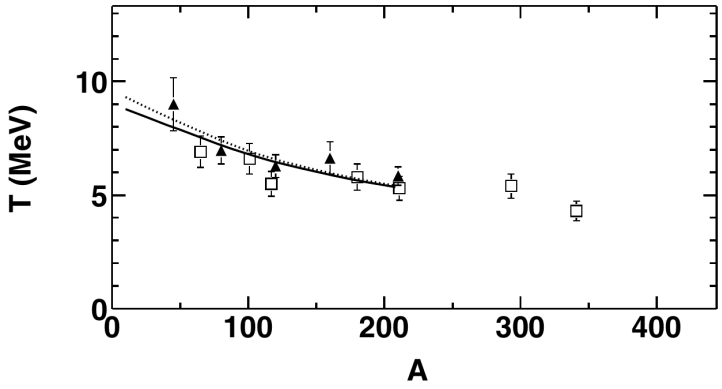

Figure 3.3: Limiting temperatures as a function of the system mass. Temperatures derived from caloric curves with double isotope ratio measurements are indicated by the solid diamonds. Temperatures obtained from thermal Bremsstrahlung measurements are indicated by the open squares. The lines represent limiting temperatures calculated using interactions proposed by Gogny [51] (dashed line), and Furnstahl *et al.* [75, 76] (solid line). Figure taken from Ref. [74].

Besides the plateau in the caloric curve, other signals characteristic of a first-order phase transition have been reported in the experimental studies, such as negative micro-canonical heat capacity, characterized by abnormal kinetic energy fluctuation [77], the "fossil" signal of spinodal decomposition, characterized by abnormal production of equally sized fragments [78], and bimodal characteristics representative of a two-phase coexistence [21, 79]. Several experimental works exploring the mass (charge) distributions have also reported various signals indicating the occurrence of critical behavior (continuous phase transition) at temperatures between 5 and 8 MeV [11, 15, 80, 81]. It should be stressed, however, that the full understanding of these signals requires further theoretical and experimental studies, due to interpretation difficulties associated with the finite size and Coulomb effects, the validity of assumptions on constant pressure or volume during phase transition in nuclei, as well as the influence of non-thermal dynamical effects.

Chapter 4

Model Studies

4.1 Largest cluster in percolation

Percolation model is a probabilistic model, introduced by S. Broadbent and J. Hammersley in 1957 to investigate whether fluids can penetrate porous media [82]. Since that time various types of the model have been developed and applied to a wide range of fields of science, such as statistical physics, physical chemistry, epidemiology, nanotechnology, materials science, communications, and economy [83, 84]. In particular, percolation is used for studying clustering phenomena in complex physical systems exhibiting phase transitions (critical behavior). It is usually formulated on a lattice, which is composed of sites (vertices) connected by bonds. Three-dimensional lattices are relevant for most physical processes.

There are two main types of percolation models: site and bond percolation. In site percolation, each site of a given lattice is randomly and independently occupied with a prescribed probability p, while each bond is considered to be connected. In bond percolation, all the lattice sites are occupied, but are either connected or not by bonds which are created randomly throughout the lattice with a given probability p. A cluster is a group of occupied sites connected by bonds. The cluster size is the number of sites in the cluster. The probability p is a model control parameter. At $p = 0$ in bond percolation, each lattice site is a cluster of size 1. As p increases, the average size of the clusters grows, and at $p = 1$ there is only one cluster of the lattice size. Figure 4.1 shows examples of bond percolation events on a finite square lattice of size $A_0 = 25$ for several values of p. Percolation events are usually generated with a Monte Carlo procedure. Statistical

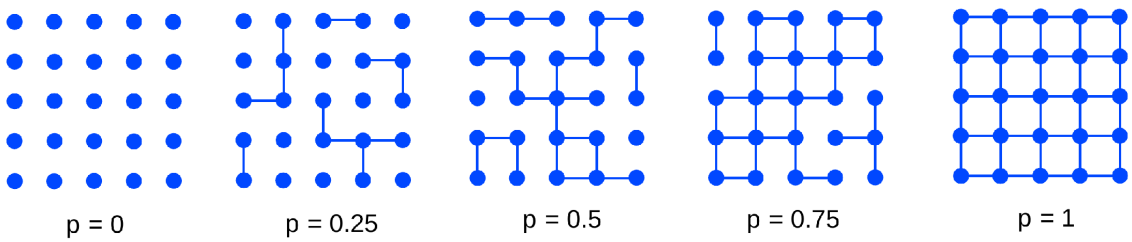

Figure 4.1: Exemplary events from bond percolation on 5×5 square lattice for various values of the bond probability p.

analysis of large samples of events allows to determine the average characteristics of

cluster sizes and to study their event-to-event fluctuations. In the continuous limit $A_0 \to \infty$, percolation exhibits a sharp continuous phase transition. There exists a critical value of probability p_c (percolation threshold) at which the properties of clusters change abruptly. For $p < p_c$ only finite clusters are present. When $p > p_c$ there exists an infinite cluster that spans across the entire lattice. The fraction of sites belonging to this spanning cluster is the order parameter. The value of the percolation threshold depends on kind of percolation (bond or site) and lattice topology. For example, in bond percolation on 2D square lattice $p_c = 0.5$, while for the 3D simple cubic lattice $p_c \simeq 0.2488$ [83].Various statistical cluster properties (e.g., the mean cluster size) exhibit singularities (divergences) at the critical point. Their behavior in approaching the critical point can be described by power laws with exponents called the critical exponents. The values of the critical exponents are the same in a given dimensionality, irrespective of the percolation and lattice type [83].These independence properties are referred to as universality.

In finite systems (lattices) the transition is smoothed. The probability that at least one cluster connects the opposite lattice sides changes gradually in the transition region. Such spanning clusters are seen in examples given in Fig. 4.1 for $p \geq 0.5$. Moreover, the divergences occurring at the critical point in the continuous limit are replaced by maxima located near p_c. Such finite-size effects can be studied with percolation by changing the system size.

Percolation models have been applied for describing the properties of nuclear fragmentation soon after first experimental evidence [57, 85, 86]. Very satisfactory reproductions of measured fragment mass/charge yields and correlations have been achieved in studies of various kinds of proton and heavy-ion induced reactions [8, 11, 87]. The results suggested that nuclei break up similar to percolation clusters with the presence of critical behavior, seemingly contradicting the first-order liquid-gas phase transition whose signatures were expected to appear in fragmentation data. In order to get a better insight into the nature of phase transition in fragmenting systems, particular attention has been paid to the largest fragments and their size (mass/charge) distributions (see, e.g., Refs. [12, 13, 17–23, 30] and references given therein). The largest fragment is expected to represent the liquid part of the system and thus to play the role of the order parameter. A transition from a "liquid" to a "gaseous" phase is associated with a rapid decrease in the largest fragment size, which may correspond to the order-parameter discontinuity in the case of a first-order phase transition or to the power-law disappearance near a second-order transition point (a critical point) in the continuous limit.

In percolation of finite systems the order parameter is the largest cluster size. Extensive studies of its distributions have been performed by J. Brzychczyk [24] Calculations presented in that article and in this work are carried out with a three-dimensional bond percolation model on simple cubic lattices [4, 83]. The sites are arranged on the lattice in the most compact configuration for an assumed the total number of sites A_0 (the system size). Events are generated using a Monte Carlo procedure. Clusters are identified with the Hoshen-Kopelman algorithm [88] and free boundary conditions are applied to account for the presence of a surface in real systems. Given a control parameter value p, the probability distribution $P(A_{\max})$ of the largest cluster size $A_{\max}$ is determined from a large sample of events.

As it was presented in Ref. [24], Fig. 4.2 illustrates the evolution of the largest cluster

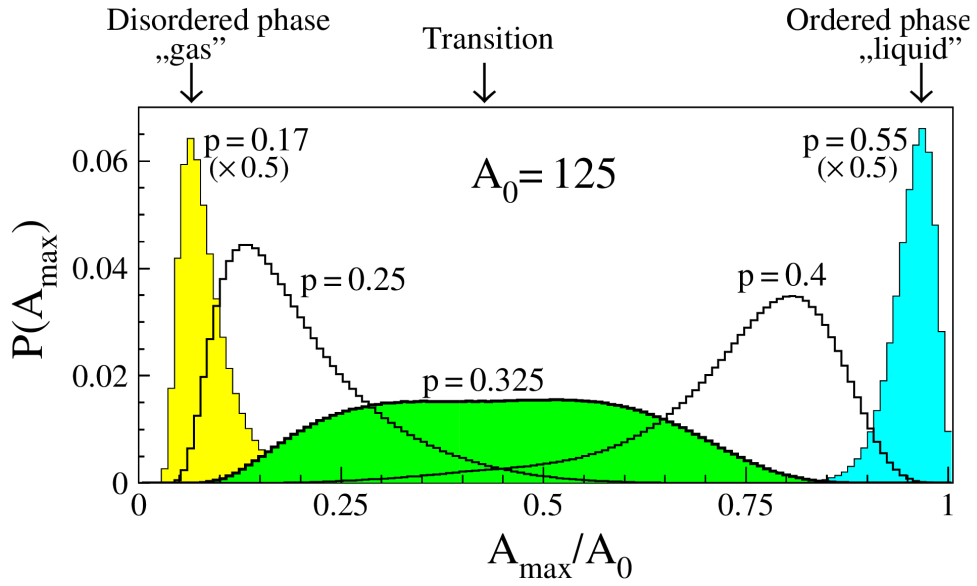

Figure 4.2: Probability distributions of the largest cluster size for a cubic lattice of size $A_0 = 5 \times 5 \times 5$ with free boundary conditions.

size distribution with the change of the bond probability p, which is representative for small lattices with open boundaries. Away from the transition at small and large values of p the distribution is sharply peaked with an extended tail to the right (left) in the disordered (ordered) phase and positioned close to the limiting values of the cluster size. In the transition region, the distribution rapidly evolves passing through a broad, flattened, and nearly symmetrical distribution. Statistical measures as the mean, variance, skewness and kurtosis contain the most significant information about the distribution. Of particular interest are the following dimensionless cumulant ratios

$$\begin{aligned} K_2 &\equiv \mu_2 / \langle A_{\max} \rangle^2 &&= \kappa_2 / \kappa_1^2 \\ K_3 &\equiv \mu_3 / \mu_2^{3/2} &&= \kappa_3 / \kappa_2^{3/2} \\ K_4 &\equiv \mu_4 / \mu_2^2 - 3 &&= \kappa_4 / \kappa_2^2, \end{aligned} \tag{4.1}$$

where $\langle A_{\max} \rangle$ denotes the mean value, $\mu_i = \langle (A_{\max} - \langle A_{\max} \rangle)^i \rangle$ is the ith central moment, and κ_i is the ith cumulant of $P(A_{\max})$. K_2 is the variance normalized to the squared mean, K_3 is the skewness indicating the distribution asymmetry, and K_4 is the kurtosis excess measuring the degree of peakedness. The cumulants are functions of the central moments with $\kappa_1 = \langle A_{\max} \rangle$, $\kappa_2 = \mu_2$, $\kappa_3 = \mu_3$, and $\kappa_4 = \mu_4 - 3\mu_2^2$. In the transition region, these quantities obey with good accuracy finite-size scaling relations even for very small systems with open boundaries [24]. This permits the identification of universal (independent of the system size) features of K_i at the percolation transition.

The form of observed universality can be illustrated with Fig. 4.3 where the cumulant ratios K_i are plotted as a function of the bond breaking probability $p_b \equiv 1 - p$ for three different system sizes. Increasing p_b corresponds to increasing temperature in physical systems in which the temperature is a control parameter, as it is expected for nuclear multifragmentation. The location of the critical point in the continuous limit $p_c \simeq 0.751$ is indicated by the vertical long line. According to the finite-size scaling, the values of

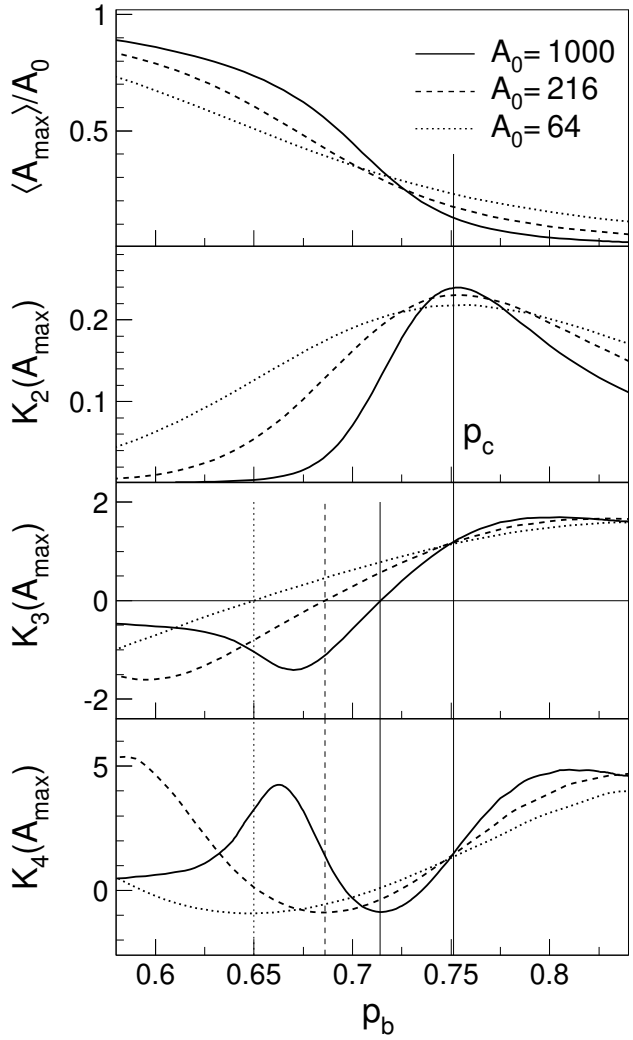

Figure 4.3: The normalized mean largest fragment size $A_{\max}$ and the cumulant ratios of Eqs.(4.1) as a function of the bond breaking probability $p_{\rm b}$, as obtained with bond percolation for three different system sizes $A_0 = 64$, 216, and 1000. The long vertical line indicates the critical point $p_{\rm c}$ in the continuous limit. The short lines indicate the transition (pseudocritical) points for the finite systems. Figure adapted from [31].

the cumulants $K_{\rm i}$ at $p_{\rm c}$ are expected to be independent of the system size. This is quite precisely observed in Fig. 4.3 as the crossing of the curves. A prominent feature of K_2 is its maximum located very close to $p_{\rm c}$. The maxima of other quantities used often as criticality signals (e.g., the maximum variance of the fragment mass distribution) show much larger deviations from $p_{\rm c}$ (see examples given in [24]). The transition point in finite systems can be associated with the broadest and most symmetric $P(A_{\max})$ distribution observed near the pseudocritical point defined by the maximum of the mean cluster size being the analog of the susceptibility [24]. This transitional distribution is indicated by $K_3 = 0$ and the minimum value of K_4 of about -1.

It is very important for analysis of experimental data that the cumulant features characterizing the critical and pseudocritical points are approximately preserved for the corresponding points when events are sorted by measurable variables correlated with the

control parameter, such as the total multiplicity or the total mass of complex fragments. Near-critical events are indicated by the maximum of K_2 while events associated with the pseudocritical point are characterized by $K_3 = 0$ and the minimum value of K_4 of about -1. These new signatures of the transition points are the subject of further studies within models of statistical multifragmentation and will be applied for analysis of the ALADIN experimental data.

4.2 Thermodynamic model predictions

The Canonical Thermodynamic Model (CTM) is a statistical model applied for describing the clustering in nuclear multifragmentation [25]. This model assumes that the hot nuclear system expands to a freeze-out volume where it breaks up into fragments (composites) in thermal equilibrium. In the freeze-out volume, the nuclear interaction between different composites is neglected, and the probability of different channels is calculated according to the availability of phase space. The model allows fast computing of the partition function in the canonical ensemble using a recursion method, and thus to obtain the thermodynamic properties of the system.

CTM was initially formulated for one kind of particles (nucleons) [17]. This simplified one-component model permits exact calculations for systems with large number of particles, as required for phase transition studies. The presence of a first-order phase transition has been established [17, 25, 89]. With the extension to two kinds of particles (neutrons and protons) [90] the model is similar to the Copenhagen Statistical Multifragmentation Model (SMM) [26] which is more general but requires complicated and time-consuming Monte-Carlo sampling. In typical physical applications the two models predict very similar results [91].

4.2.1 One-component Canonical Model

The canonical partition function of a closed system consisting of A identical particles of only one kind at temperature T can be written as

$$Q_{\mathrm{A}} = \frac{1}{\mathrm{A!}}(\omega)^A \tag{4.2}$$

where ω is the partition function of one particle. The $A!$ term in the denominator accounts for particle indistinguishability. In the case of a spinless particle with no internal structure

$$\omega = \frac{V_a}{h^3}(2\pi mT)^{3/2} \tag{4.3}$$

where m is the particle mass, V_{a} is the volume available for the particle centre of mass motion, and h is the Planck's constant.

In the one-component CTM, all particles in a system, which is composed of A_0 nucleons, are represented by monomers, dimers, trimmers, etc. (single nucleons and their various clusters). A system containing n_1 monomers, n_2 dimers, n_3 trimmers, etc. is characterized by the vector $\vec{n} = (n_1, n_2, n_3, ...)$ called a channel. The system partition function is given

by

$$Q_{A_0} = \sum \prod_{i} \frac{(\omega_i)^{n_i}}{n_i!} \tag{4.4}$$

where ω_i is the partition function of a composite which has i nucleons. The sum runs over all channels that satisfy the mass conservation

$$A_0 = \sum_{i} i \times n_i \tag{4.5}$$

The one-body partition function ω_i is a product of two parts

$$\omega_i = \frac{V_a}{h^3}(2\pi m_0 iT)^{3/2} \times q_i \tag{4.6}$$

where the first part arises from the translational motion of the composite and the second one, q_i, is the internal partition function. Here m_0 denotes the nucleon mass. The volume available to the particles for the centre of mass motion V_a is less than the system's total volume V interpreted as the volume to which the nuclear system has expanded at break up (the freeze-out volume). It is assumed that the excluded volume is constant, independent of the channel, and $V_a = V - V_0$ where $V_0 = A_0/\rho_0$ with ρ_0 being the normal nuclear density. For more precise calculations, however, the multiplicity of fragments should be taken into account [92]. The assumptions that fragments are well separated and the excluded volume is independent of multiplicity will fail for non-dilute systems. Therefore, the model is restricted (somewhat arbitrarily) to volumes $V \geq 2V_0$ or to the system average density $\rho \leq 0.5\rho_0$. This is not a significant limitation because there are experimental indications that the freeze-out volume V is around $3V_0$ [26, 92, 93].
Such a value, $V = 3V_0$, was used in all simulations presented in the following, unless otherwise specified.

The internal partition function $q_i = 1$ for $i = 1$, and for $i \geq 2$

$$q_i = \exp(-F_i/T) \tag{4.7}$$

where F_i is the intrinsic free energy at freeze-out, which is approximated using the Fermi-gas model

$$F_i = -W_0 i + \sigma(T) i^{2/3} + i\frac{T^2}{\varepsilon_0} - 2i\frac{T^2}{\varepsilon_0} \tag{4.8}$$

As in Ref. [26], $W_0 = 16$ MeV is the volume energy per nucleon, $\sigma(T)$ is a temperature-dependent surface energy coefficient and ε_0 is a constant parameter. The surface coefficient at zero temperature $\sigma(T = 0) \equiv \sigma_0 = 18$ MeV as in the Bethe-Weizsäcker mass formula. With increasing temperature the surface tension decreases, vanishing at the critical temperature taken as $T_c = 18$ MeV. For temperatures below the critical temperature, $\sigma(T)$ is expressed by the formula

$$\sigma(T) = \sigma_0 \left(\frac{T_c^2 - T^2}{T_c^2 + T^2}\right)^{5/4} \tag{4.9}$$

The constant ε_0 in Eq. (4.8) can be interpreted as a parameter determining the fraction of the total thermal energy transferred into the internal excitation of fragments. The value of ε_0 is assumed to be 16 MeV as for the ideal Fermi gas at normal nuclear matter density [26].

The probability of occurrence of a given channel $P(\vec{n}) = P(n_1, n_2, n_3, n_4, ...)$ is

$$P(\vec{n}) = \frac{1}{Q_{A_0}} \prod_{\mathrm{i}} \frac{(\omega_{\mathrm{i}})^{n_{\mathrm{i}}}}{n_{\mathrm{i}}!} \tag{4.10}$$

and the average number of fragments with i nucleons can be calculated as

$$\langle n_{\mathrm{i}} \rangle = \frac{Q_{A_0 - i}}{Q_{A_0}} \omega_{\mathrm{i}} \tag{4.11}$$

From this and Eq. 4.5 one can derive a recursion relation

$$Q_{A_0} = \frac{1}{A_0} \sum_{\mathrm{k}=1}^{A_0} k \omega_k Q_{A_0 - k} \tag{4.12}$$

which allows computing the partition function in a short time even for large ($A \sim 10^3$) systems, and obtain all relevant thermodynamic quantities.

The mean energy of one fragment with k nucleons can be calculated as

$$E_{\mathrm{k}} = T^2 \frac{\partial ln(\omega_k)}{\partial T} = \frac{3}{2} T + k(-W_0 + \frac{T^2}{\varepsilon_0}) + \sigma(T) k^{2/3} - T \frac{\partial \sigma(T)}{\partial T} k^{2/3} \tag{4.13}$$

In this equation, the first term comes from the center of mass motion and the remaining ones from the internal partition function. The average energy of the whole system can be calculated from the temperature dependence of the partition function or by summing up the mean fragment energies

$$\langle E \rangle = T^2 \frac{1}{Q_{A_0}} \frac{\partial Q_{A_0}}{\partial T} = \sum_{\mathrm{k}=1}^{A_0} E_{\mathrm{k}} \langle n_{\mathrm{k}} \rangle \tag{4.14}$$

The excitation energy $\langle E^* \rangle$ is the difference between the total energy $\langle E \rangle$ and the ground state energy $E(gr)$ that is calculated for mass number A_0 using the liquid-drop formula

$$\langle E^* \rangle = \langle E \rangle - E(gr) = \langle E \rangle - (-W_0 A_0 + \sigma_0 A_0^{2/3}) \tag{4.15}$$

Figure 4.4 shows an example of the caloric curve plotted as the average excitation energy per nucleon versus the temperature that is the control parameter in the canonical model. Near the temperature of 6.5 MeV, the caloric curve exhibits a sharp increase (plateau-like behavior when plotted as T vs. E^*), which is a characteristic signature of a first-order phase transition in finite systems. The point of the fastest increase corresponds to a

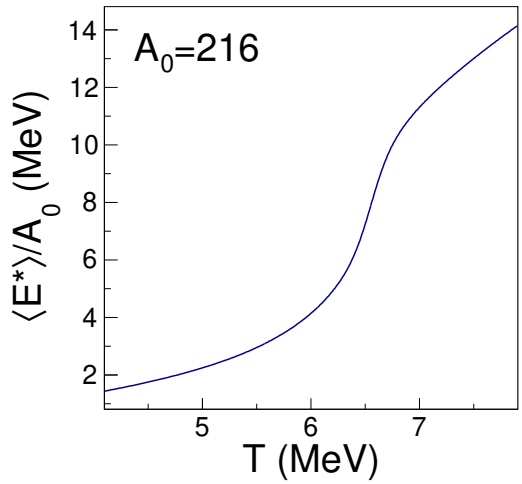

Figure 4.4: Caloric curve for a system with 216 nucleons.

maximum of the specific heat C_V

$$C_V = \left(\frac{\partial (E/A_0)}{\partial T} \right)_V \tag{4.16}$$

Here, the specific heat is the heat capacity per nucleon, which is a dimensionless quantity since the temperature is in energy units (MeV). For the canonical ensemble the specific heat at constant volume is a second derivative of the free energy F. In the case of first-order phase transition, the second derivative is a derivative of a discontinuous quantity and C_V diverges to infinity in the thermodynamic limit. In a finite system where the transition is smoothed, the divergence is replaced by a peak. Examples of such peaks for various system sizes will be shown in Fig. 4.6.

The pressure can be calculated as

$$p = T \frac{\partial ln Q_{A_0}}{\partial V_a} = \frac{T}{V_a} \sum_i^{A_0} \langle n_i \rangle \tag{4.17}$$

It allows determining the isotherms at various temperatures in the pressure versus density plane, as shown in Fig. 4.5 for systems with 64, 216, and 1000 nucleons. One can clearly see that for larger systems the isotherms present a back bending (related to a mechanical instability), which is characteristic of the first-order liquid-gas phase transition.

Of particular interest in this work are properties of the largest fragment size. For this purpose one needs to derive the probability $P(A_{max})$ that the largest cluster is A_{max} in fragmentation of a system of size A_0. Let's define

$$Q_{A_0}(k) \equiv Q_{A_0}(\omega_1, \omega_2, ..., \omega_k, 0, ..., 0) \tag{4.18}$$

as the partition function Q_{A_0} calculated with $\omega_1, \omega_2, ..., \omega_k, 0, 0, ...$, i.e. when all ω_i with $i > k$ are set to zero. In this ensemble there are no channels with clusters having more than k nucleons, and thus the largest cluster may be of any size less or equal to k.

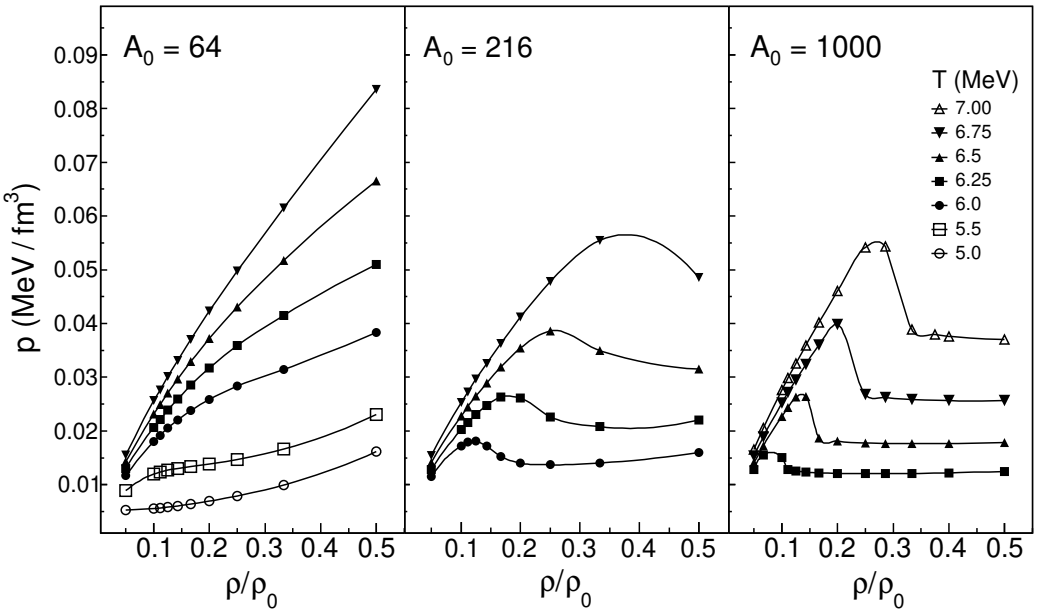

Figure 4.5: Pressure vs density isotherms for indicated system sizes.

The difference

$$\Delta Q_{\mathrm{A}_0}(k) \equiv Q_{\mathrm{A}_0}(k) - Q_{\mathrm{A}_0}(k-1) \tag{4.19}$$

represents the total partition function for the ensemble of all channels in which the largest cluster has exactly k nucleons. Therefore, the probability that the largest cluster has k nucleons is

$$P(A_{\max} = k) = \frac{\Delta Q_{A_0}(k)}{Q_{A_0}(\omega_1, \omega_2, ..., \omega_{A_0})} \tag{4.20}$$

Once the probability distribution of the largest fragment size is determined, one can calculate the mean value and higher order statistical measures of this distribution using Eqs. (4.1).

Figure 4.6 shows the largest fragment size distributions as a function of the temperature in the transition region where a peak of the specific heat is observed for different system sizes. As can be seen in the top panel, with increasing system size the C_V peak becomes sharper and higher, as well as shifted towards larger temperatures. In the thermodynamic limit, the transition location is expected at $T \simeq 8$ MeV as calculated within the grand canonical approach and shown in Fig. 4 of Ref. [89]. In this model, the critical temperature is assumed to be $T_c = 18$ MeV. The location of the specific heat maximum indicates the transition point (temperature) in finite systems. At low temperatures, below the transition, the largest fragment size is comparable to the system size. This corresponds to evaporation regime in nuclear reactions in which the system is created with low excitation energy and then decays via emission of few nucleons and/or light particles leaving a heavy remnant. At higher temperatures, after passing the transition point, the system disintegrates into many light and intermediate mass fragments, leading to a rapid decrease of the largest fragment size. As seen in the bottom panel, $\langle A_{\max} \rangle$ shows the fastest decrease at the transition point. A step discontinuity develops with

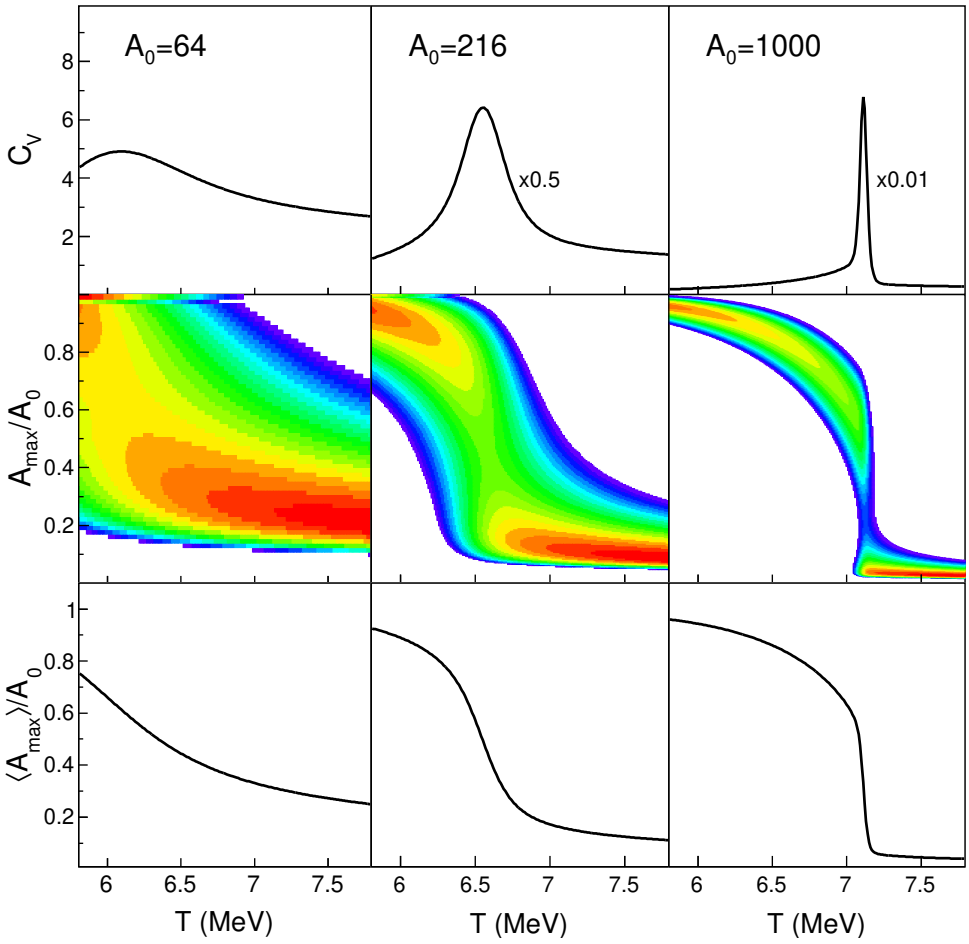

Figure 4.6: From top to bottom: the specific heat, the largest cluster size probability distribution, and its average value as functions of the temperature for systems with 64, 216 and 1000 nucleons. The probabilities shown in the middle panel are indicated by a logarithmic color scale going from blue (minimum) to red (maximum).

increasing system size, which is characteristic of the order parameter behavior at a first-order phase transition [32].

The cumulant ratios K_3 and K_4 of Eqs. (4.1) as functions of the temperature are shown in Fig. 4.7. The transition temperatures for systems with 64, 216, and 1000 nucleons, derived from the locations of the specific heat maximum, are 6.09, 6.55, and 7.11 MeV, respectively. These values are marked by the dotted vertical lines. As can be seen, the transition point is precisely indicated by $K_3 = 0$ and the minimum of K_4, similarly to the percolation case. A comparison between the CTM and percolation results is presented in Fig. 4.8. Although the K_3 and K_4 characteristics at the transition points are similar in both models, the shapes of the $P(A_{\max})$ distribution are significantly different as shown in Fig. 4.9. In CTM a bimodal structure of the distribution is observed as expected for a first-order phase transition in the canonical ensemble. A distinct bimodality appears for a system as large as $A_0 = 1000$, and the two-peak structure gradually vanishes as the system size decreases.

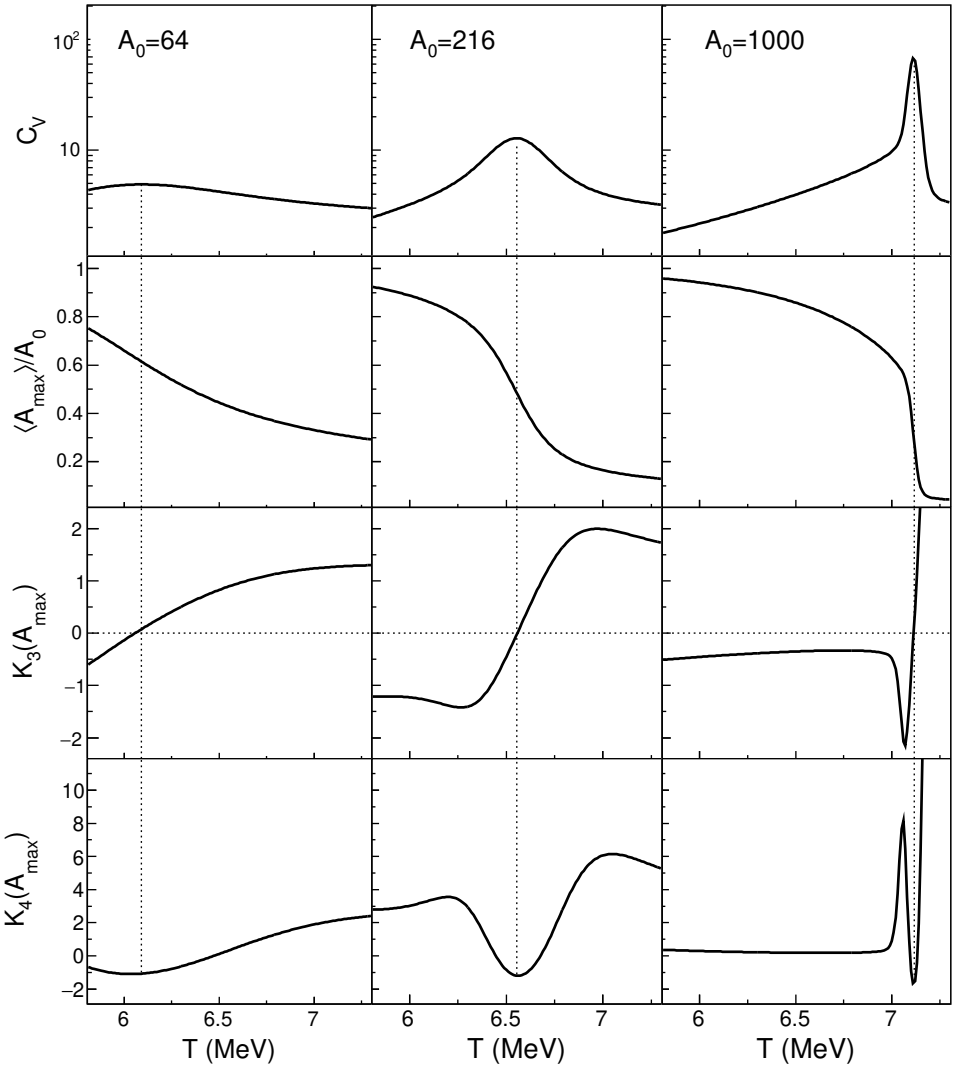

Figure 4.7: From top to bottom: the specific heat, the mean, skewness and kurtosis of the largest fragment size distribution as a function of the temperature for three system sizes.

The above examples illustrate that the transition point in small systems, associated with a phase transition in the thermodynamic limit, is well indicated by $K_3 = 0$ together with a minimum of K_4 for both, i.e. first- and second-order, types of transition. The comparisons suggest that some evidence for the transition order can be obtained from the shape of $P(A_{\max})$ and evolution of the cumulants with the system size. In particular, in the vicinity of the transition point the cumulants exhibit maxima whose amplitudes increase with the system size in the case of the thermodynamic model. This is in contrast to percolation where the amplitudes are bounded according to the second-order finite-size scaling, which is particularly clearly seen in Fig. 4.8 for the normalized variance K_2.

A bimodal pattern of the correlation between the largest and second-largest fragment sizes has also been proposed as a signature of a first-order phase transition [94, 95].

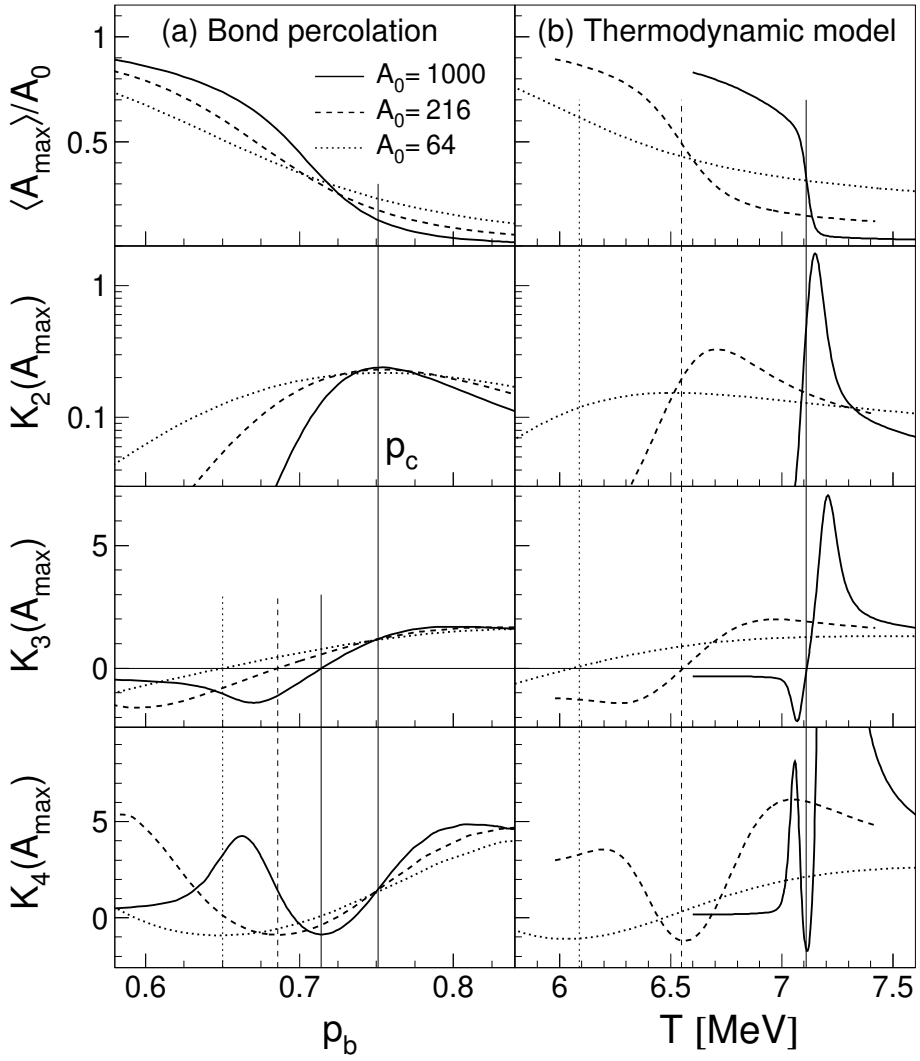

Figure 4.8: Cumulants of $P(A_{\max})$ for three system sizes. (a) Percolation results plotted as a function of the bond-breaking probability. The long vertical line indicates the critical point p_c in the continuous limit. Short lines indicate the transition (pseudocritical) points for the finite systems. (b) Results from the thermodynamic model as a function of the temperature. Vertical lines mark the transition temperatures corresponding to the maximum specific heats of the three systems. For $A_0 = 1000$, the kurtosis excess K_4 reaches a maximum value of 78 at $T \simeq 7.2$ MeV (bottom right panel).

In order to investigated this with CTM one has to get the probability $P_{A_0}(A_{max}, A_2)$ that in fragmentation of a system of size A_0 the largest fragment is of size $A_{\max}$ and the second-largest fragment is of size A_2. There are two cases to be considered:
First, if $A_2 < A_{\max}$, $(A_{\max} + A_2 \leq A_0)$ then

$$P_{\mathrm{A_0}}(A_{\max}, A_2 < A_{\max}) = \frac{\Delta Q_{\mathrm{A_0 - A_{max}}}(A_2) \cdot \omega_{\mathrm{A_{max}}}}{Q_{\mathrm{A_0}}} \tag{4.21}$$

The partition functions are calculated in a similar way as for $A_{\max}$.

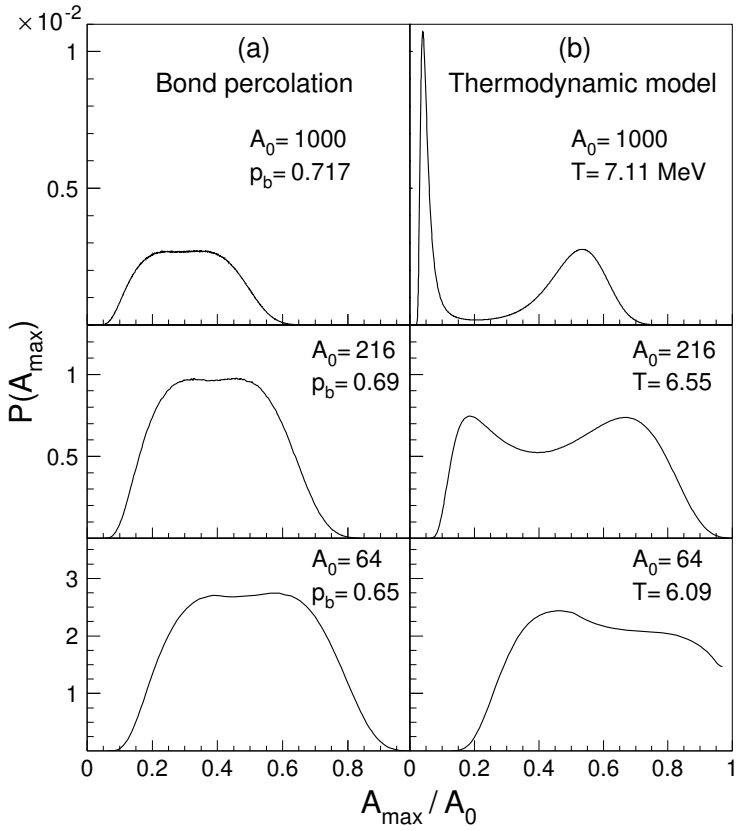

Figure 4.9: Probability distributions of the largest fragment size at the transition points.

Second case, if $A_2 = A_{\max}$ then

$$P_{\mathrm{A}_0}(A_{\max}, A_2 = A_{\max}) = \frac{\Delta Q_{\mathrm{A}_0}(A_2) - Q_{A_0 - A_2}(A_2 - 1) \cdot \omega_{A_2}}{Q_{A_0}} \tag{4.22}$$

The first term in the subtraction is the total partition function for the channels where the largest cluster size is A_2 but the number of such clusters can be one or more. The second term is the total partition function for the channels in which there is only one cluster of size A_2 being the largest one.

The upper panel in Fig. 4.10 illustrates the correlation between the two largest fragment sizes at and near the transition temperature $T = 6.55$ MeV in the system consisting of 216 nucleons. The bottom panel shows another representation of this correlation: $A_{\max}$ as a function of the asymmetry parameter defined as

$$\eta \equiv \frac{A_{\max} - A_2}{A_{\max} + A_2} \tag{4.23}$$

At $T = 6$ MeV, below the transition temperature, almost the entire mass of the system is contained in one large fragment, identified with the liquid phase. Above the transition, at $T = 7$ MeV, the system contains only small fragments, which is identified with the gas phase. The plots reveal that these two types of channels are simultaneously present at the

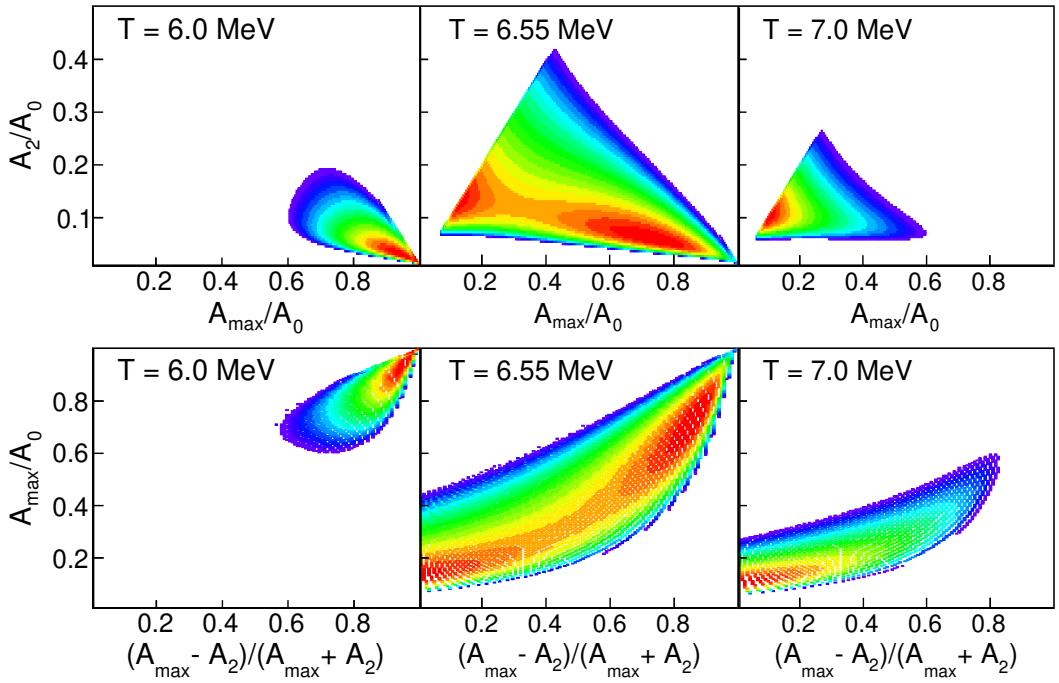

Figure 4.10: Probability distributions of the relation between the two largest fragment sizes below, at, and above the transition temperature for system of size $A_0 = 216$. The probabilities are indicated by a logarithmic color scale.

transition, indicating phase coexistence as in liquid-gas phase transitions.

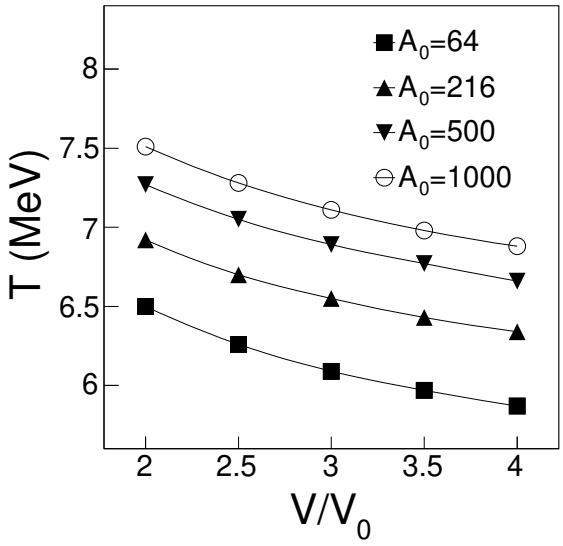

Figure 4.11: Transition temperature as a function of the freeze-out volume for indicated system sizes.

Presented above results are for the freeze-out volume $V = 3V_0$, three times larger than the normal nucleus volume. The calculations have also been performed for other freeze-out volumes to evaluate how the transition temperature depends on this model parameter.

Figures 4.11 and 4.12 show the obtained dependences for various system sizes. For all the systems, the transition temperature decreases by about 0.65 MeV with a freeze-out volume increase from $2V_0$ to $4V_0$. It might be also interesting to compare the shapes of the $P(A_{\max})$ distribution at the transition point for different freeze-out volumes. Figure 4.13 shows such a comparison for the system with 216 nucleons. The distributions are very similar - only a slight increase in the degree of bimodality is observed with increasing the freeze-out volume.

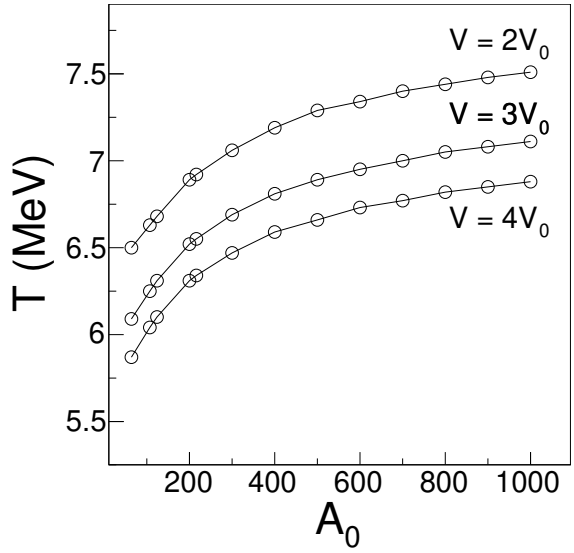

Figure 4.12: Transition temperature as a function of the system size for three freeze-out volumes.

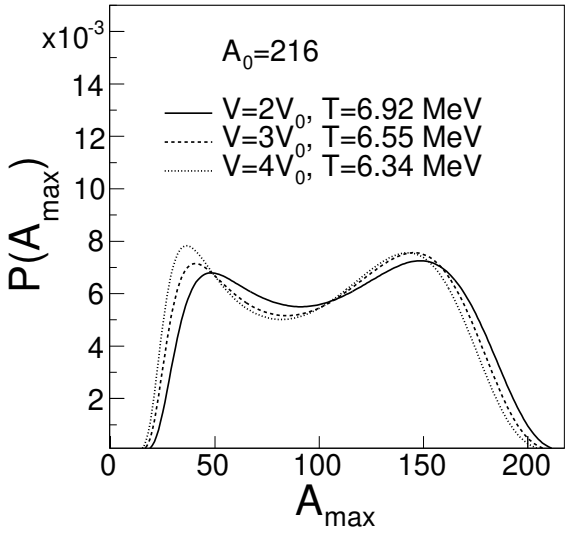

Figure 4.13: Largest fragment size distribution at the transition temperature for different freeze-out volumes.

4.2.2 Two-component Canonical Model

In the two-component CTM, the system consists of two kinds of particles: protons and neutrons. Clusters are specified by two indices i, j where i is the number of protons and j is the number of neutrons. The partition function for the fragmenting system with Z_0 protons and N_0 neutrons (mass number $A_0 = Z_0 + N_0$) at a temperature T is given as

$$Q_{\mathrm{Z_0,N_0}} = \sum \prod_{\mathrm{i,j}} \frac{\omega_{\mathrm{i,j}}^{n_{\mathrm{i,j}}}}{n_{\mathrm{i,j}}!} \tag{4.24}$$

where $\omega_{\mathrm{i,j}}$ is the partition function of one composite with i protons and j neutrons (mass number $a = i + j$), and $n_{\mathrm{i,j}}$ is the number of such composites in a given channel. The sum is over all possible break-up channels that satisfy the requirements

$$Z_0 = \sum_{\mathrm{i,j}} i \times n_{\mathrm{i,j}} \tag{4.25}$$

and

$$N_0 = \sum_{\mathrm{i,j}} j \times n_{\mathrm{i,j}} \tag{4.26}$$

The partition function of a fragment is

$$\omega_{\mathrm{i,j}} = \frac{V_{\mathrm{a}}}{h^3} (2\pi m_0 a T)^{3/2} \times z_{\mathrm{i,j}} \tag{4.27}$$

where $m_0 a$ is the fragment mass. The available volume V_{a} is calculated as in the one-component model. Here, the intrinsic partition function $z_{i,j}$ is specified as

- For protons and neutrons: $z_{1,0} = z_{0,1} = 2$ to incorporate the spin degeneracy.
- For deuteron, triton, ^{3}He and ^{4}He

  $$z_{\mathrm{i,j}} = (2s_{\mathrm{i,j}} + 1) \exp\left(\frac{-E_{\mathrm{i,j}}(gr)}{T}\right) \tag{4.28}$$

  where $s_{\mathrm{i,j}}$ and $E_{\mathrm{i,j}}(gr)$ are the experimental ground-state spin and energy, respectively:
  $s_{1,1,} = 1 \quad E_{1,1}(gr) = -2.225$ MeV (deuteron)
  $s_{1,2} = \frac{1}{2} \quad E_{1,2}(gr) = -8.482$ MeV (triton)
  $s_{2,1} = \frac{1}{2} \quad E_{2,1}(gr) = -7.718$ MeV (^{3}He)
  $s_{2,2} = 0 \quad E_{2,2}(gr) = -28.296$ MeV (^{4}He),
  Excited states of these light nuclei are not included.
- For fragments with mass number $a \geq 5$ the internal partition function is calculated using the liquid-drop model for binding energies and the Fermi-gas model for excited states

  $$z_{\mathrm{i,j}} = \exp\frac{1}{T}\left[W_0 a - \sigma(T) a^{2/3} - \kappa \frac{i^2}{a^{1/3}}(1-w) - s\frac{(i-j)^2}{a} + \frac{T^2 a}{\varepsilon_0}\right] \tag{4.29}$$

With respect to the one-component CTM, the formula includes two additional terms: the Coulomb energy term with the coefficient $\kappa = 0.72$ MeV and the parameter w correcting for the Coulomb interaction between different composites, which is calculated based on the Wigner-Seitz approximation $w = 1 - (V_0/V)^{1/3}$ [26], and the symmetry energy term with the coefficient $s = 23.2$ MeV. One needs to specify which composites are included in the partition function. Here, for mass number $a = 5$ only charge numbers i = 2, 3 and for mass number a = 6 only charge numbers i = 2, 3, 4 are taken into account. For $a > 6$ all nuclei were included within drip lines derived from the liquid-drop formula.

The probability of a given channel is

$$P(\vec{n}_{\mathrm{i,j}}) = P(n_{0,1}, n_{1,0}, n_{1,1}, ..., n_{i,j}, ...) = \frac{1}{Q_{\mathrm{Z_0,N_0}}} \prod_{i,j} \frac{(\omega_{\mathrm{i,j}})^{n_{\mathrm{i,j}}}}{n_{\mathrm{i,j}}!} \tag{4.30}$$

The average number of composites with i protons and j neutrons can be calculate as

$$\langle n_{\mathrm{i,j}} \rangle = \frac{Q_{\mathrm{Z_0-i,N_0-j}}}{Q_{\mathrm{Z_0,N_0}}} \omega_{\mathrm{i,j}} \tag{4.31}$$

From this and the constraint of Eq. 4.25 one obtains a recursion relation to compute partition functions

$$Q_{\mathrm{Z_0,N_0}} = \frac{1}{Z_0} \sum_{\mathrm{i,j}} i \omega_{\mathrm{i,j}} Q_{\mathrm{Z_0-i,N_0-j}} \tag{4.32}$$

Deriving formula for the probability $P(A_{max})$ follows in a similar way as in the one-component model. We construct $Q_{\mathrm{Z_0,N_0}}(a)$ where all the intrinsic partition functions $\omega_{\mathrm{i,j}}$ are set to zero when $i + j > a$. The probability that the largest fragment mass number is A_{max} can be calculated as

$$P(A_{\mathrm{max}} = a) = \frac{Q_{\mathrm{Z_0,N_0}}(a) - Q_{\mathrm{Z_0,N_0}}(a-1)}{Q_{\mathrm{Z_0,N_0}}} \tag{4.33}$$

The calculation of the probability $P(Z_{\mathrm{max}})$ that the largest fragment charge number is Z_{max} can be done by analogy with appropriate changes in the formula.

Due to long-range Coulomb interactions the model generates some fraction of fission-like channels containing two large fragments [96]. Such fission events are usually removed from the analysis of fragment size distributions in phase transition (criticality) studies (see e.g. [5,97]). Their presence would otherwise contaminate the obtained results. In the present calculations the contribution from fission-like events was suppressed to focus on possible signatures of a phase transition. The obtained results concerning the temperature dependence of the heat capacity and the largest fragment size distribution are shown in Figs. 4.14 - 4.16 for several nuclear systems. Qualitatively, these results are similar to those of the one-component model. However, as a consequence of the Coulomb repulsion, the maxima of the specific heat C_{V} are positioned at lower temperatures around 5.5 MeV, nearly independently of the system size. Comparing Fig. 4.15 with Fig. 4.16 shows that

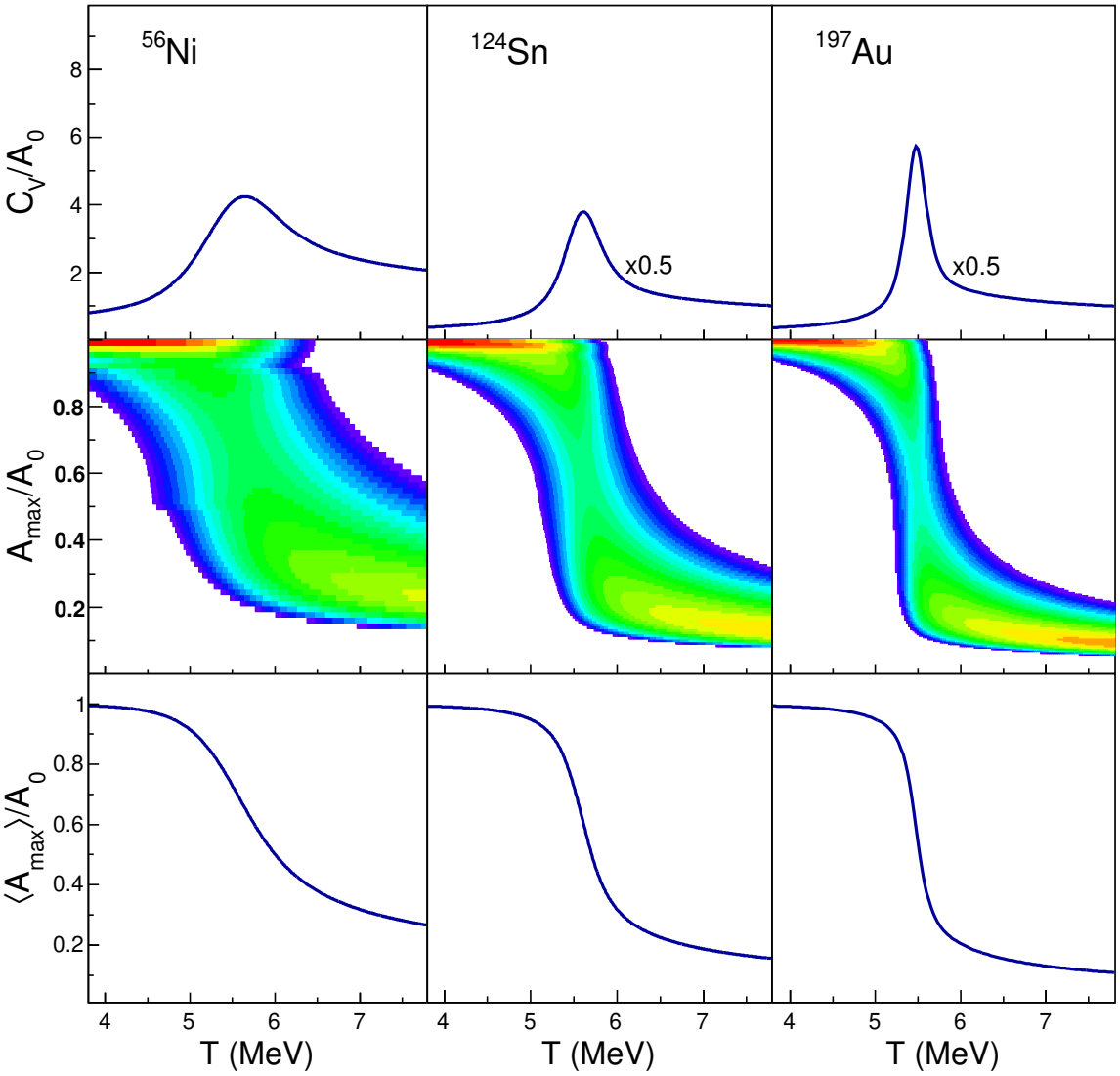

Figure 4.14: The specific heat C_V (top panel), the distribution of the largest fragment mass number A_{max} (middle panel), and the mean value $\langle A_{max} \rangle$ of the largest fragment mass normalized with respect to the system mass A_0 (bottom panel) as a function of the temperature for the indicated nuclear systems.

the cumulant ratios K_i are almost identical for the A_{max} and Z_{max} distributions. Defining the transition temperature through the maximum of C_V, referred also to as the boiling or breakup point [17], we observe that it coincides with the zero crossing of the skewness K_3 and the minimum of K_4. This corroborates conclusions from the percolation and one-component CTM studies that such characteristics of K_3 and K_4 can indicate a trace of a phase transition in small systems. As can be seen from Figs. 4.15 and 4.16, the effect of varying the neutron content of the Sn isotopes is small. The weak effect of the system A_0/Z_0 ratio on the transition point can also be seen in Fig. 4.17, which plots the system size dependence of the breakup temperature for neutron-poor and neutron-rich

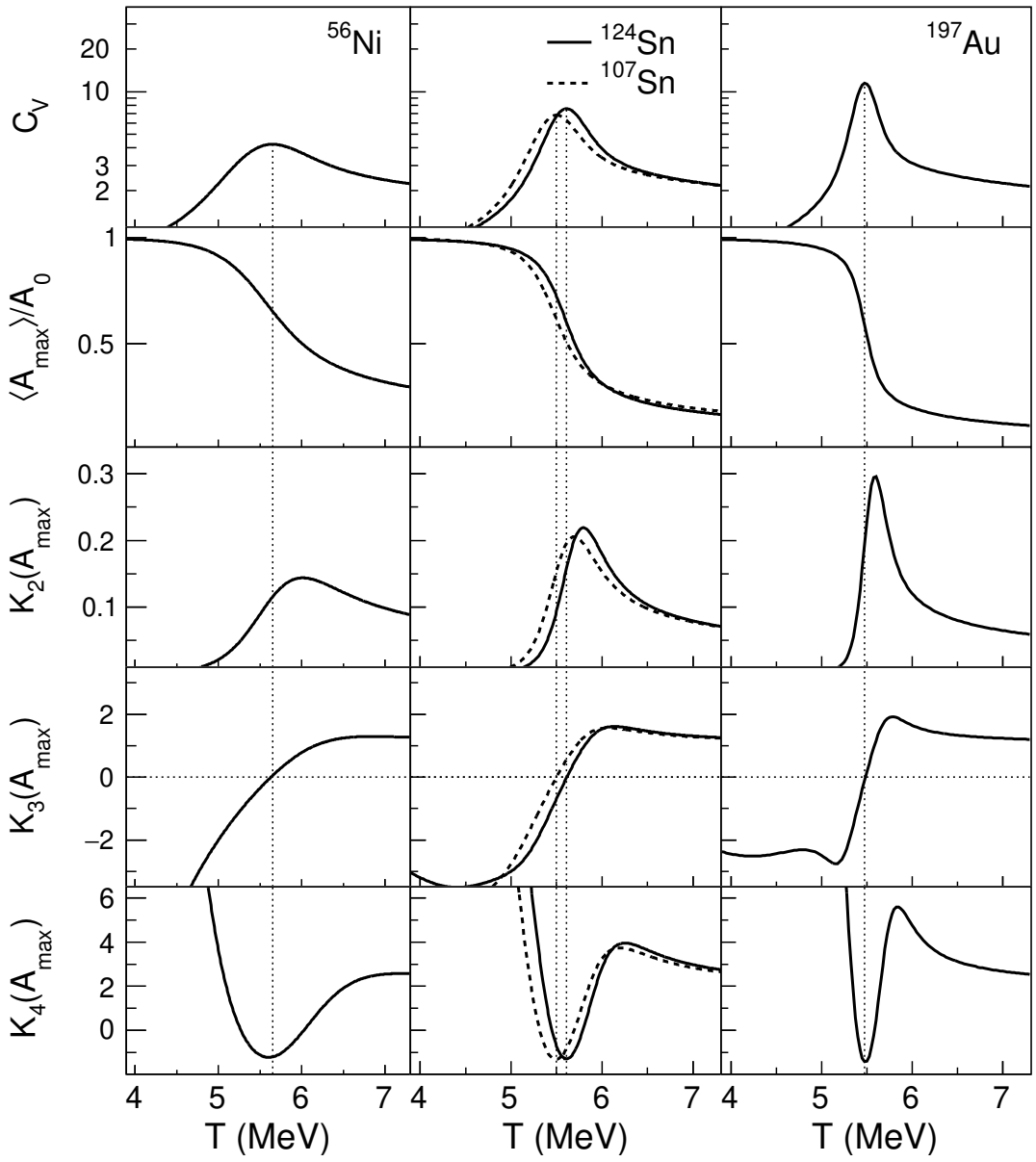

Figure 4.15: The specific heat C_V, the normalized mean value of the largest fragment mass, and the cumulant ratios K_2 to K_4 of the distributions of the largest fragment mass A_{max}, from top to bottom, as a function of the temperature for the indicated systems. The vertical dotted lines indicate the maxima of the specific heat coinciding with the zero transitions of K_3 and the minima of K_4.

systems. The results are shown for the three different freeze-out volumes V indicated in the figure. For given A_0/Z_0 and V, the transition temperature slightly decreases with increasing system size.

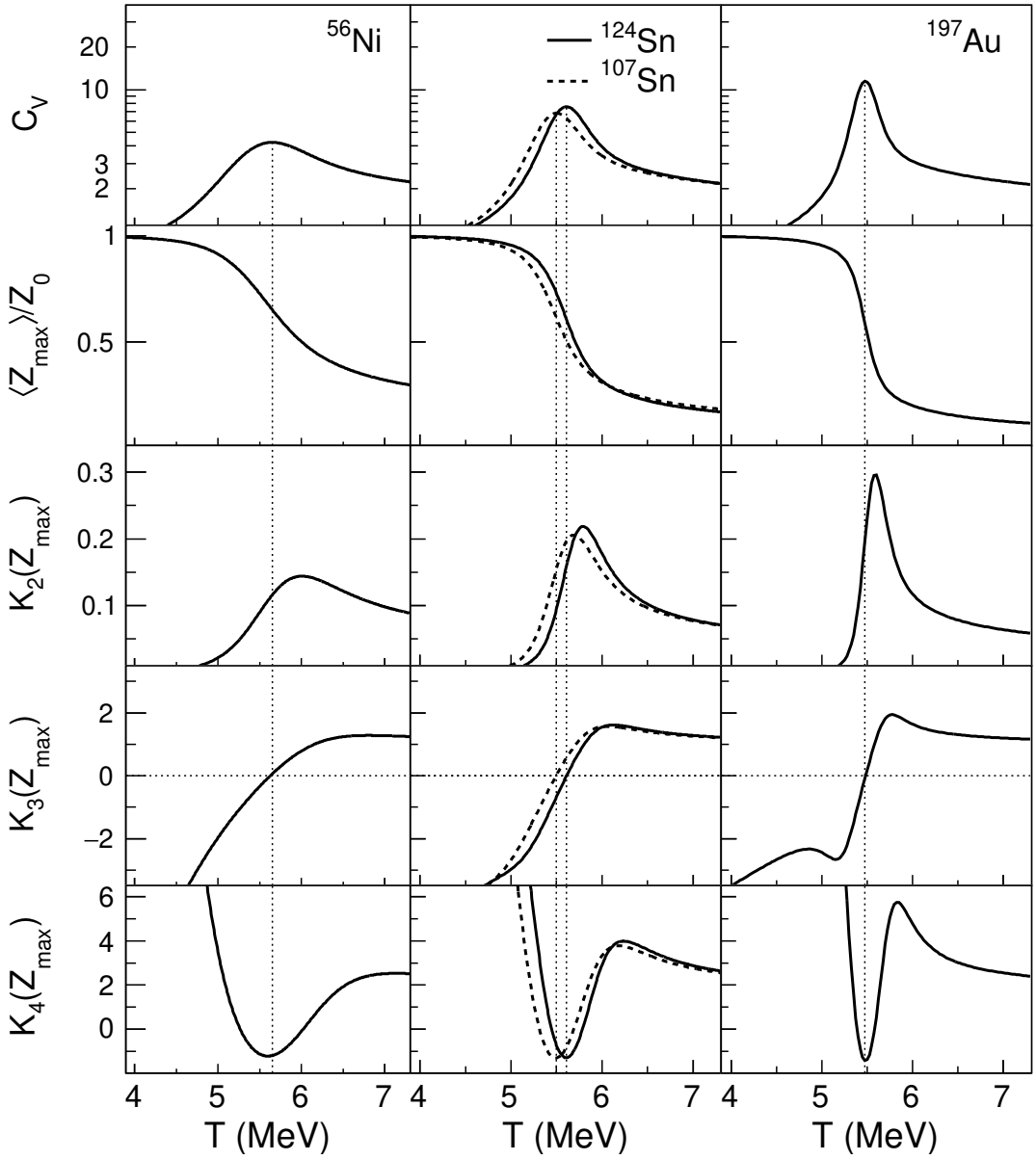

Figure 4.16: As in Fig. 4.15, but for the probability distribution of the largest fragment atomic number (charge) Z_{max}.

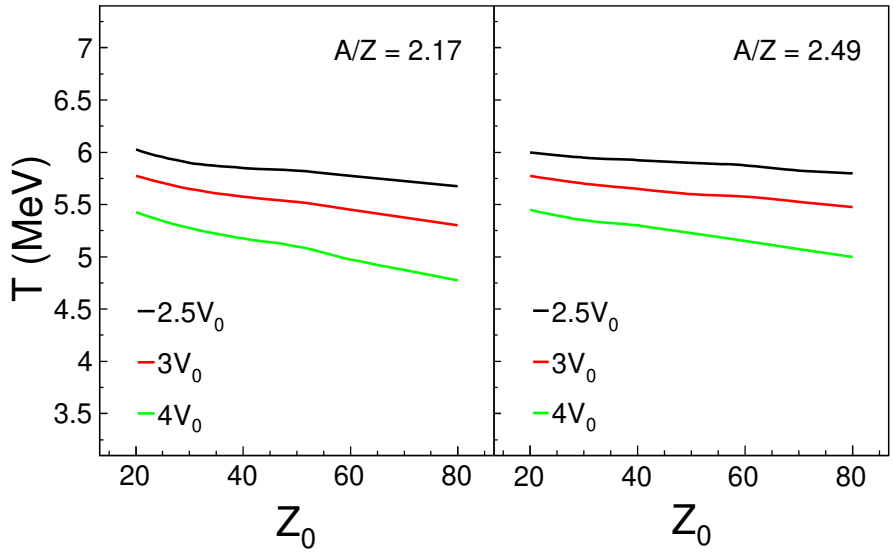

Figure 4.17: Transition (breakup) temperatures T_b as a function of the system charge Z_0 for neutron-poor (left) and neutron-rich (right) systems calculated for the three indicated freeze-out volumes.

4.3 Simulations with Statistical Multifragmentation Model

For more realistic simulations that can be compared with experimental data, we have used the Copenhagen Statistical Multifragmentation Model (SMM) [26], which includes secondary decays of hot primary fragments. The model input requires the specification of the atomic and mass numbers of the system (Z_0,A_0), the excitation energy, and the freeze-out density. The fragment characteristics are calculated as in the two-component CTM. The break-up channels are selected randomly from the ensemble of all possible partitions and their statistical weights (probabilities) are determined. For small fragment multiplicities, appearing at low excitation energies, the microcanonical sampling is performed. At high excitation energies, above 4 MeV/nucleon, the SMM code generates partitions by Monte-Carlo sampling from the grand-canonical distribution, however, with requiring the exact mass number and charge conservations in each partition. The temperature of the system in a given channel is determined iteratively so that the total energy is conserved. Therefore, it is referred to as the microcanonical temperature of the system. The hot primary fragments formed in the freeze-out volume are then propagated independently in their mutual Coulomb fields and undergo secondary decays. The decays of large fragments ($A > 16$) are simulated with the evaporation-fission model while smaller fragments with the Fermi break-up model [98].

Since the calculated events contain the complete information about all produced particles and fragments (masses, charges, and momenta), they can be treated in the same way as experimental events. In particular, they can be sorted into event groups according to measurable quantities. Of interest here is sorting events by Z_{bound}, defined as the sum of the atomic numbers Z of all fragments with $Z \geq 2$, which has been used in analyses of the ALADIN data on fragmentation of projectile spectators in peripheral collisions at relativistic energies [27–29, 99]. This quantity is correlated with the excitation energy per nucleon and plays the role of the control parameter.

In order to check whether the investigated phase transition signatures associated with the Z_{max} distributions are preserved for the Z_{bound} sorting, we have performed SMM simulations for the Sn system with $Z_0 = 50$ and $A_0 = 124$. A uniform excitation energy distribution extending to 10 MeV per nucleon, and the freeze-out density of one third of the normal nuclear density were assumed. Figure 4.18 presents the obtained results, showing in the left diagrams the Z_{max} distribution, its mean value, (normalized) variance and K_3, K_4 values as a function of Z_{bound}. The Z_{max} versus Z_{bound} plot shows that the break-up transition associated with the broadest Z_{max} distribution is located near $Z_{\mathrm{bound}} = 45$, as marked by the vertical dotted line. This distribution exhibiting a bimodal structure is shown in the right top diagram. As can be seen, the transition point on the Z_{bound} axis is well indicated by $K_3 = 0$ and a minimum of K_4. The systems at $Z_{\mathrm{bound}} = 45$ have the average excitation energy of 5.2 MeV/nucleon and the average temperature of 6 MeV. As shown in the right bottom diagram, this corresponds to a point laying on the flattest part of the caloric curve, confirming that the observed transition can be interpreted as a trace of a first-order phase transition.

These results support the usefulness of the zero crossing of K_3 and the minimum of K_4 as a signature of a phase transition in fragmenting nuclear systems (with the presence of secondary decays) with using measurable quantities such as Z_{max} and Z_{bound}.

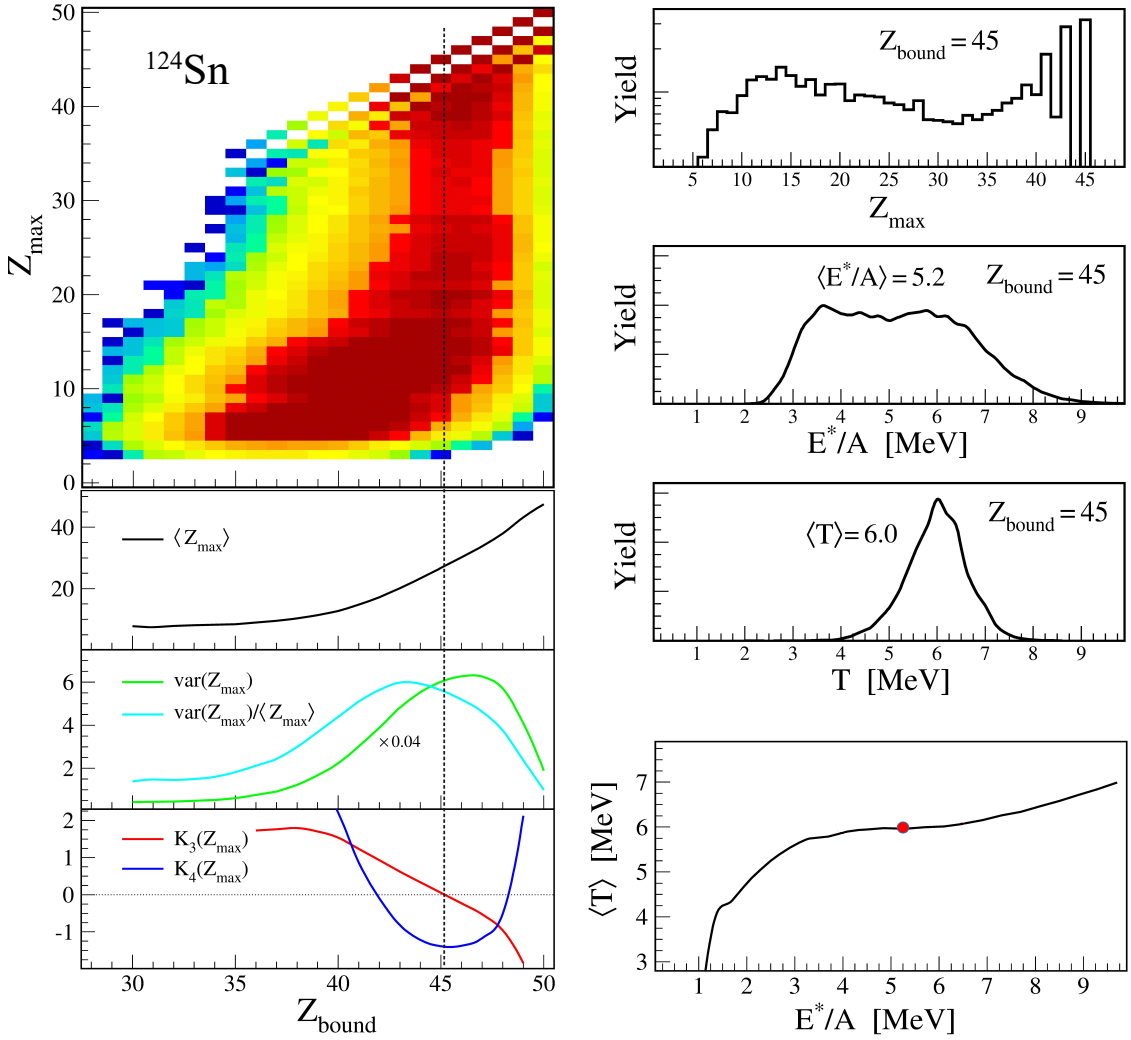

Figure 4.18: Results of SMM calculations for the ^{124}Sn system, performed over a wide range of the excitation energy. The left part shows the largest fragment charge distribution $P(Z_{\mathrm{max}})$ and its statistical measures as a function of Z_{bound}. The right part, from top to bottom: the distributions of Z_{max}, the excitation energy per nucleon and the temperature at the transition point $Z_{\mathrm{bound}} = 45$, and the caloric curve with a point indicating the mean excitation energy and temperature for $Z_{\mathrm{bound}} = 45$.

Chapter 5

ALADIN data on spectator fragmentation and percolation description

5.1 Experimental data

The present work examines the ALADIN data on fragmentation of projectile spectators in ^{197}Au + Cu, In, Au peripheral collisions at the incident energies of 600A MeV (Cu, In, Au targets), 800A MeV (Au), and 1000A MeV (Cu, Au). The experiment (S114) was performed at the heavy-ion synchrotron SIS of the GSI Helmholtzzentrum in Darmstadt.

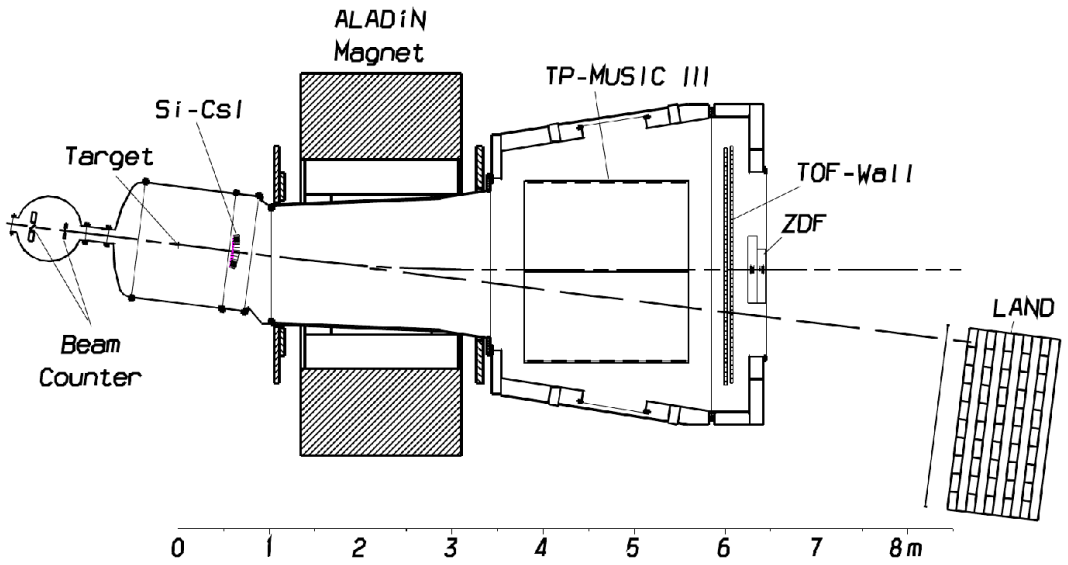

Figure 5.1: Schematic view of the ALADIN facility at GSI Darmstadt.

Details of the experiment and general characteristics of the data have been presented in Ref. [27]. Figure 5.1 shows the ALADIN experimental setup. Projectile fragments entering into the acceptance of the magnet were tracked and identified with the large volume time projection chamber TP-MUSIC III and the time-of-flight (TOF) wall. Fragments with the atomic numbers $Z \geq 2$ were detected with high efficiencies, close to

100% at the bombarding energy of 1000 MeV/nucleon, and fully Z-identified. For the present analysis, the event-sorted data files were used that formed the basis of the results reported in the experimental paper [27]. A prominent feature of the ALADIN data is that

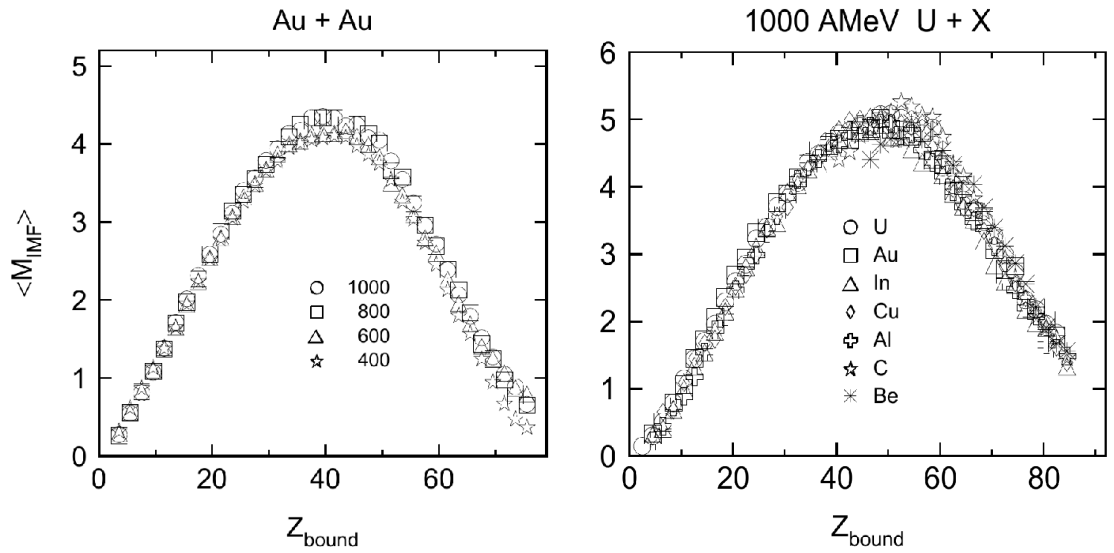

Figure 5.2: The mean multiplicity of intermediate-mass fragments (with atomic numbers $3 \leq Z \leq 30$) as a function of Z_{bound} for the reaction ^{197}Au + ^{197}Au at the incident energies of 400, 600, 800 and 1000 MeV/nucleon (left), and for the reactions of ^{238}U projectiles at the energy of 1000 MeV/nucleon with the seven targets of Be, C, Al, Cu, In, Au and U (right). Figures from Ref. [27].

the fragment multiplicities and correlations are independent of the projectile energy and the target nucleus when plotted as a function of Z_{bound} (the sum of the atomic numbers Z of all fragments with $Z \geq 2$). For example, the left part of Fig. 5.2 shows that the mean multiplicity of intermediate-mass fragments (IMF's) is independent of the projectile energy within the experimental accuracy for the ^{197}Au + ^{197}Au reactions. The invariance with respect to the target is shown in the right part of the figure for the case of ^{238}U projectiles at the incident energy of 1000 MeV/nucleon. This universality has been interpreted as indicating a high degree of equilibration attained prior to or during the fragmentation stage [27]. The numbers of events as a function of Z_{bound} in the analysed ALADIN data sets are presented in Fig. 5.3. The largest statistics were obtained with the Au target.

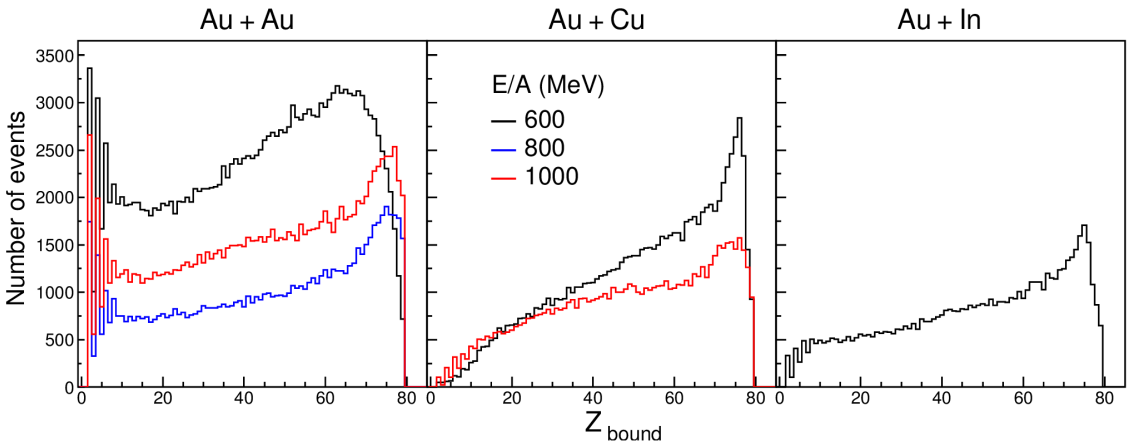

Figure 5.3: Distributions of Z_{bound} in the ALADIN data.

5.2 Largest fragment charge distributions

Examples of the the largest fragment charge Z_{max} distributions at several Z_{bound} values are shown in Fig. 5.4 for the reaction Au + Au at 600 MeV/nucleon. The event sorting variable Z_{bound} is correlated with the size of the projectile spectator and inversely correlated with the excitation energy per nucleon [99]. At low excitation energies, corresponding to largest Z_{bound} values, evaporation processes are dominant, leaving one large fragment (heavy remnant). At excitation energies approaching and exceeding the nuclear binding energy, the systems are disassembled into many small fragments. The transition between the two extreme regimes is characterized by a rapidly decreasing Z_{max} associated with an increasing number of fragments. The evolution of the Z_{max} distribution seen in Fig. 5.4 indicates that such a transition takes place between $Z_{\mathrm{bound}} = 50$ and $Z_{\mathrm{bound}} = 60$, where also a fast rising of the IMF production is observed (see Fig. 5.2). This transition is clearly visible in Fig. 5.5 presenting the correlation between Z_{max} and Z_{bound}. The plot reveals also a small fraction of fission events with Z_{max} around 40 located at largest Z_{bound} values.

In order to identify the breakup transition and to find its precise location, the cumulant ratios K_i of the the Z_{max} probability distributions have been examined. They are shown in Fig. 5.6, plotted as a function of Z_{bound} for different targets and energies. The comparison of the different data sets confirms that also these distributions are independent of the projectile energy and the target nucleus. Significant systematic differences are seen only for K_2 below $Z_{\mathrm{bound}} \simeq 50$. The values of K_2 in the region of small Z_{bound} depend slightly on the projectile energy. It may be related to a sensitivity of K_2 to existing small changes in the reaction dynamics or perhaps simply to a residual energy dependence of the detection efficiency. At large excitation energies corresponding to small Z_{bound} values, secondary evaporation effects may also be of importance. The signature characteristic of a phase transition $K_3 = 0$ and minimum of K_4 is clearly observed at $Z_{\mathrm{bound}} = 54$ in all the cases. The statistical errors are small and comparable to the apparent scatter of the data points. They are smallest near the transition point $Z_{\mathrm{bound}} = 54$, where the error bars are smaller than the size of data symbols. The errors become larger for smaller Z_{bound} values. For example, at $Z_{\mathrm{bound}} = 31$, the error analysis for the Au + Au system at 1000 MeV/nucleon yields 0.0091, 0.077, and 0.347 for the statistical rms uncertainties of K_2, K_3, and K_4,

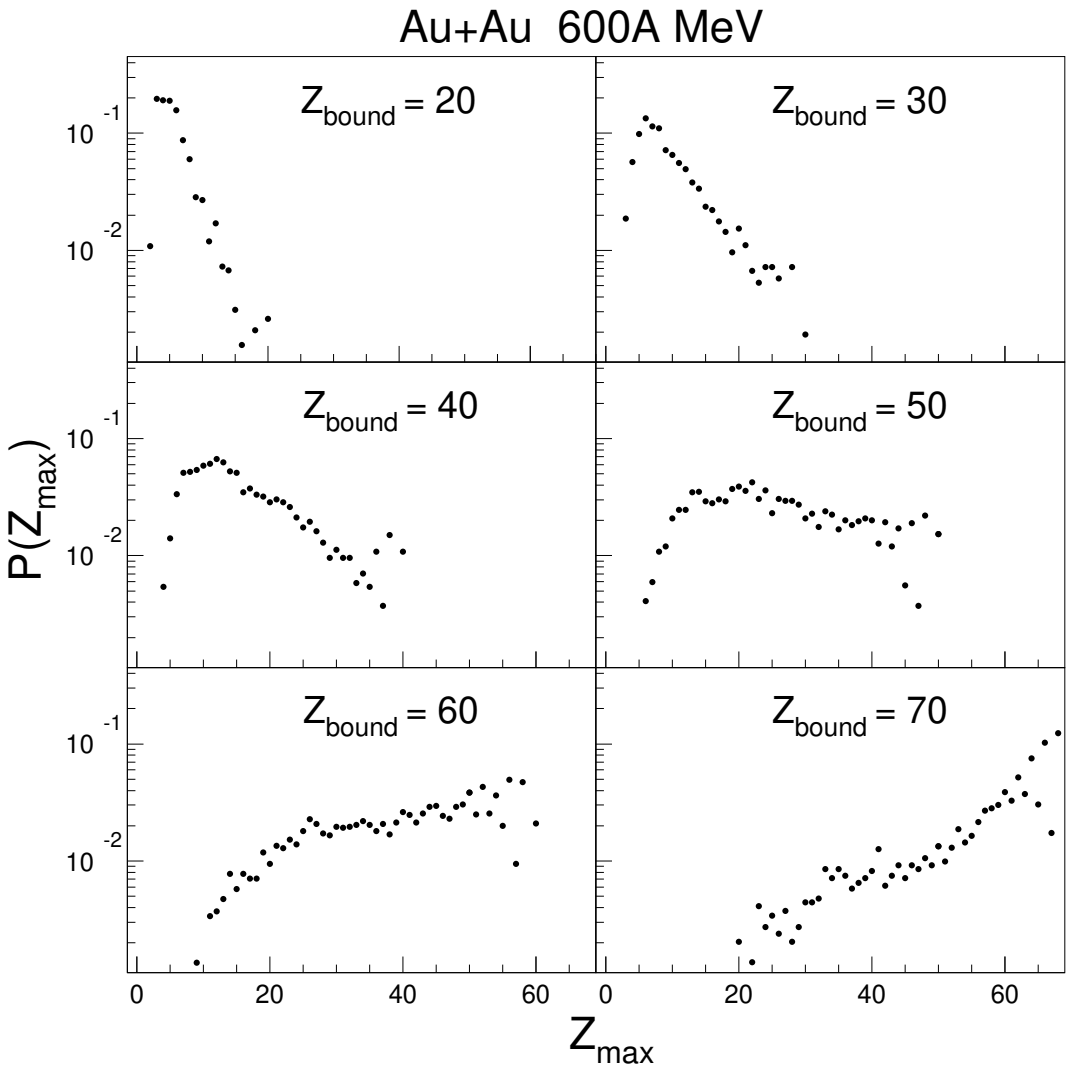

Figure 5.4: Probability distributions of the largest fragment charge at several Z_{bound} values in Au + Au collisions at 600 MeV/nucleon.

respectively. For clarity, these errors are not displayed in the figure.

In the following, the experimental results will be compared with predictions of the cubic bond percolation model. The atomic number serves as a measure of the fragment size in the experimental data. The corresponding measure in the percolation analysis performed here is the number of sites contained within a cluster. In other words, the number of sites is considered as the number of protons. The same notation will be used for percolation quantities as for their experimental counterparts. Percolation events were generated with Monte Carlo simulations for the bond probabilities uniformly distributed in the interval $[0,1]$, and then sorted according to Z_{bound}. The experimental and simulated cumulant ratios K_i of the largest fragment size distribution $P(Z_{\mathrm{max}})$ are compared in Fig. 5.7. The percolation results are plotted in the left part as a function of Z_{bound} normalized to the system size Z_0, for three different system sizes that span over a range expected to be in the transition region. In this representation, the K_{i} distributions show a weak dependence on the system size which vanishes at the pseudocritical point located

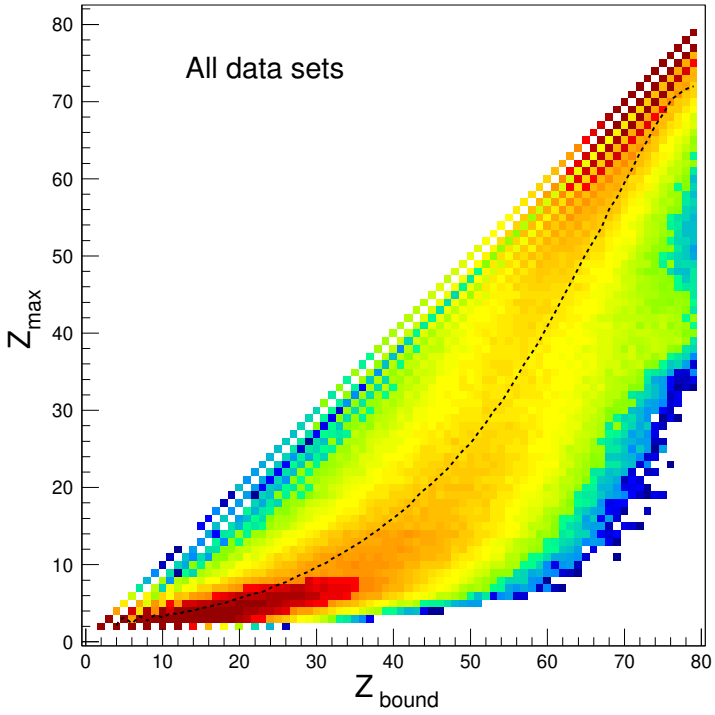

Figure 5.5: Distribution of Z_{max} vs Z_{bound} for the ALADIN data shown with a logarithmic color scale. The broken line indicates the mean values of Z_{max}.

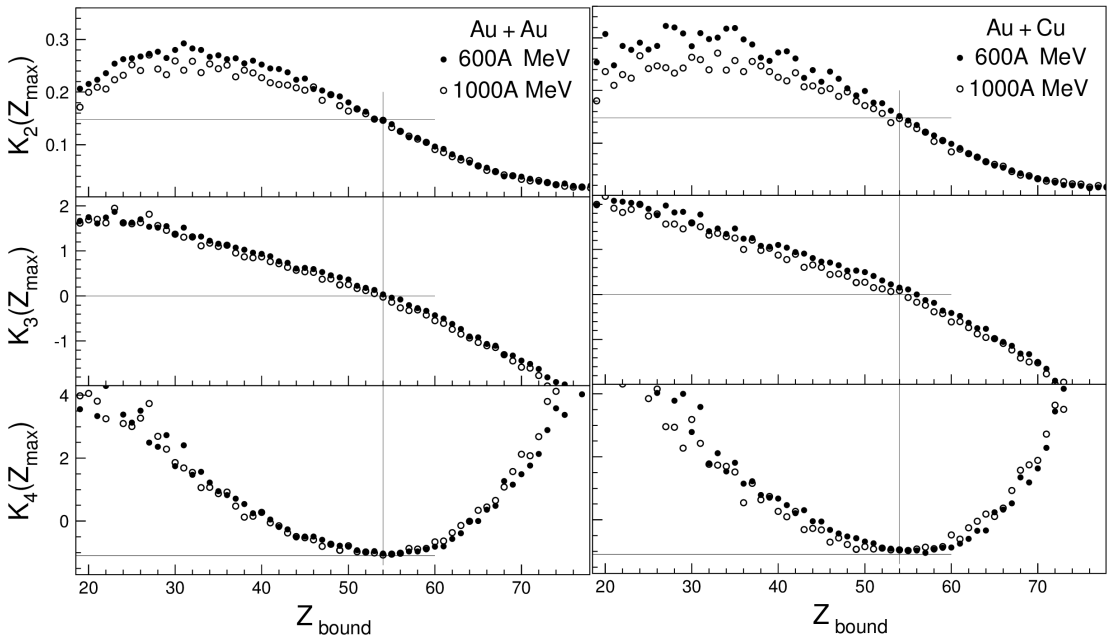

Figure 5.6: The cumulant ratios of $P(Z_{\mathrm{max}})$ as a function of Z_{bound}. Experimental data for Au fragmentation following collisions with Au targets (left panels) and Cu targets (right panels) at the incident energies of 600 and 1000 MeV/nucleon. The statistical errors are of the order of the scatter of the data symbols.

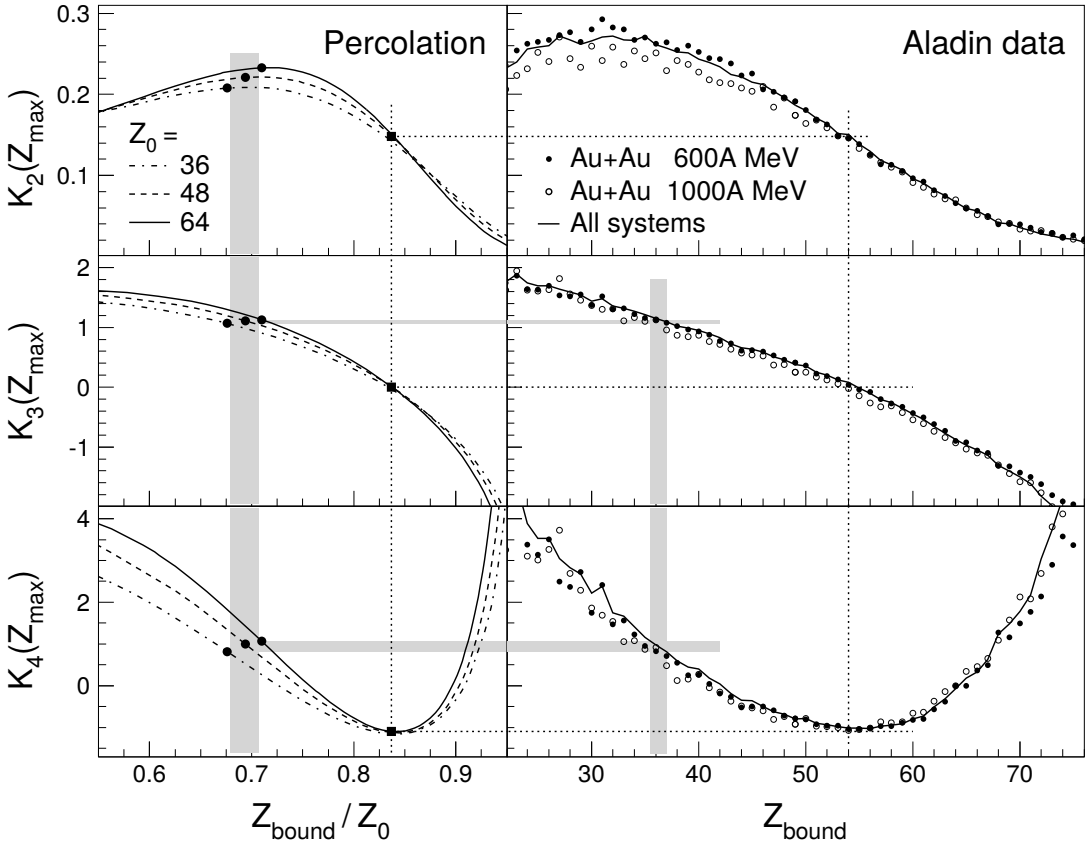

Figure 5.7: The cumulants of $P(Z_{\max})$ as a function of Z_{bound} (or Z_{bound} normalized with respect to Z_0 in the case of percolation). The results of bond percolation calculations for three values of Z_0 (left panels) are shown in comparison with the experimental data for ^{197}Au fragmentation (right panels) following collisions with ^{197}Au targets at two energies (symbols) and the combined results for all systems (full lines). The meaning of the lines and of the symbols in the left panels is explained in the text. Figure published in [30].

at $Z_{\text{bound}}/Z_0 \simeq 0.84$ (the squares). The results corresponding to the true critical point are located near the maximum of K_2 (Fig. 5.7) but their positions on the Z_{bound}/Z_0 axis depend somewhat on the system size (the filled circles in Fig. 5.7, left panel).

The experimental results are shown in the right diagrams for the ^{197}Au + ^{197}Au systems at 600 and 1000 MeV/nucleon and for the summed data sets (all targets and all energies). Here, the cumulant ratios K_{i} are plotted as a function of Z_{bound}. The system sizes are considered unknown quantities that are to be determined. Overall, the percolation and experimental patterns of K_{i} are very similar. The specific characteristics of the percolation pseudocritical point are well observed in the data at $Z_{\text{bound}} \simeq 54$. With this correspondence, the mean system size at $Z_{\text{bound}} \simeq 54$ may be estimated as $Z_0 \simeq Z_{\text{bound}}/0.84 \simeq 64$. For the percolation "critical" point, an approximate correspondence can be established relying on K_3 and K_4. It indicates $Z_{\text{bound}} \simeq 36$ and a system size Z_0 around $36/0.69 \simeq 52$.

In order to test the sensitivity of K_i to the secondary decay and detection inefficiency effects, a simple simulation was performed and applied to percolation events. The result is shown in Fig. 5.8. The largest cluster was divided into two fragments:

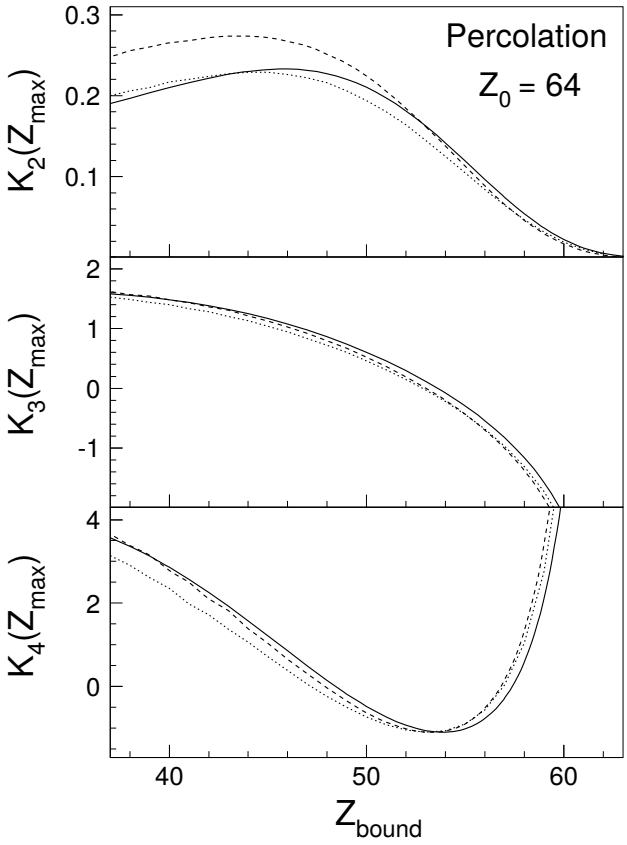

Figure 5.8: The cumulants of $P(Z_{\mathrm{max}})$ as a function of Z_{bound} calculated for the system size $Z_0 = 64$ as shown in the left panel of Fig. 5.7 (full lines) in comparison with the results of the two tests described in the text investigating the effects of secondary decays (dashed lines) and of the detection efficiency of the spectrometer (dotted lines). Figure published in [30].

$Z_{\mathrm{max}} \rightarrow (Z_{\mathrm{max}} - 1) + 1$ with probability p_1, or $Z_{max} \rightarrow (Z_{\mathrm{max}} - 2) + 2$ with probability p_2. Such calculations with various assumptions on p_1 and p_2 indicate that K_2 significantly increases at small Z_{bound} while K_3 and K_4 remain nearly unchanged. As an example, for $Z_0 = 64$ with $p_1 = 0.6$ and $p_2 = 0.3$, the maximum of K_2 increases from 0.23 to 0.27 and its position is shifted towards lower Z_{bound} by $\sim 5\%$ (Fig. 5.8, dashed lines). These observations support the conclusion that K_3 and K_4 are more reliable than K_2 as quantitative indicators of the transition points. The results of a test investigating the effects of the small detection inefficiencies of the spectrometer are shown in the same panels of Fig. 5.8 (dotted lines). It consisted of modifying the percolation event files by randomly deleting fragments with probabilities $1 - \varepsilon(Z)$ and redoing the cumulant analysis with these modified files. The detection efficiencies $\varepsilon(Z)$ were assumed to have the values of the geometrical acceptance of the time-of-flight wall of the spectrometer as determined for 800 MeV/nucleon incident energy [100]. They increase smoothly from $\varepsilon(2) = 0.93$ to $\varepsilon(7) = 0.99$ and $\varepsilon(Z) = 1.00$ for $Z \geq 8$. This test cannot restore the original event structure nor can it take account of additional sources of uncertainties mentioned in the experimental reports [27, 100] as, e.g., reactions in the detector material. However, these processes are estimated to cause similarly small effects on the

percent level whose magnitude can equally be estimated from the deviation of the test result. Both tests indicate that the modifications can be expected to be small, corresponding to an uncertainty of the order of one unit of Z_{bound} on the abscissa. The coincidence of the zero crossing of K_3 with the minimum of K_4 is not affected.

5.3 Sizes of fragmenting systems

Information on the size of the fragmenting system (spectator remnant) is necessary for performing theoretical calculations. Only the knowledge of the relation between Z_{bound} and Z_0 is required. An estimation of the mean system mass $\langle A_0 \rangle$ as a function of Z_{bound} in several Z_{max} windows was made for the 600A MeV ^{197}Au + Cu reaction [101]. Assuming the charge-to-mass ratio $Z_0/A_0 = 0.4$ as for ^{197}Au projectiles, the results converted to the mean system charge $\langle Z_0 \rangle$ and averaged over Z_{max} bins are shown in Fig. 5.9 by the solid line. A similar result (dashed line) was obtained by Campi *et al.* who used a sum-rule approach for extrapolating from the measured Z_{bound} to Z_0 [102]. As it was

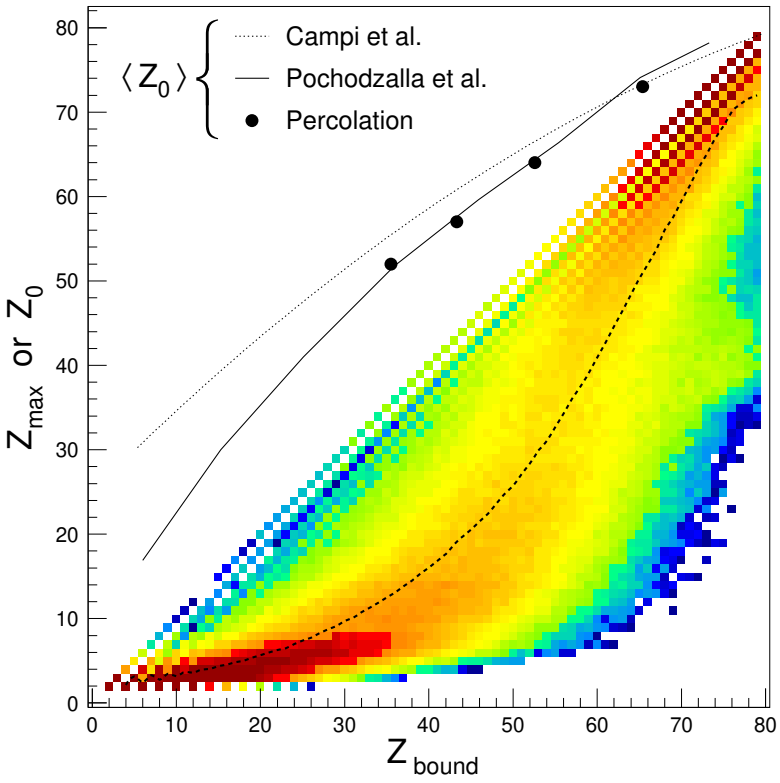

Figure 5.9: Estimates of the mean system size $\langle Z_0 \rangle$ as a function of Z_{bound}, plotted with the Z_{max} experimental distributions shown in Fig. 5.5. The full and thin dashed lines represent two estimates of $\langle Z_0 \rangle$ obtained from the experimental data with different methods [101, 102] while the filled circles give the result obtained with present percolation analysis (see text). Figure published in [30].

shown above for the critical and pseudocritical points, the system sizes can be deduced from comparisons between the experimental data and the percolation predictions using

K_i versus Z_{bound} dependencies. Such a procedure based on the K_3 and K_4 equalities can be extended to other Z_{bound} values. In Fig. 5.10 the cumulants are plotted as a function of Z_{bound} for the experimental data and percolation systems of different sizes Z_0. For a given Z_0, the crossing of the percolation and experimental lines determine the corresponding Z_{bound}. The relation found by this procedure is displayed in Fig. 5.9 by the solid circles. As can be seen, it is in very good agreement with the experimental estimates of Ref. [101]. In reality, the system sizes at fixed Z_{bound} are dispersed. To evaluate the significance of this dispersion for the analysis, additional percolation calculations have been performed for a Gaussian distribution of Z_0 with the mean of 57 and standard deviation of 2. Such a deviation is suggested by SMM simulations with input conditions established in Ref. [103]. The results are plotted in Fig. 5.10 by the dashed lines, showing that the dispersion effects are not substantial.

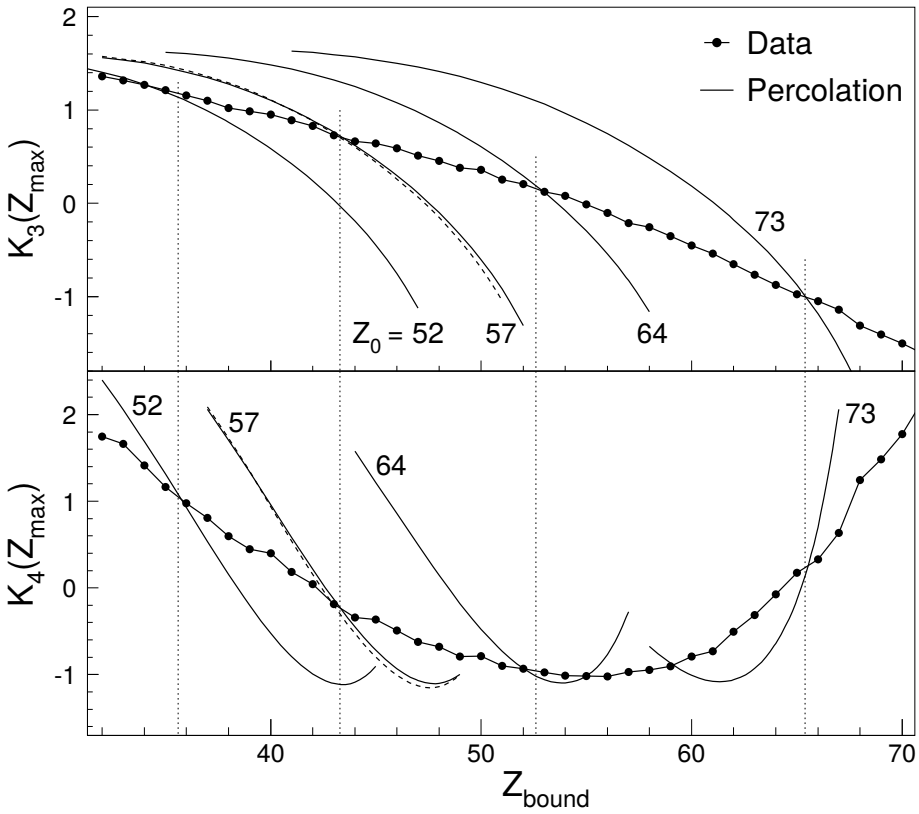

Figure 5.10: The K_3 and K_4 cumulants as a function of Z_{bound}. The experimental data (filled circles, all systems, as shown by full lines in Fig. 5.7, right panel) and percolation calculations for the indicated system sizes Z_0. The dotted vertical lines indicate the crossing points for K_3 and K_4. The dashed line shows the result obtained with a Gaussian distribution of Z_0 with $\langle Z_0 \rangle = 57$ (see text). Figure published in [30].

5.4 Fragment yields and correlations

This section examines if the close resemblance between the data and percolation observed for the Z_{max} distributions is more general, extending to the whole fragmentation pattern. It is also interesting whether the critical and pseudocritical points indicated by the K_3 and K_4 cumulants are coinciding with other criticality signals associated with fragment size distributions, such as the Fisher power-law and the Zipf's law.

5.4.1 Fisher power-law

A power-law fragment size (mass or charge) distribution was frequently observed in nuclear fragmentation and interpreted as a signature of critical behavior at liquid-gas phase transition, see e.g. [56, 57, 67, 80, 104, 105]. This interpretation was stimulated by the Fisher's droplet model, which predicts a power-law droplet-size distribution with the critical exponent τ between 2.1 and 2.3 for systems at the critical point [58]. In the

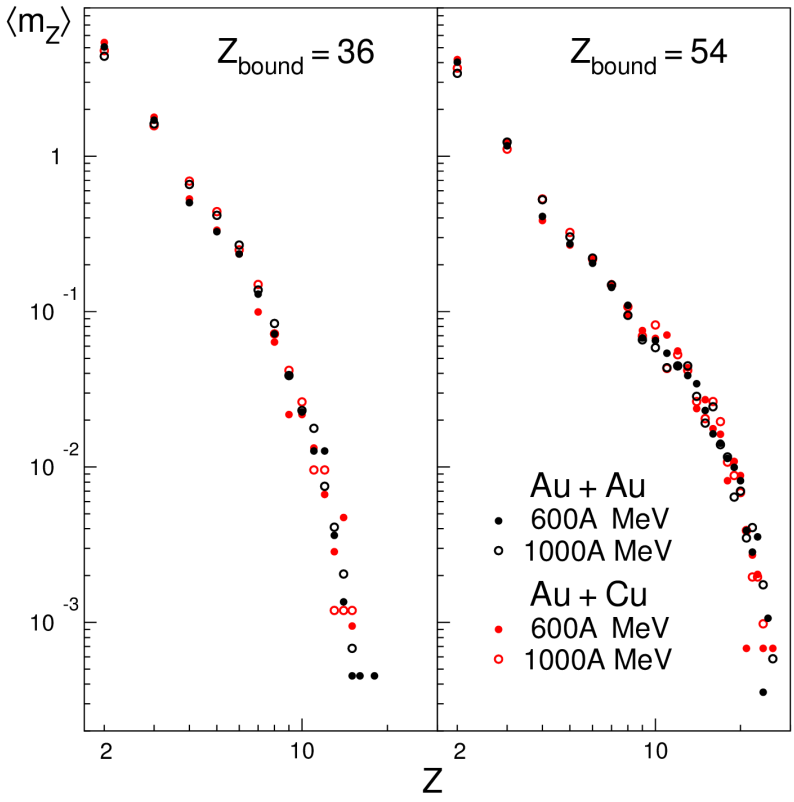

Figure 5.11: The experimental mean fragment multiplicity as a function of the fragment charge Z (the largest fragment excluded) for indicated systems, selected with the conditions $Z_{bound} = 36$ and 54.

percolation model, the cluster size distribution for infinite systems at the critical point also obeys a power-law with $\tau = 2.189$ [106]. In finite systems such a distribution is expected near the pseudocritical point, but only in a limited range of small clusters when the largest cluster is excluded [24]. Denoting the system size by Z_0 and the cluster (fragment) size

by Z, it can be described as

$$\langle m_Z \rangle = q_0 Z_0 Z^{-\tau} \tag{5.1}$$

where $\langle m_Z \rangle$ is the mean multiplicity of fragments with atomic number Z, and the normalization coefficient $q_0 = 0.173$ [24].

The experimental fragment charge distributions for two different targets and energies at $Z_{\text{bound}} = 36$ and 54 are shown in Fig. 5.11. Since all the data sets give approximately the same results, they can be summed to obtain better statistics for comparisons with percolation predictions as made in Fig. 5.12. The percolation calculations are performed for the estimated system sizes $Z_0 = 52$ and 64. As can be seen, the model well describes the data over four orders of magnitude. The dotted lines represent the power-law dependencies of Eq. 5.1 (straight lines in log-log plots). At $Z_{\text{bound}} = 54$, the distributions follows for $Z < 15$ this asymptotic power-law dependence with the exponent $\tau = 2.189$, as expected for the percolation pseudocritical point. I should be noted that this τ value is close to the Fisher critical exponent of the liquid-gas phase transition universality class, which is about 2.21 [107].

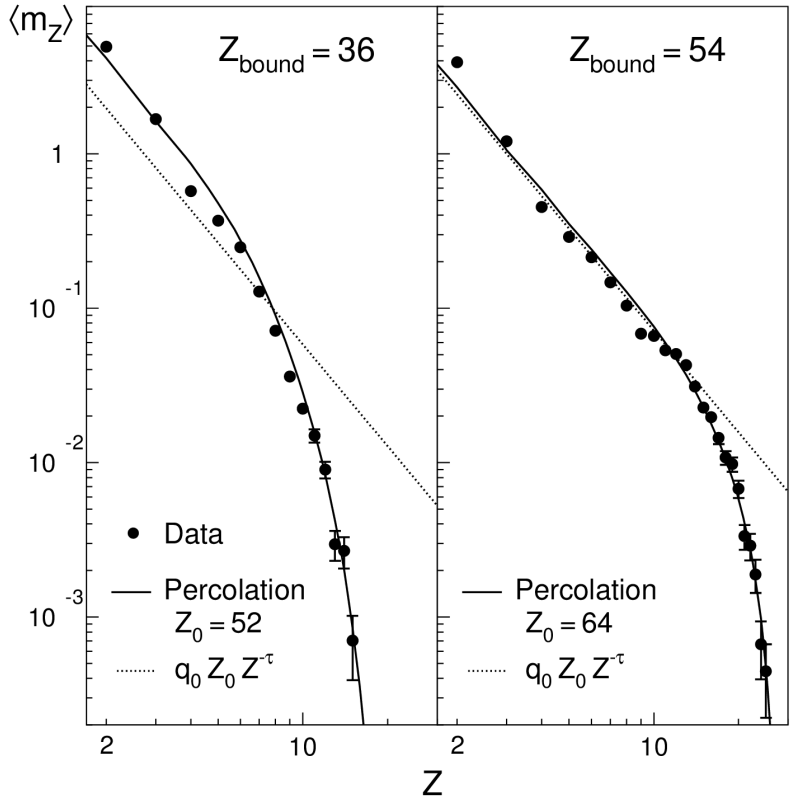

Figure 5.12: Fragment charge distributions for $Z_{\text{bound}} = 36$ and 54. Experimental data for all systems (filled circles) compared with percolation predictions (solid lines). The statistical error bars are shown for errors larger than the symbol size. The asymptotic power-law dependencies of Eq. 5.1 are plotted with dotted lines.

5.4.2 Zipf's law

Another signature of a phase transition in multifragmentation is the nuclear Zipf's law of fragment size distributions [20, 81, 108]. The Zipf's law was originally formulated for word frequencies in a given language by American linguist G. K. Zipf. He noted that the most frequent word appears approximately twice as often as the second most frequent word, three times as often as the third most frequent and so on, i.e. the frequency of the usage of a word is inversely proportional to its rank [109]. Thus, if words are ranked by their frequency of occurrence ("size"), the frequency f shows a power-law dependence on the rank r

$$f(r) \propto r^{-\lambda} \tag{5.2}$$

with $\lambda \simeq 1$. Interestingly enough, such a rank-size law was also found in many other phenomena, for example, in distributions of city populations [110], the Internet traffic [111], distributions of firm sizes [112], and DNA base pair sequences [113].

Watanabe found in bond percolation simulations that cluster sizes at the critical point also obey Zipf's law [114]. Similar results were obtained with the lattice-gas and molecular dynamical models by Ma, who proposed to use the occurrence of Zipf's law in fragment size distributions as a signature of phase transition in nuclear multifragmentation [20, 81, 108]. Campi and Krivine demonstrated that for infinite systems, the Zipf's law is a mathematical consequence of a power law with the Fisher exponent $\tau \simeq 2$ for cluster size distribution [115]. They concluded that the observation of a Zipf's law is not a new and independent signal of a critical behavior. Moreover, in small systems typical of nuclear fragmentation, the signal and its location can be affected by finite size effects [115, 116]. In spite of this, it has been argued that the Zipf-type plot is a direct observable allowing to characterize the fragment hierarchy in nuclear fragmentation, and as such it is a useful signal of phase transition or critical behavior [81].

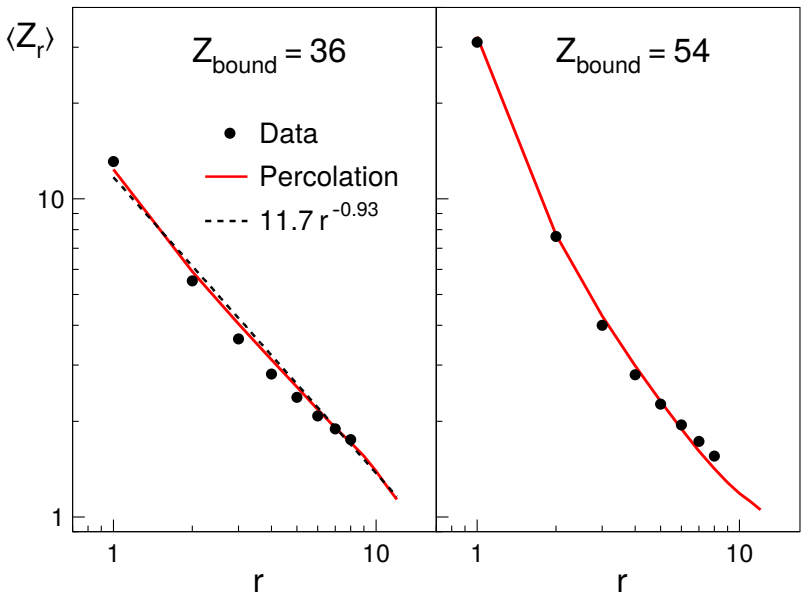

Figure 5.13: Log-log plots of the relation between the average value of fragment charges and their rank r.

Figure 5.13 shows the Zipf-type plots, i.e. the mean size (charge) of the largest (rank $r = 1$), second largest ($r = 2$), third largest ($r = 3$), ... fragments plotted as a function of their rank r for the ALADIN data with comparisons with percolation calculations. The model results are shown for the rank numbers up to 11 because for all considered percolation events, the total fragment multiplicity is at least $m = 11$, as implied by the condition $m > Z_0 - Z_{\mathrm{bound}}$. The experimental data events contain only fragments with $Z > 1$. Since their mean multiplicities for $Z_{\mathrm{bound}} = 36$ and 54 are about 9.1 and 7.7, the mean total multiplicities including $Z = 1$ isotopes may be estimated as 25.1 and 17.7, respectively, by assuming $m_{Z=1} = Z_0 - Z_{\mathrm{bound}}$. It was, therefore, assumed that events containing less than 8 fragments can be supplemented with fragments of $Z = 1$ up to the rank of 8. As can be seen in Fig. 5.13, the percolation model very well describes the data, and an approximate power-law dependence according to the Zipf's law is observed at $Z_{\mathrm{bound}} = 36$. The black dashed line shows a power-law fit to the percolation results, which determined the exponent $\lambda \simeq 0.93$. It is worth noting that this feature appears at the "critical" point while a trace of the asymptotic power-law behavior in the fragment size distribution (with the largest fragment excluded) is observed at the pseudocritical point $Z_{\mathrm{bound}} = 54$. Although the two signatures are related in the thermodynamic limit, they are affected differently by finite size and event sorting effects. The obtained result indicate that the Zipf's law is also a valuable signature in small nuclear systems, which points to the events characteristic of a critical point.

5.4.3 Correlations with the largest fragment

Extended comparisons of the experimental data with predictions of the percolation model are shown in Fig. 5.14. They are performed for four Z_{bound} values, namely $Z_{\mathrm{bound}} = 36, 43, 53$, and 66. The system sizes applied in percolation calculations are $Z_0 = 52, 57, 64$, and 73, respectively, which were found from the matching conditions for K_3 and K_4, as shown in Fig. 5.10. Statistical error bars are omitted in the figure for better readability, however, their magnitude is reflected in the scatter of the data symbols. The top panels show the $P(Z_{\mathrm{max}})$ distributions. Overall, the agreement is very good, although the experimental distributions exhibit some local enhancements which are not accounted for by the model. They are seen for $Z_{\mathrm{bound}} = 36$ and 43 at largest Z_{max}, which correspond to events with one large fragment and few light particles. Such evaporation-like events may be expected even for large excitation energies (small Z_{bound} values), because neutron-rich projectile spectators can be cooled by neutron emissions. Another enhancement observed at $Z_{\mathrm{bound}} = 66$ around $Z_{\mathrm{max}} \simeq 37$ is associated with a contribution from fission events, which is also visible in Fig. 5.5. The next panels in Fig. 5.14 examine various fragment size characteristics and correlations as a function of Z_{max}. They are the mean and variance of the multiplicity of fragments with $Z > 2$, the mean fragment size S_2 defined as the second moment of the fragment size distribution normalized to the first moment (the largest fragment excluded) [83], the mean and variance of the second largest fragment size, and the size asymmetry between the second and third largest fragments $a_{23} \equiv (Z_2 - Z_3)/(Z_2 + Z_3)$ averaged over events with $Z_3 > 2$. These calculations were performed for fragments with $Z > 2$ to avoid contributions from light particles coming from other sources.

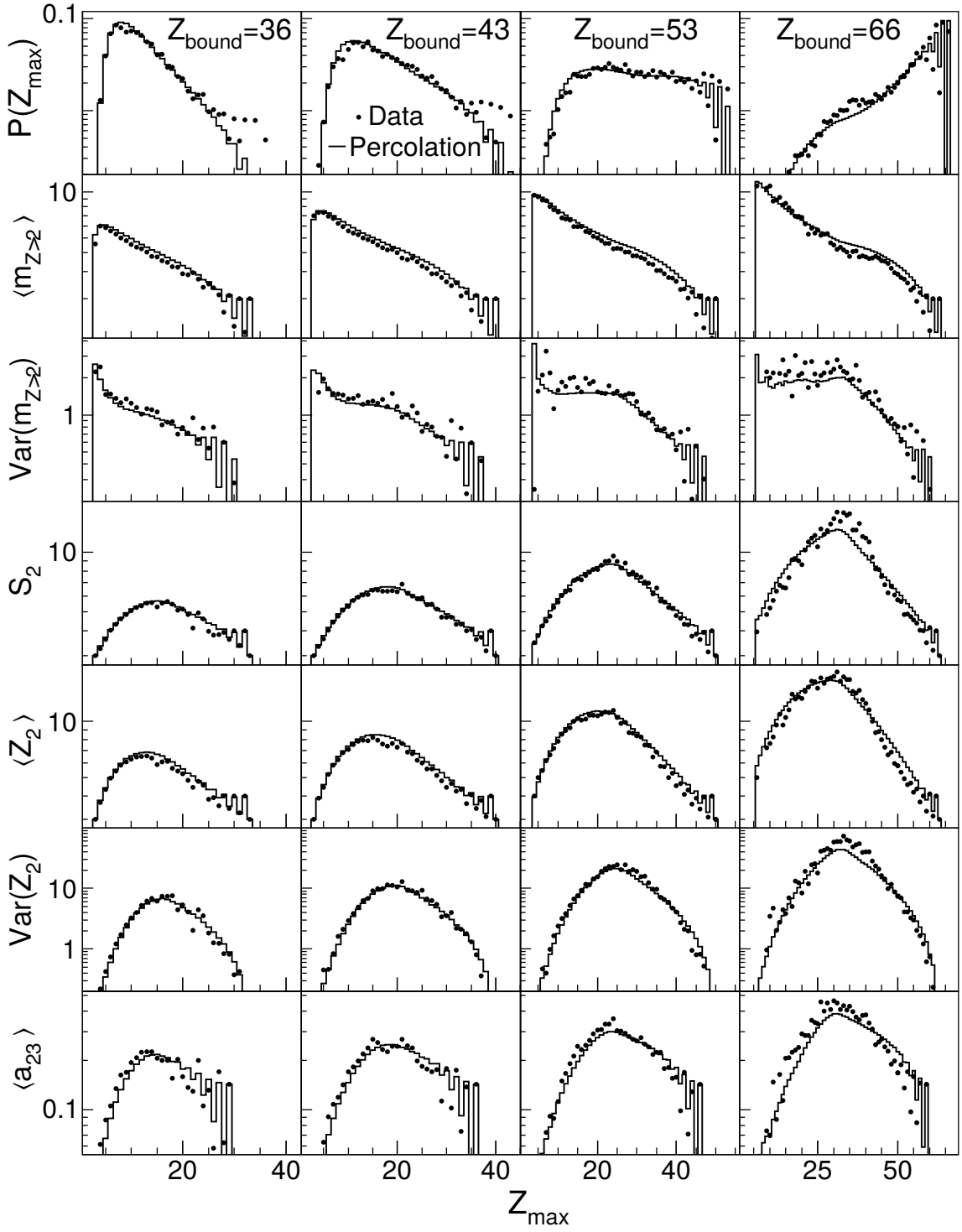

Figure 5.14: Percolation (solid histograms) and experimental data (dots, all systems): Characteristics of fragments with $Z > 2$ plotted as a function of $Z_{\max}$. From top to bottom: the $Z_{\max}$ distribution, the mean and variance of the fragment multiplicity, the mean fragment charge, the mean and variance of the second largest fragment charge, the mean charge asymmetry between the second and third largest fragments. The statistical errors are of the order of the scatter of the data symbols. Figure published in [30].

The question arises whether simultaneously fixed Z_{bound} and Z_{max} will severely limit the possibilities for the fragment-charge partitioning, leading to rather trivial results. This is the case when Z_{max} is close to its limiting minimum or maximum value. The number of possible partitions is largest for Z_{max} in the middle of its range, around $Z_{\mathrm{bound}}/2$. This least restrictive condition allows for a better test of fragmentation patterns. Without additional Z_{max} selection the characteristics would be dominated by the trivial contributions in the cases when $P(Z_{\mathrm{max}})$ distributions are peaked near the limiting Z_{max} values, as for $Z_{\mathrm{bound}} = 36$ and 66 (top row in Fig. 5.14).

The comparisons confirm in detail a close resemblance between the experimental and percolation events (fragment charge/size partitions), not only in the transition region, but also in a wide range of Z_{bound} values.

5.5 Appearance of bimodality signals

A bimodal structure of distributions of the largest fragment size or other quantities expected to be closely correlated with the order parameter is considered as a signature of first-order phase transition [79, 117–119]. The present and other experimental examinations of the largest-fragment charge distribution have not ascertained such a signal. However, the presence of bimodality has been reported for distributions of some other quantities such as the charge asymmetry between the two or three largest fragments, and the asymmetry ratio between heavy and light fragments [20, 38, 79, 120, 121]. In the ALADIN data on ^{197}Au + ^{197}Au at 1000A MeV, a bimodal distribution of $Z_{\mathrm{max}} - Z_2 - Z_3$ has been found in the transition region $Z_{\mathrm{bound}} = 53 - 55$ [79, 122]. As demonstrated by Trautmann [122], the bimodal behavior of this variable can be reproduced by a percolation model, which contains only a second-order phase transition.

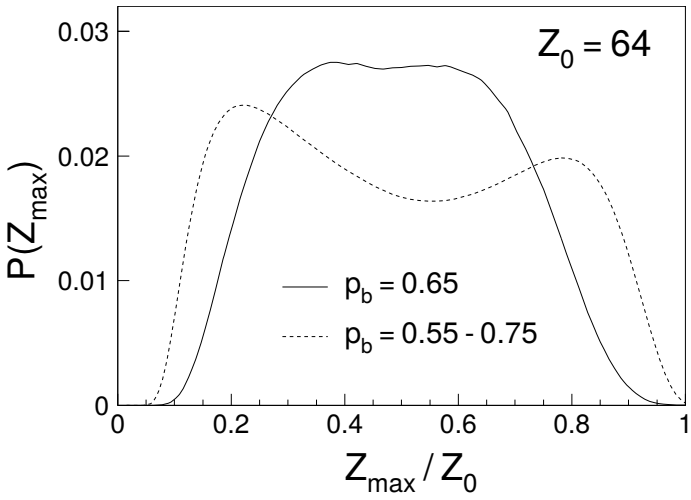

Figure 5.15: Bond percolation for $Z_0 = 64$. The probability distribution of the largest cluster size Z_{max} at the transition point $p_{\mathrm{b}} = 0.65$ (solid line) and for the bond probability distributed over a finite range (dashed line). Figure published in [30].

As expected for the continuous percolation transition, the distribution of $P(Z_{\mathrm{max}})$ does not exhibit bimodality. The shape of the transitional distribution is characterized by a wide

plateau regardless of the system size, as it was shown in Sec.4.2.1 (Fig. 4.9) and is also illustrated in Fig. 5.15 for the system size $Z_0 = 64$ (solid line). Such distribution shapes are observed when events are sorted by the control parameter p_b. If p_b is dispersed in a sample of analyzed events, the shape of $P(Z_{max})$ can be very different. In particular, a bimodal shape may appear as shown in Fig. 5.15 by the dashed line. It warns against using wide bins for event sorting or sorting variables that are not well correlated with the control parameter.

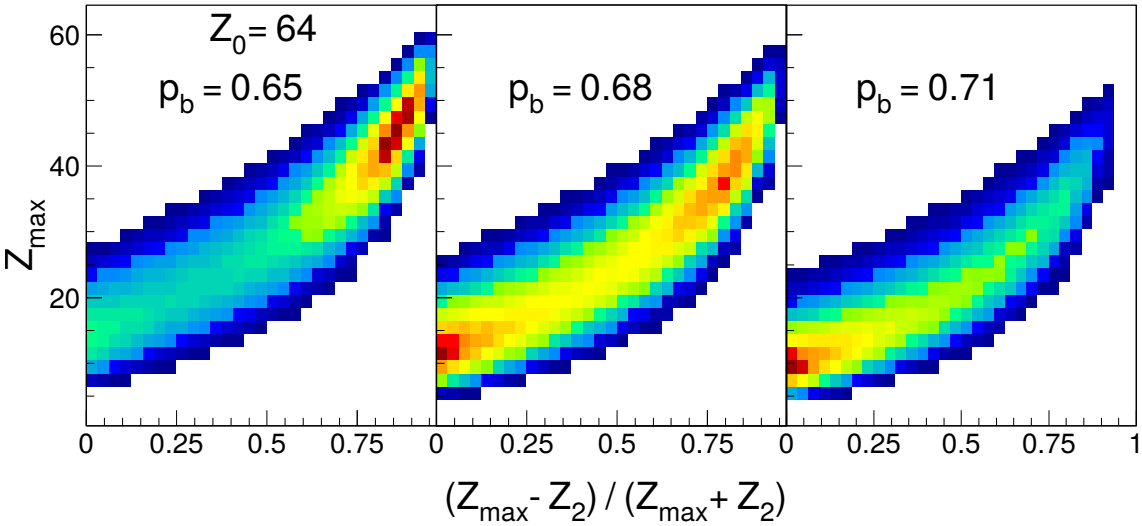

Figure 5.16: Bond percolation for $Z_0 = 64$. Correlations between Z_{max} and the size asymmetry of the two largest clusters in the transition region.

Even when percolation events are sorted by the control parameter, various size asymmetry variables exhibit bimodal behavior in the transition region. As an example, Fig. 5.16 shows the correlation between Z_{max} and the size asymmetry of the two largest fragments $(Z_{max} - Z_2)/(Z_{max} + Z_2)$. A bimodal structure of this distribution is clearly observed at $p_b = 0.68$. It should be noted that the projection onto the Z_{max} axis does not reveal this bimodality. A similar degree of bimodality is observed for a much larger system with 16^3 sites, suggesting that this feature is not generated by finite size effects. Correlations of this kind were examined experimentally for fragmentation of projectiles in ^{197}Au + ^{197}Au and Xe + Sn reactions at 80 MeV/nucleon with qualitatively similar results [121].

Another example concerns the asymmetry between the total sizes of large and small fragments. Following the prescription applied to Xe + Sn central collisions [38], fragments with $Z \geq 13$ are considered as large and fragments with $3 \leq Z \leq 12$ as small. The evolution of their normalized difference distributions near the percolation transition is illustrated in the left diagram of Fig. 5.17. The system size of 100 sites is comparable to the total charge of the investigated nuclear system. Also in this case a bimodal structure is predicted by the percolation model. The right diagram shows the qualitatively similar result that is observed when the clusters with $Z = 1 - 2$ are additionally included in the group of light fragments.

The presented percolation simulations demonstrate that bimodalities observed in distributions of the asymmetry variables are not necessarily associated with a first-order

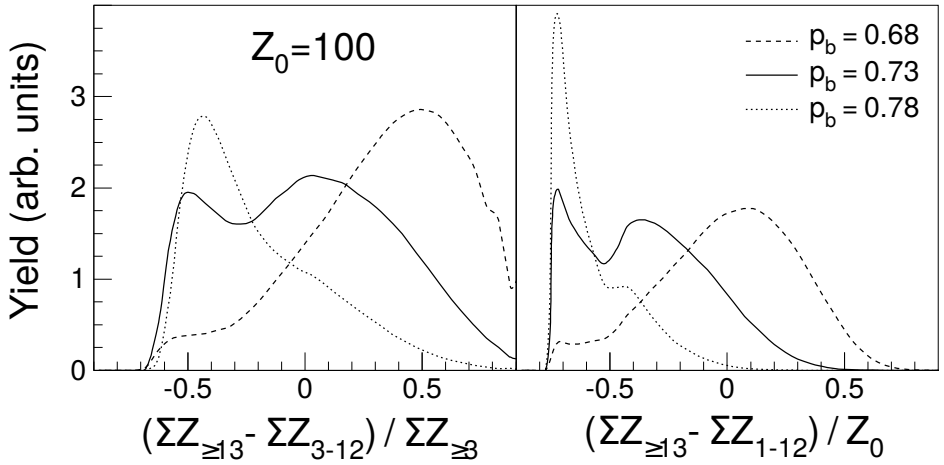

Figure 5.17: Bond percolation for $Z_0 = 100$: distributions of the normalized differences between the sum of atomic numbers of large fragments with $Z \geq 13$ and the sum of atomic numbers of small fragments with $3 \leq Z \leq 12$ (left panel) or with $1 \leq Z \leq 12$ (right panel), calculated for three values of the bond breaking probability p_b below, near, and above the pseudocritical point. Figure published in [30].

phase transition.

5.6 Transition temperature

The analysis of the largest fragment charge fluctuations indicates $Z_{\mathrm{bound}} = 54$ as the transition point for nuclear systems with $Z_0 \simeq 64$. Based on estimations performed for the ^{197}Au + ^{197}Au reaction at 600 MeV/nucleon [27, 68], this point corresponds to the excitation energy around 6 MeV per nucleon, which can be associated with a temperature within the range $5 - 7$ MeV [68, 73, 123]. The isotope temperature determined for this point from double ratios of helium and lithium isotopic yields is about $T_{\mathrm{HeLi}} \simeq 5.4$ MeV as reported in Ref. [123]. In the context of percolation, the transition point may be interpreted as the pseudocritical point. The analysis suggests that near-critical events are rather located at $Z_{\mathrm{bound}} \simeq 36$ where the estimated excitation energy is about 10 MeV per nucleon, corresponding to temperatures between 6 and 7 MeV. These temperatures are well below the critical temperature of about $14 - 15$ MeV, calculated with relativistic mean-field models for asymmetric nuclear matter with a proton fraction of the ^{197}Au nucleus [33, 124]. However, in finite nuclear systems the critical temperature may be reduced by more than 5 MeV as a result of the presence of Coulomb and surface effects [42]. The estimated temperatures depend on the method and size of the system under study. For example, according to calculations with the Fermionic Molecular Dynamics model performed for ^{16}O, the critical temperature deduced from observing the disappearance of the liquid-gas coexistence is about 10 MeV [44]. A somewhat larger value $T_c \simeq 12$ MeV has been concluded from a study of a system of mass number $A = 36$ with antisymmetrized molecular dynamics [45].

The critical temperatures from calculations using the lattice-gas model are within the range from 5 to 8 MeV [15, 16], i.e. much lower than the expected critical temperature for nuclear liquid-gas phase transition even for small systems (cf., e.g., Refs. [42, 44, 45]).

As Le Neindre *et al.* pointed out, these temperatures are comparable with the critical temperatures that appear in analyses based on the Fisher scaling of fragment yields [21]. In fact, the values reported in Refs. [11, 80, 125] are between 4.75 and about 8 MeV. In the lattice-gas model, the critical-like behavior identified by searching for the scaling features of power-law type fragment spectra appears along the Kertész line or its extension into the coexistence zone in the temperature-vs-density phase diagram [12–16, 126]. The wide range of observed temperatures is to be expected since different reaction types and experimental techniques will lead to different approaches of the critical line. There are also some uncertainties associated with determining temperatures from the observed fragment properties and yields.

Chapter 6

Isotopic dependence of spectator fragmentation

6.1 ALADIN experiment S254

The ALADIN experiment S254 was conducted in 2003 at the GSI Schwerionen Synchrotron (SIS) to study isotopic effects in projectile-spectator fragmentation at relativistic energies. A stable beam of neutron-rich ^{124}Sn and radioactive neutron-poor ^{107}Sn and ^{124}La secondary beams were used to explore a wide range of isotopic compositions. The beams with a laboratory energy of 600 MeV/nucleon were directed onto natural Sn targets. The secondary beams were produced at the fragment separator FRS by the fragmentation of primary ^{142}Nd projectiles in a thick beryllium target, and they contained also some fraction of neighboring isotopes. The mean compositions of the nominal ^{124}La (^{107}Sn) beams were $\langle Z \rangle = 56.8(49.7)$ and $\langle A/Z \rangle = 2.19(2.16)$, respectively [127]. Dynamical model studies confirm that these $\langle A/Z \rangle$ values are also representative for spectators produced in the reactions [128, 129].

The ALADIN experimental setup has been presented in the previous chapter. For the S254 experiment, it has been upgraded by constructing new eight proportional readout chambers for the TP-MUSIC IV detector and by redesigning the electronic readout chain [130]. The threshold for fragment detection and identification was below atomic number $Z = 2$ and the resolution permitted individual identification of detected fragments according to their atomic number Z up to the projectile Z_{proj} [29]. The high efficiency of close to 100% for the detection of projectile fragments is an important property of the setup [27]. Tests performed for the case of ^{197}Au fragmentation, confirmed that possible minor inefficiencies have negligible effects on the studied cumulant ratios of the largest fragment size distribution.

The most prominent result of the experiment is the observation that the isotopic dependence of projectile fragmentation is weak [28]. When determined as a function of Z_{bound}, the mean IMF multiplicity, the mean largest fragment charge, and the temperatures deduced from the isotope yields are nearly invariant with respect to the projectile A/Z ratio. As an example, Fig. 6.1 shows the results for the double-isotope temperatures T_{HeLi} and T_{BeLi}.

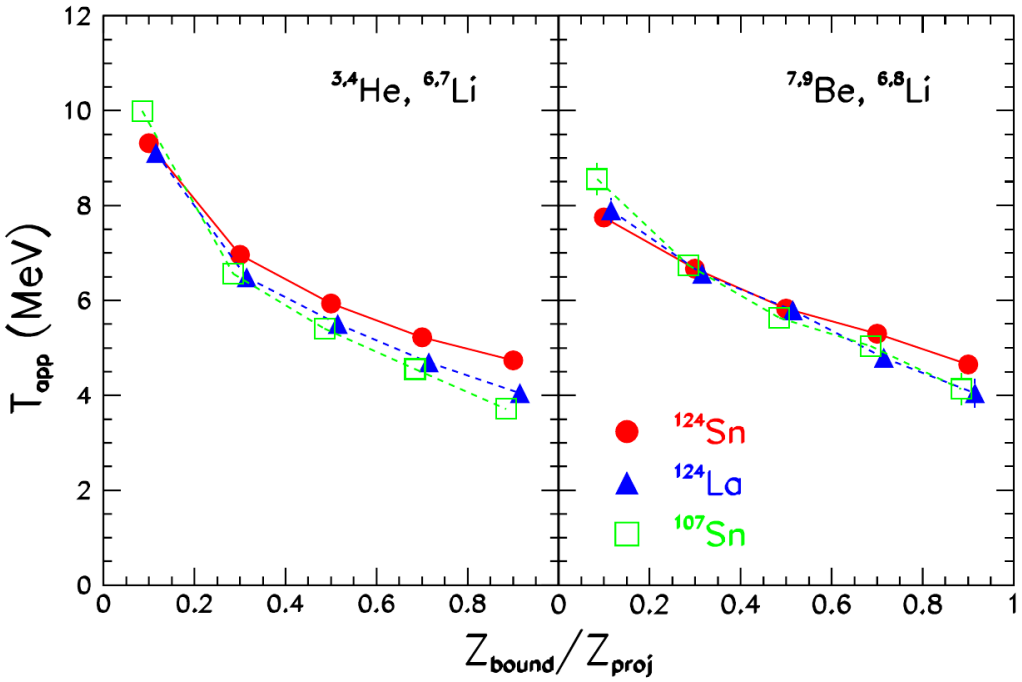

Figure 6.1: Apparent temperatures T_{HeLi} (left panel) and T_{BeLi} (right panel) as a function of Z_{bound} normalized to the projectile charge Z_{proj} for the three studied reactions ^{107,124}Sn+Sn and ^{124}La+Sn at 600 MeV/nucleon. For clarity, two of the three data sets are slightly shifted horizontally, only statistical errors are displayed. Figure from [28].

6.2 Largest fragment charge distributions

In this section, the data analysis is extended to higher order fluctuations of the largest fragment size to examine the transition signals and their isotopic dependence. The distributions of the largest fragment charge (atomic number) as a function of Z_{bound} are illustrated in Fig. 6.2. As can be seen, they exhibit specific lines in their structures

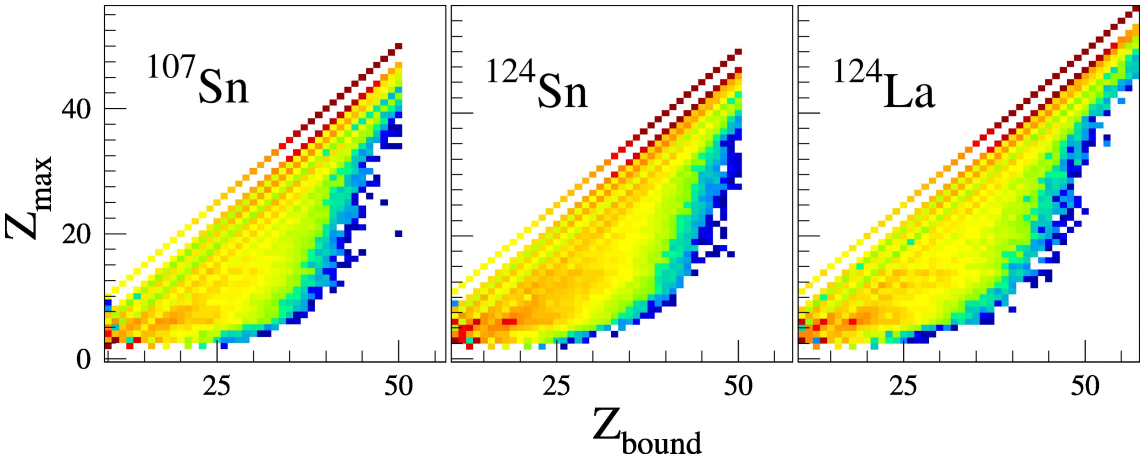

Figure 6.2: Experimental distributions of the largest fragment charge Z_{max} as a function of Z_{bound} for the three reaction systems.

caused by constraints imposed trough the event selection according to Z_{bound}. The main

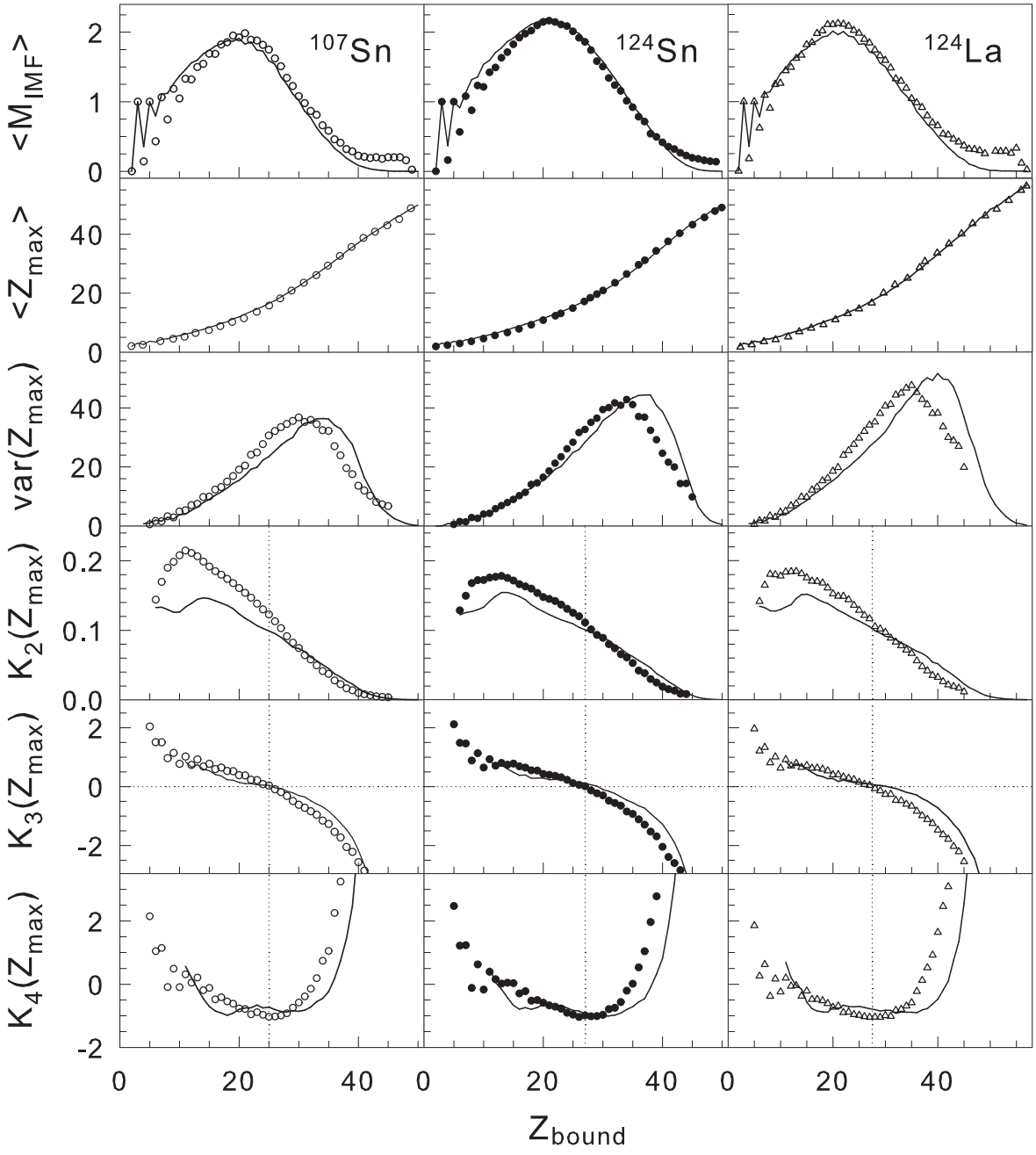

Figure 6.3: Experimental results (symbols) and SMM ensemble calculations (lines) for the mean multiplicity $\langle M_{\mathrm{IMF}} \rangle$ of intermediate-mass fragments, the mean value $\langle Z_{\mathrm{max}} \rangle$ of the largest fragment charge, the variance var (Z_{max}), and the cumulant ratios K_2 to K_4, from top to bottom, as a function of Z_{bound}. The results for K_2 are smoothed to suppress odd-even effects at small Z_{bound}. The dotted vertical lines in the lower panels indicate the observed zero transitions of K_3. Figure published in [31].

statistical measures characterizing the experimental Z_{max} distributions, i.e., the average value, variance and the cumulant ratios K_2, K_3, K_4 are shown by points in Fig. 6.3. In addition, the top row shows the results reported in Ref. [29] for the mean multiplicity of

intermediate-mass fragments (IMF, $3 \leq Z \leq 20$). The rise and fall of the IMF multiplicity as a function of Z_{bound} with maxima slightly exceeding the value $\langle M_{\mathrm{IMF}} \rangle = 2$ is very similar for the three cases. The same holds for the evolution of the mean value $\langle Z_{\mathrm{max}} \rangle$ and the variance $\mathrm{var}(Z_{\mathrm{max}})$ displayed below. The cumulant ratios shown in the lower three rows exhibit the properties known from the percolation and thermodynamic models, qualitatively similar to the case of the ^{197}Au fragmentation discussed in the previous chapter. In particular, the transition points are well determined by the coincident zero transitions of K_3 and the minima of K_4 with values of about -1. For all three systems, they are located in the same small interval of $Z_{\mathrm{bound}} = 25$ for ^{107}Sn to $Z_{\mathrm{bound}} = 27$ for ^{124}Sn and ^{124}La, approximately where $\langle M_{\mathrm{IMF}} \rangle$ rises most steeply with decreasing Z_{bound}.

6.3 SMM description of the experimental results

For the interpretation of the measured fragmentation processes and the observed isotopic effects, the Statistical Multifragmentation Model was applied [29]. An ensemble of excited sources, defined with a few parameters, was used to represent the intermediate stage of the reaction at which equilibrium is assumed, an established method successfully applied in previous interpretations of ALADIN fragmentation data [103, 131]. The disintegration and further deexcitation of excited fragments is then followed within the statistical framework of the model. The experimental data were very well reproduced and, in particular, also the mean value of the largest fragment charge and its evolution with impact parameter were obtained with high accuracy.

Here the analysis is extended to the cumulant ratios of the distributions of the largest fragment charge in order to investigate whether the experimental data and the SMM results equally exhibit the higher-order features. An ensemble of hot sources representing the variety of excited spectator nuclei expected in a participant-spectator scenario was chosen with parameters determined empirically by searching for an optimum reproduction of the measured fragment charge distributions and correlations. As an example, Fig. 6.4 shows the correlation between the atomic number and the excitation energy of the source. The quality of the obtained description for the three studied reaction systems is illustrated in Fig. 6.3. The top two rows present the results reported in Figs. 13, 14 of Ref. [29]. The cumulant ratios in the lower three rows show that the good quality of the reproduction extends to the higher-order properties of the Z_{max} distributions. Some deviations are observed for K_2 in the region of smaller Z_{bound} and for K_3 and K_4 at larger Z_{bound}. A good agreement is observed near and around the transition points (percolation pseudo-critical points) that are equally well determined by the SMM results. As documented in Ref. [29], the evolution of the fragment Z spectra with Z_{bound} exhibits the well-known transition from U-shaped through power-law to exponential spectral forms. The location of the identified transition points falls into the Z_{bound} interval with power-law shaped Z spectra. The statistical errors are omitted in the figure but may be estimated from the scatter of the data points and lines. The significant odd-even effects visible at small Z_{bound} in the multiplicities of intermediate-mass fragments (top row of Fig. 6.3) are caused by the definition of Z_{bound} that includes He fragments. Small even values of Z_{bound} may thus contain larger amounts of multiple ^{4}He events without a fragment with $Z \geq 3$. This is reflected in the cumulant ratios K_3 and K_4 with slightly more peaked and more skewed

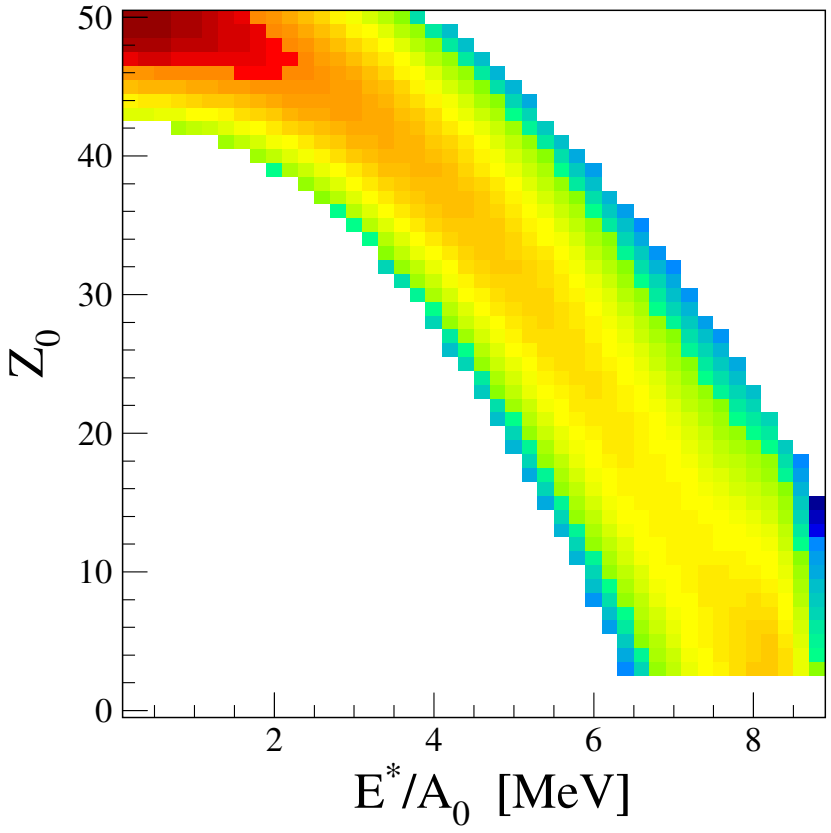

Figure 6.4: Ensemble of hot thermal sources represented in a plot of the atomic number versus the excitation energy per nucleon used in the SMM calculations for reactions with ^{124}Sn projectiles.

distributions for the smaller odd values of Z_{bound}. In the K_2 distributions, this effect has been suppressed by smoothing over the two neighboring values of Z_{bound} with weights [0.25, 0.5, 0.25]. It permits the maxima of K_2 at $Z_{\mathrm{bound}} = 11$ for ^{107}Sn and $Z_{\mathrm{bound}} = 13$ for the two heavier projectiles to appear more clearly. These values may indicate approximate locations of the true critical point as discussed in Ref. [30]. The differences of K_2 at small Z_{bound}, between experimental and model results and between systems, are not surprising because the variances and values of $\langle Z_{\mathrm{max}} \rangle$ are small and the tiny overprediction of $\langle Z_{\mathrm{max}} \rangle$ and underprediction of the variances in some cases have visible effects on K_2.

6.4 Δ-scaling

Properties of the cumulants are of interest in the context of Δ-scaling proposed for revealing a phase transition in finite systems [18, 132, 133]. Probability distributions $P(Z_{\mathrm{max}})$ for different $\langle Z_{\mathrm{max}} \rangle$ values obey Δ-scaling if they can be converted to a single scaling function $\Phi(z_{(\Delta)})$ with the transformation

$$\langle Z_{\mathrm{max}} \rangle^{\Delta} P(Z_{\mathrm{max}}) = \Phi(z_{(\Delta)}) \equiv \Phi\left(\frac{Z_{\mathrm{max}} - \langle Z_{\mathrm{max}} \rangle}{\langle Z_{\mathrm{max}} \rangle^{\Delta}} \right), \tag{6.1}$$

where $1/2 \leq \Delta \leq 1$.

The Δ-scaling method has been applied to distributions of the largest fragment charge with expectations that the distributions obey the $\Delta = 1/2$ scaling in the low temperature (ordered) phase and the $\Delta = 1$ scaling in the high temperature (disordered) phase [18–20, 121, 134]. The transition between the two scaling regimes would signal the presence of a phase transition.

As it was shown in Ref. [24], the percolation model contradicts such expectations. In the percolation disordered phase no Δ-scaling is observed for the largest cluster size. In the ordered phase, the $\Delta = 1/2$ scaling can only be observed for different system sizes at a fixed value of the control parameter, which is difficult to realize experimentally. In addition, for small system sizes corresponding to nuclear systems, this limiting scaling behavior is violated as a consequence of surface effects.

The ALADIN experimental data with events sorted according to Z_{bound} do not show Δ-scaling features in any Z_{bound} range. This can be concluded from Fig. 5.10 for the ^{197}Au spectator fragmentation and from Fig. 6.3 for the present data, considering that $K_3 = \mathrm{const}$ and $K_4 = \mathrm{const}$ are necessary conditions for Δ-scaling [24].

Another consequence of the Δ-scaling is a linear correlation of the logarithms of the variance and of the squared mean value of Z_{max}. As can be seen in Fig. 6.5, such a correlation is not observed. The variation of the slopes is continuous and very smooth. The correlations recorded for the three reactions are nearly identical and also very similar to that reported for ^{131}Xe + ^{27}Al at the same energy in Ref. [30]. They show the odd-even effects at small $\ln(\langle Z_{\mathrm{max}}\rangle^2)$ known to be caused by the definition of Z_{bound} (cf. Fig. 6.3). Qualitatively similar shapes have been reported for percolation [24] and for the canonical lattice gas model with constant density and varying temperature [13].

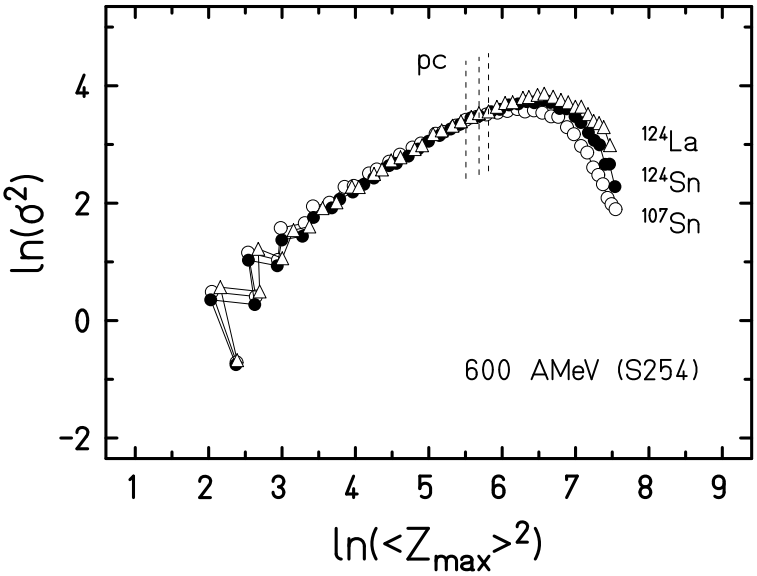

Figure 6.5: Natural logarithm of the variance as a function of the natural logarithm of the squared mean value of the largest atomic number Z_{max} recorded in the three reactions with ^{107}Sn (open circles), ^{124}Sn (filled circles), and ^{124}La (open triangles) projectiles at 600 MeV/nucleon. The data symbols represent the results for individual values of Z_{bound} in the range from 5 to 45. The positions of the pseudocritical (pc) points are indicated by dashed vertical lines and correspond, from left to right, to the ^{107}Sn, ^{124}Sn, and ^{124}La systems. Figure published in [31].

6.5 Isotopic dependence of the breakup temperature

The determined positions of the transition points on the Z_{bound} axis allowed to evaluate the parameters of the fragmenting sources. They are presented in Tab. 6.1, including results obtained for Au projectiles. The mean atomic number Z_0 was estimated on the basis of percolation to be 19% larger than the observed Z_{bound} value at the transition (cf. Fig. 4 in Ref. [30]). The isotopic asymmetry $I = (N-Z)/A$ was assumed to be that of the initial projectiles. The values of the isotope temperature T_{HeLi} were taken from Refs. [28, 123], and the so-called apparent temperatures at the Z_{bound} values of the transition points were used. As indicated by model calculations, the apparent T_{HeLi} may underestimate the actual breakup temperature by up to 15% because of the effects of secondary decays [123] and corrections of 20% were used in Refs. [28, 74]. Here the observed values are found to be on average 0.4 MeV, i.e. less than 10%, lower than the mean microcanonical temperatures obtained with the SMM for the same breakup points [29]. The statistical errors of T_{HeLi} are below 0.1 MeV [28], so that the experimental results indicate a minor dependence on the isotopic composition of the system. The measured values are lower by ≈ 0.4 MeV in the case of the neutron-poor, i.e. more highly charged, systems. This is not reflected in the calculated SMM and CTM results (Table 6.1) nor is it evident from the apparent T_{BeLi} isotope temperatures of 5.6 to 5.7 MeV reported in Ref. [28].

Projectile	Z_{bound}	Z_0	I	T_{HeLi} (MeV)	T_{SMM} (MeV)	T_{CTM} (MeV)
^{107}Sn	25	30 ± 2	0.074	5.4	6.0	5.5
^{124}Sn	27	32 ± 2	0.194	5.8	5.9	5.6
^{124}La	27	32 ± 2	0.086	5.5	6.0	5.5
^{197}Au	54	64 ± 2	0.198	5.4	5.2	5.2

Table 6.1: Freeze-out characteristics of the four fragmenting systems at the transition points Z_{bound}: the estimated atomic number Z_0, the asymmetry $I = (N-Z)/A$ of the projectile (averaged over the beam composition for the radioactive projectiles), the apparent temperature T_{HeLi} at the transition point from Refs. [28, 123], the mean microcanonical temperature T_{SMM} from Ref. [29], and the CTM freeze-out temperature calculated for the indicated system charge Z_0 and asymmetry I.

The isotopic and system size dependence of the breakup temperature is shown again in Fig. 6.6, together with predictions obtained with the SMM and CTM as well as from the Hartree-Fock calculations reported by Besprosvany and Levit [47]. For this purpose, SMM and CTM calculations were performed for many systems covering the interval of $20 \lesssim Z_0 \lesssim 80$, for the two indicated asymmetries I, and by generating events over wide ranges of either the excitation energy (SMM) or the temperature (CTM). The transition points were identified on the basis of the obtained cumulant ratios by searching for their characteristic signal. In the case of the SMM, the microcanonical breakup temperatures derived in this way for the experimentally studied systems are within ≈ 0.2 MeV the same as the results of the ensemble calculations listed in the table. The results for the neutron-poor and the neutron-rich cases are shown separately in the two panels. The experimental temperatures T_{HeLi} are given with an assumed error of ± 0.3 MeV and

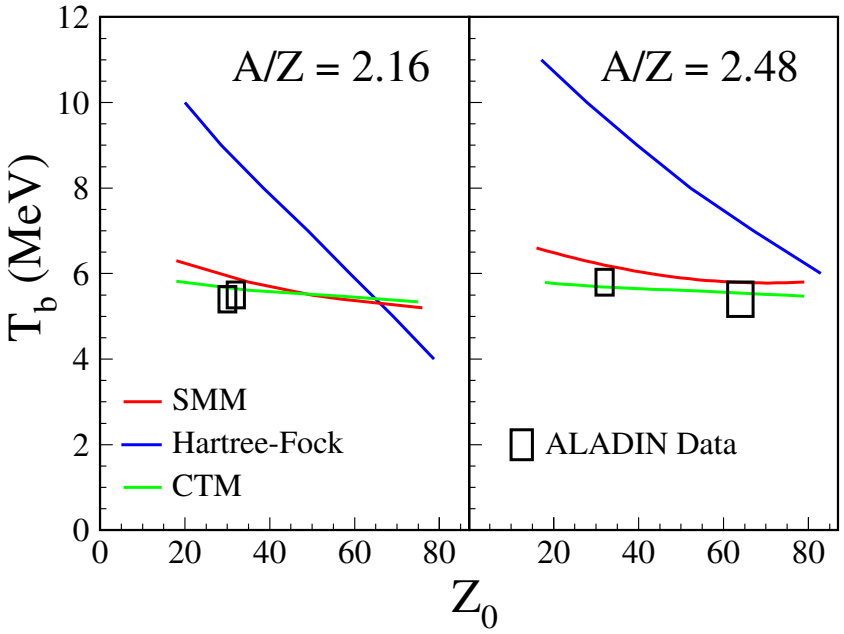

Figure 6.6: Breakup temperatures T_b as a function of the reconstructed atomic number Z_0 of the disintegrating system at the pseudocritical breakup point for neutron-poor (left) and neutron-rich (right) systems. The boxes represent the apparent chemical breakup temperatures T_{HeLi} from Table 6.1 with an assumed error of ± 0.3 MeV while the lines give the model results as indicated. The value 5.4 ± 0.4 MeV for the fragmentation of ^{197}Au [123] is included in the right panel.

include $T_{\mathrm{HeLi}} = 5.4 \pm 0.4$ MeV for ^{197}Au at $Z_{\mathrm{bound}} = 54$ from Ref. [123], corresponding to $Z_0 = 64$. After applying the same 20% correction, these values are in very good agreement with the plateau temperatures of caloric curves compiled by Natowitz *et al.* [74]. It is evident that the fragmentation occurs at temperatures lower than those expected for the Coulomb instabilities of equilibrated compound nuclei investigated with the Hartree-Fock model [47]. The magnitudes of the latter may still depend on the form of the nuclear potential used in the calculations [46, 135] but the predicted dependences on the mass and isotopic composition of the system are much stronger than in the statistical models and as observed here and in other fragmentation reactions [136].

Chapter 7

Summary and conclusions

The main aim of this thesis work was to study the phase transition in nuclear multifragmentation by examining properties of the largest fragment size distribution, which reflects event-to-event fluctuations. The size of the largest fragment plays the role of the order parameter in multifragmentation, and thus is expected to provide valuable information about the phase behavior of fragmenting systems. Bond percolation studies presented in [24] suggested new signatures of a critical behavior (second-order phase transition) associated with the cumulant ratios of the largest fragment size distribution: the normalized variance K_2, skewness K_3 and kurtosis excess K_4. In particular, the pseudocritical point in finite percolation systems is indicated by $K_3 = 0$ coinciding with a minimum of K_4.

Here, the properties of the largest fragment size distribution (mass or charge) have been studied within statistical models: the Canonical Thermodynamic Model (CTM) and the Copenhagen Statistical Multifragmentation Model (SMM). The simplified one - component CTM is known to contain a first-order phase transition and allows calculations in a wide range of system sizes. As for the canonical ensemble, the control parameter is the temperature. In finite systems the transition is indicated by a maximum of the specific heat C_V that becomes increasingly pronounced as the system grows in size. It is shown that this transition point coincides with the zero transition of K_3 and minimum of K_4. This result demonstrates that the transition point in small systems, associated with a phase transition in the thermodynamic limit, is well indicated by this cumulant signature for both, i.e. first- and second-order, types of transition. Although in both cases the K_3 and K_4 measures of the largest fragment size distribution have the same characteristics, the distribution shapes are different. In CTM the distribution exhibits bimodality (two peaks corresponding to the coexisting gas and liquid phases), while in percolation the distribution has a wide plateau. The bimodality signal is also present in correlations between the largest and the second largest fragment sizes. However, a distinct bimodality is observed for large systems and gradually vanishes as the system size decreases. The derived transition temperature is in the range 6 to 7.5 MeV depending on the system size and the freeze-out volume. Calculations with the more realistic two-component CTM and SMM corroborate conclusions from the percolation and one-component CTM studies that the specific characteristics of K_3 and K_4 can indicate a phase transition in small systems. The transition temperature is influenced by the introduced Coulomb and neutron-proton symmetry energies. It is around 5.5 MeV,

nearly independently of the system size and the neutron-proton asymmetry.

Fragment size (charge or atomic number Z) distributions have been studied using the ALADIN data on fragmentation of ^{197}Au projectiles at energies between 600 and 1000 MeV/nucleon. The analysis was focused on the largest fragment charge fluctuations. The cumulant ratios of the largest fragment size distribution were examined as a function of Z_{bound}, which is correlated with the excitation energy and plays the role of the control parameter. The transition point indicated by $K_3 = 0$ and a minimum of K_4 is observed at $Z_{\mathrm{bound}} = 54$ which, according to Ref. [123], corresponds to excitation energies near 6 MeV/nucleon, associated with a temperature around 5.5 MeV. In percolation, it corresponds to the pseudocritical point, and in the thermodynamic model, to the maximum of the specific heat that is associated with a first-order phase transition. Based on percolation simulations, the cumulants K_3 and K_4 are shown to be not significantly affected by experimental conditions and secondary decay effects. They were used as constraints in comparison with bond percolation predictions to determine the system sizes at different Z_{bound} values. The system sizes found with this method are in good agreement with experimental estimates. Extensive comparisons with predictions of the bond percolation model were made to test the whole fragmentation pattern. They have shown that the fragment sizes and their event-to-event fluctuations observed in the experiment are remarkably well reproduced by the model. The analysis suggests that near-critical events, corresponding to the percolation critical point in the continuous limit, are located at $Z_{\mathrm{bound}} = 36$. The associated excitation energy is about 10 MeV/nucleon, leading to a temperature of approximately 6 to 7 MeV [68], [123].

Due to the high accuracy in describing the fragment size properties, the percolation model, containing a second-order phase transition, can serve as a very useful reference model for studying the phase behavior of fragmenting systems. In particular, it permits verifying the uniqueness of signatures proposed for revealing the presence of a first-order phase transition. It should to be stressed, however, that model comparisons, in order to be applicable to experimental verification, must rely on event samples selected with measurable quantities, such as for example Z_{bound}. These sorting quantities are inevitably dispersed over the control parameter of the model as, e.g., the temperature or the bond probability, which may significantly modify or artificially create investigated signatures. As an example, it has been shown with percolation simulations that bimodality may appear in the largest fragment size distribution when events are selected with Z_{bound}.

The cumulant analysis of the largest fragment charge distributions has been applied to the ALADIN S254 experimental data to investigate the isotopic dependence of projectile fragmentation. The experiment was conducted with neutron-rich ^{124}Sn and radioactive neutron-poor ^{107}Sn and ^{124}La beams of 600 MeV/nucleon incident energy and natural Sn targets [28, 29]. The coincident zero transitions of K_3 and the minima of K_4 with values of about -1 are observed at Z_{bound}=25 for ^{107}Sn and Z_{bound}=27 for ^{124}Sn and ^{124}La indicating the transition points. Their locations are nearly independent of the projectile A/Z ratio. It is shown that the SMM model in the form used to successfully describe the fragment distributions and correlations of the studied reaction [29] reproduces also the fluctuations of the largest fragment charge. The evolutions of the experimental and calculated cumulant ratios with Z_{bound} follow each other rather well, and quite precisely near the transition. The locations of the transition points on the

Z_{bound} axis allow to estimate the associated temperatures. For all investigated reaction systems, including reactions with Au projectiles, the temperatures determined from the measured isotopic ratios T_{HeLi} are around 5.5 MeV [28, 123] in a good agreement with predictions of the statistical models, showing only a very weak dependence of the transition temperatures on the A/Z ratio and size of the fragmenting system. This confirms the earlier observations (Refs. [28, 29, 137]) that the fragmentation process is governed by the opening of the corresponding partition space and less likely by a possible Coulomb instability related to the system charge. Overall, the studies corroborated the suggestion derived from percolation that the cumulant ratios skewness K_3 and kurtosis excess K_4 of the distributions of the largest fragment size (charge) are valuable observables in searching for a phase transition in multifragmentation. It has been shown that K_3=0 coinciding with a minimum of K_4 indicates not only the second-order percolation transition but also the transitions observed in CTM and SMM statistical models that are believed to be associated with a first-order phase transition in the thermodynamic limit. The observed properties of the cumulant ratios appear generic for fragmentation processes. It will be interesting to investigate their existence in other fragmentation models.

The presented very detailed quantitative analysis has demonstrated that the bond percolation model with no free parameters remarkably well describes the experimental fragment sizes and their fluctuations. It should be stressed that no correction for the secondary decays was applied in the analysis. In the context of the lattice-gas model, which is similar to bond percolation near the normal density, the success of percolation suggests that clusters are formed in the dense medium and isolated fragments are cold, in accordance with the "Little big bang" scenario of multifragmentation proposed in Ref. [10, 138]. However, the location of the transition in a temperature vs density phase diagram is uncertain. Calculations with the lattice-gas model performed for small systems demonstrated that critical-like behavior can also be observed in the liquid-gas coexistence zone of the phase diagram at low densities [12–16]. It has recently been shown by investigating the lattice-gas, percolation and thermodynamic models that all three models provide qualitative descriptions of experimental data while the transition points are indicative of either a first- or a second-order phase transition, depending the applied model [139]. Further investigations, particularly with quantum molecular dynamics calculations that reproduce the experimental fragmentation patterns, are required for better understanding of the phase transition signals in nuclear multifragmentation processes.

Acknowledgements:

The author would like to express his gratitude to the ALADIN Collaboration for the permission to use the event-sorted fragmentation data.

I am very grateful to my promoter prof. dr hab. Janusz Brzyczyk for his time, valuable comments and support throughout the writing process.

I also thank my family who supported me during this work.

Bibliography

[1] P. J. Siemens Nature **305**, 410 (1983).

[2] H. Jaqaman, A. Z. Mekjian, and L. Zamick, Phys. Rev. C **27**, 2782 (1983).

[3] A. L. Goodman, J. I. Kapusta, and A. Z. Mekjian, Phys. Rev. C **30**, 851 (1984).

[4] W. Bauer, D. R. Dean, U. Mosel, and U. Post, Phys. Lett. B **150**, 53 (1985).

[5] W. Bauer, Phys. Rev. C **38**, 1297 (1988).

[6] X. Campi, J. Phys. A **19**, L917 (1986).

[7] X. Campi, Phys. Lett. B **208**, 351 (1988).

[8] P. Kreutz, *et al.*, Nucl. Phys. A, **556** p. 672 (1993).

[9] T. Li et al., Phys. Rev. C **49**, 1630 (1994).

[10] X. Campi, H. Krivine, N. Sator, and E. Plagnol, Eur. Phys. J. D **11**, 233 (2000).

[11] M. Kleine Berkenbusch *et al.*, Phys. Rev. Lett. **88**, 022701 (2002).

[12] J. M. Carmona, J. Richert, and P. Wagner, Phys. Lett. B **531**, 71 (2002).

[13] F. Gulminelli and Ph. Chomaz, Phys. Rev. C **71**, 054607 (2005).

[14] F. Gulminelli and Ph. Chomaz, Phys. Rev. Lett. **82**, 1402 (1999).

[15] C. B. Das *et al.*, Phys. Rev. C **66**, 044602 (2002).

[16] A. Wieloch, J. Brzychczyk, J. Łukasik, P. Pawłowski, T. Pietrzak, and W. Trautmann, in *Proceedings of the IWM2009 International Workshop on Multifragmentation and Related Topics*, Catania, Italy, edited by J. D. Frankland, A. Pagano, S. Pirrone, M-F. Rivet, and F. Rizzo (Conference Proceedings Vol. 101, Italian Physical Society, Bologna 2010), p. 158; preprint arXiv:nucl-th/1003.2794.

[17] S. Das Gupta, A.Z. Mekjian Phys. Rev. C **57**, 1361 (1998).

[18] R. Botet, M. Płoszajczak, A. Chbihi, B. Borderie, D. Durand, and J. Frankland, Phys. Rev. Lett. **86**, 3514 (2001).

[19] J. D. Frankland *et al.*, Phys. Rev. C **71**, 034607 (2005).

[20] Y. G. Ma *at al.*, Phys. Rev. C **71**, 054606 (2005).

[21] N. Le Neindre *et al.*, Nucl. Phys. A **795**, 47 (2007).

[22] P. Das, S. Mallik, G. Chaudhuri, Phys. Lett. B **783**, 364 (2018).

[23] B. Borderie, J.D. Frankland, Prog. Part. Nucl. Phys. **105**, 82 (2019).

[24] J. Brzychczyk, Phys. Rev. C **73**, 024601 (2006).

[25] C. B. Das, S. Das Gupta, W. G. Lynch, A. Z. Mekjian, M. B. Tsang, Phys. Rep. **406**, 1. (2005).

[26] J. P. Bondorf, A. S. Botvina, A. S. Ilinov, I .N. Mishustin, K. Sneppen, Phys. Rep. **257**, 133 (1995).

[27] A. Schüttauf *et al.*, Nucl. Phys. A **607**, 457 (1996).

[28] C. Sfienti, *et al.*, Phys. Rev. Lett. **102**, 152701 (2009).

[29] R. Ogul, *et al.*, Phys. Rev. C **83** 024608 (2011) and Erratum, ibid. **85**, 019903(E) (2012).

[30] J. Brzychczyk, T. Pietrzak, A. Wieloch, W. Trautmann, Phys. Rev. C **98**, 054606 (2018).

[31] T. Pietrzak, A. S. Botvina, J. Brzychczyk, N. Buyukcizmeci, A. Le Fèvre *et al.* Phys. Lett. B **809**, 135763 (2020).

[32] T. Pietrzak *et al.*, in *Proceedings of the IWM2009 International Workshop on Multifragmentation and Related Topics*, Catania, Italy, edited by J. D. Frankland, A. Pagano, S. Pirrone, M-F. Rivet, and F. Rizzo (Conference Proceedings Vol. 101, Italian Physical Society, Bologna 2010), p. 171; preprint arXiv:nucl-ex/1003.2800.

[33] H. Müller, B. D. Serot, Phys. Rev. C **52**, 2072 (1995).

[34] P. Chomaz, M. Colonna, J. Randrup, Phys. Rep. **389**, 263 (2004).

[35] B. Borderie, M. F. Rivet, Prog. Part. Nucl. Phys. **61**, 551 (2008).

[36] S. Typel, G. Röpke, T. Klähn, D. Blaschke, H. H. Wolter, Phys. Rev. C **81**, 015803 (2010).

[37] G. Bertsch and P. J. Siemens, Phys. Lett. B **126**, 9 (1983).

[38] B. Borderie, J. Phys. G: Nucl. Part. Phys. **28**, R217 (2002).

[39] V. Baran, M. Colonna, M. Di Toro, V. Greco, Phys. Rev. Lett. **86**, 4492 (2001).

[40] J. Margueron, P. Chomaz, Phys. Rev. C **67**, 41602 (2003).

[41] B. A. Li, L. W. Chen, H. R. Ma, J. Xu and G. C. Yong, Phys. Rev. C **76**, 051601 (2007).

[42] H. R. Jaqaman, A. Z. Mekjian, and L. Zamick, Phys. Rev. C **29**, 2067 (1984).

[43] J. N. De, B. K. Agrawal, S. K. Samaddar, Phys. Rev. C **59**, R1 (1999).

[44] J. Schnack and H. Feldmeier, Phys. Lett. B **409**, 6 (1997).

[45] T. Furuta and A. Ono, Phys. Rev. C **74**, 014612 (2006).

[46] S. Levit, P. Bonche, Nucl. Phys. A **437**, 426 (1985).

[47] J. Besprosvany, S. Levit, Phys. Lett. B **217**, 1 (1989).

[48] H. R. Jaqaman, Phys. Rev. C **39**, 169 (1989); **40**, 1677 (1989).

[49] H. Q. Song, R. K. Su, Phys. Rev. C **44**, 2505 (1991).

[50] H. Q. Song, Z. X. Qian, R. K. Su, Phys. Rev. C **47**, 2001 (1993); **49**, 2924 (1994).

[51] Y. J. Zhang, R. K. Su, H. Song, F. M. Lin, Phys. Rev. C **54**, 1137 (1996).

[52] M. Baldo, L. S. Ferreira, Phys. Rev. C **59**, 682 (1999).

[53] J. N. De, S. Das Gupta, S. Shlomo, and S. K. Samaddar, Phys. Rev. C **55**, R1641 (1997).

[54] P. Wang, D. B. Leinweber, A. W. Thomas, A. G. Williams, Nucl. Phys. A **748**, 226 (2005).

[55] S. Talahmeh and H. R. Jaqaman, J. Phys. G: Nucl. Part. Phys. **40**, 015103 (2013).

[56] J. E. Finn *et al.*, Phys. Rev. Lett. **49**, 1321 (1982).

[57] R. W. Minich *et al.*, Phys. Lett. B **118**, 458 (1982).

[58] M. E. Fisher, Physics (N.Y.) **3**, 255 (1967).

[59] R. T. de Souza, N. Le Neindre, A. Pagano, and K.-H. Schmidt, Eur. Phys. J. A **30**, 275 (2006).

[60] A. Le Fèvre *et al.*, Phys. Rev. C **80**, 044615 (2009).

[61] R. T. de Souza *et al.*, Nucl. Instrum. Methods A **295**, 109 (1990).

[62] D. R. Bowman *et al.*, Phys. Rev. Lett. **67**, 1527 (1991).

[63] Y. D. Kim *et al.*, Phys. Rev. Lett. **67**, 14 (1991).

[64] Multipurpose charged particle array at Texas A&M University, see http://cyclotron.tamu.edu/nimrod/ .

[65] J. Pouthas *et al.*, Nucl. Instrum. Methods A **357**, 418 (1995).

[66] A. Pagano *et al.*, Nucl. Phys. A **681**, 331c (2001).

[67] V. E. Viola *et al.*, Physics Reports **434**, 1 (2006).

[68] J. Pochodzalla *et al.*, Phys. Rev. Lett., **75**, 1040 (1995).

[69] V. E. Viola and R. Bougault, Eur. Phys. J. A **30**, 215 (2006).

[70] A. Kelić, J. B. Natowitz, and K.H. Schmidt, Eur. Phys. J. A **30**, 203 (2006).

[71] J. P. Bondorf, R. Donangelo, I. N. Mishustin, H. Schulz, Nucl. Phys. A **444**, 460 (1985).

[72] T. Faruta, A. Ono, Prog. Theor. Phys. Suppl. **156**, 147 (2004).

[73] J. B. Natowitz *et al.*, Phys. Rev. C **65**, 034618 (2002).

[74] J. B. Natowitz *et al.*, Phys. Rev. Lett. **89**, 212701 (2002).

[75] R. J. Furnstahl *et al.*, Nucl. Phys. A **615**, 441 (1997).

[76] L. L. Zhang *et al.*, Phys. Rev. C **59**, 3292 (1999).

[77] M. D'Agostino *et al.*, Nucl. Phys. A **650**, 329 (1999).

[78] B. Borderie *et al.*, Phys. Rev. Lett. **86**, 3252 (2001).

[79] O. Lopez and M. F. Rivet, Eur. Phys. J. A **30**, 263 (2006).

[80] J. B. Elliott *et al.*, Phys. Rev. C **67**, 024609 (2003).

[81] Y. G. Ma, Eur. Phys. J. A **30**, 227 (2006).

[82] S. Broadbent and J. Hammersley,
Percolation Processes I. Crystals and Mazes.
Proceedings of the Cambridge Philosophical Society, 53, 629-641 (1957).

[83] D. Stauffer and A. Aharony,
Introduction to Percolation Theory
(Taylor & Francis, London, 2003).

[84] M. Sahimi,
Applications of Percolation Theory
(Taylor & Francis, London, 1994).

[85] B. Jakobsson, G. Jönsson, B. Lindkvist, A. Oskarsson Z. Phys. A, **307** p. 293 (1982).

[86] A.S. Hirsch, *et al.*, Phys. Rev. C **29**, p. 508 (1984).

[87] W. Bauer, A. Botvina Phys. Rev. C **52**, R1760 (1995).

[88] J. Hoshen and R. Kopelman, Phys. Rev. B **14**, 3438 (1976).

[89] K. A. Bugaev, M. I. Gorenstein, I. N. Mishustin, and W. Greiner, Phys. Lett. B **498**, 144 (2001).

[90] P. Bhattacharyya, S. Das Gupta and A. Z. Mekjian, Phys. Rev. C **60**, 054616 (1999).

[91] A. Botvina, G. Chaudhuri, S. Das Gupta and I. N. Mishustin, Phys. Lett. B **668**, 414 (2008).

[92] S. Das Gupta, A. Z. Mekjian and M. B. Tsang, Advances in Nuclear Physics **26**, 89 (2001) (Kluwer Academic/Plenum Publishers, New York).

[93] V. E. Viola, K. Kwiatkowski, J. B. Natowitz, and S. J. Yennello, Phys. Rev. Lett. **93**, (2004).

[94] G. Chaudhuri, S. Das Gupta, arXiv::0612037v3 [nucl-th] (2007).

[95] W. Trautmann, the ALADIN Collaboration, arXiv::0705.0678v1 [nucl-ex] (2007).

[96] G. Chaudhuri, S. Das Gupta, F. Gulminelli, Nucl. Phys. A **815**, 89 (2009).

[97] P. F. Mastinu *et al.*, Phys. Rev. Lett. **76**, 2647 (1996).

[98] A. S. Botvina, A. S. Iljinov, I. N. Mishustin, J. P. Bondorf, R. Donangelo, and K. Sneppen, Nucl. Phys. A **475**, 663 (1987).

[99] J. Hubele *et al.*, Z. Phys. A **340**, 263 (1991).

[100] A. Schüttauf, Ph.D. thesis, Universität Frankfurt am Main, 1996.

[101] J. Pochodzalla *et al*., Phys. Rev. Lett. **75**, 1040 (1995).

[102] X. Campi, H. Krivine, and E. Plagnol, Phys. Rev. C **50**, R2680 (1994).

[103] A. S. Botvina, *et al.*, Nucl. Phys. A **584**, 737 (1995).

[104] W. Trautmann, U. Milkau, U. Lynen, and J. Pochodzalla Z. Phys. A **344**, 447, (1993).

[105] M. Huang *et al.*, Phys. Rev. C **82**, 054602 (2010).

[106] C. D. Lorenz and R. M. Ziff, Phys. Rev. E **57**, 230 (1998).

[107] Y. G. Ma, arXiv:nucl-ex/0610014.

[108] Y. G. Ma, Phys. Rev. Lett. **83**, 3617 (1999).

[109] G. K. Zipf, *Human Behavior and the Principle of Least Effort* Addison-Wesley, Cambridge, MA, 1949.

[110] X. Gabaix *Zipf's Law and the Growth of Cities* Am. Econ. Rev. **89**, 129 (1999).

[111] R. Albert and A.-L. Barabasi, Rev. Mod. Phys. **74**, 47 (2002).

[112] R. L. Axtel, Science **293**, 1818 (2001).

[113] R. N. Mantegna *et al.*, Phys. Rev. Lett. **73**, 3169 (1994).

[114] M. Watanabe, Phys. Rev. E **53** 4187 (1996).

[115] X. Campi and H. Krivine, Phys. Rev. C **72**, 057602 (2005).

[116] K. Paech, W. Bauer, and S. Pratt, Phys. Rev. C **76**, 054603 (2007).

[117] Ph. Chomaz, F. Gulminelli, V. Duflot, Phys. Rev. E **64**, 046114 (2001).

[118] D.H.E. Gross, Eur. Phys. J. A **30**, 293 (2006), and in *Dynamics and Thermodynamics with Nuclear Degrees of Freedom*, ed. by Ph. Chomaz et al., Springer, Berlin Heidelberg New York, 2006.

[119] E. Bonnet *et al*., Phys. Rev. Lett. **103**, 072701 (2009).

[120] N. Bellaize *et al.*, Nucl. Phys. A **709**, 367 (2002).

[121] M. Pichon *et al*., Nucl. Phys. A **779**, 267 (2006).

[122] W. Trautmann *et al.* in *Proceedings of the XLVth International Winter Meeting on Nuclear Physics, Bormio, Italy*, edited by I. Iori and A. Tarantola (Ricerca Scientifica ed Educazione Permanente Suppl. No. 127, Milano, 2007), p. 205.

[123] W. Trautmann *et al*., Phys. Rev. C **76**, 064606 (2007).

[124] Guang-Hua Zhang, Wei-Zhou Jiang, Phys. Lett. B **720**, 148 (2013).

[125] J. B. Elliott *et al.*, Phys. Rev. Lett. **88**, 042701 (2002).

[126] X. Campi and H. Krivine, Nucl. Phys. A **620**, 46 (1997).

[127] J. Lukasik *et al.*, Nucl. Instr. and Meth. A **587**, 413 (2008).

[128] A. Le Fevre *et al.*, Phys. Rev. Lett. **94**, 162701 (2005).

[129] A. S. Botvina, O. V. Lozhkin, and W. Trautmann, Phys. Rev. C **65**, 044610 (2002).

[130] C. Sfienti *et al.*, in Proceedings of the XLIst International Winter Meeting on Nuclear Physics, Bormio, Italy, edited by I. Iori and A. Moroni (Ricerca Scientifica ed Educazione Permanente Suppl. vol. 120, Milano 2003), p. 323.

[131] H. W. Barz *et al.*, Nucl. Phys. A **561**, 466 (1993).

[132] R. Botet and M. Płoszajczak, Phys. Rev. E **62**, 1825 (2000).

[133] R. Botet and M. Płoszajczak, Nucl. Phys. B (Proc. Suppl.) **92**, 101 (2001).

[134] D. Gruyer *et al*., Phys. Rev. Lett. **110**, 172701 (2013).

[135] M. Baldo, L. S. Ferreira and O. E. Nicotra, Phys. Rev. C **69**, 034321 (2004).

[136] X. Liu *et. al*, Phys. Rev. C **100**, 064601 (2019).

[137] N. Buyukcizmeci, R Ogul and A. S. Botvina, Eur. Phys. J. A **25**, 57 (2005).

[138] X. Campi, H. Krivine, E. Plagnol, and N. Sator, Phys. Rev. C **67**, 044610 (2003).

[139] S. Das Gupta, S. Mallik, G. Chaudhuri, Phys. Rev. C **97**, 044605 (2018).